Carlo F. Barenghi
Nick G. Parker

A Primer on Quantum Fluids

SpringerBriefs in Physics

Editorial Board

Carlo F. Barenghi · Nick G. Parker

A Primer on Quantum Fluids

Carlo F. Barenghi
Joint Quantum Centre
    (JQC) Durham-Newcastle
School of Mathematics and Statistics,
    Newcastle University
Newcastle upon Tyne
UK

Nick G. Parker
Joint Quantum Centre
    (JQC) Durham-Newcastle
School of Mathematics and Statistics,
    Newcastle University
Newcastle upon Tyne
UK

Preface

This book introduces the theoretical description and properties of quantum fluids. The focus is on gaseous atomic Bose–Einstein condensates and, to a minor extent, superfluid helium, but the underlying concepts are relevant to other forms of quantum fluids such as polariton and photonic condensates. The book is pitched at the level of advanced undergraduates and early postgraduate students, aiming to provide the reader with the knowledge and skills to develop their own research project on quantum fluids. Indeed, the content for this book grew from introductory notes provided to our own research students. It is assumed that the reader has prior knowledge of undergraduate mathematics and/or physics; otherwise, the concepts are introduced from scratch, often with references for directed further reading.

After an overview of the history of quantum fluids and the motivations for studying them (Chap. 1), we introduce the simplest model of a quantum fluid provided by the ideal Bose gas, following the seminal works of Bose and Einstein (Chap. 2). The Gross–Pitaevskii equation, an accurate description of weakly interacting Bose gases at low temperatures, is presented, and its typical time-independent solutions are examined (Chap. 3). We then progress to solitons and waves (Chap. 4) and vortices (Chap. 5) in quantum fluids. For important aspects which fall outside the scope of this book, e.g. modelling of Bose gases at finite temperatures, we list appropriate reading material. Each chapter ends with key exercises to deepen the understanding. Detailed solutions can be made available to instructors upon request to the authors.

We thank Nick Proukakis and Em Rickinson for helpful comments on this work.

Newcastle upon Tyne, UK Carlo F. Barenghi
April 2016 Nick G. Parker

Contents

Acronyms

List of Acronyms

1D   One-dimensional
2D   Two-dimensional
3D   Three-dimensional
BEC   Bose–Einstein condensate
GPE   Gross–Pitaevskii equation
LIA   Local induction approximation

List of Symbols

A	Wavefunction amplitude
$\mathbf{A}$	Vector potential
α_j	Scaling solution velocity coefficients, $j = x, y, z$
a_0	Vortex core radius
a_s	s-wave scattering length
b_j	Scaling-solution variables, $j = x, y, z$ or $j = r, z$
B	Dark soliton coefficient $B = \sqrt{1 - u^2/c^2}$
β	Irrotational flow amplitude
c	Speed of sound
$C_\mathcal{V}$	Heat capacity at constant volume
d	Average inter-particle distance
D	System size
$\mathcal{D}$	Number of dimensions
$\widehat{e}_j$	Unit vector. $j = x, y, z$ for Cartesian coordinates or $j = r, z, \theta$ for cylindrical polar coordinates
ε	Small parameter
E	Energy
E'	Energy per unit mass
η	Flow angle

f_j	Distribution function, with $j =$ B, BE or FD for the Boltzmann, Bose–Einstein or Fermi–Dirac distributions
F	Free energy
g_i	Degeneracy of i'th energy level
g	Density of states, $g(E)$ or $g(p)$
g	GPE nonlinear coefficient
$\Gamma(x)$	The Gamma function, $\Gamma = \int_0^\infty t^{x-1} e^{-t}\, dt$
H_0	Cylinder height
$\hbar$	Planck's constant, $\hbar = 6.63 \times 10^{-34}\,\mathrm{m^2 kg/s}$
k	Wavenumber
k_B	Boltzmann's constant, $k_\mathrm{B} = 1.38 \times 10^{-23}\,\mathrm{m^2 kg s^{-2}\,K^{-1}}$
κ	Quantum of circulation
λ	Trap ratio, ω_z/ω_r, of a cylindrically symmetric harmonic trap
L	Vortex line density
L_z	Angular momentum about z
ℓ	Wavepacket size (Chap. 4)
ℓ	Average inter-vortex distance (Chap. 5)
ℓ_j	Harmonic oscillator length $\ell_j = \sqrt{\hbar/m\omega_j}$ in jth dimension
λ	Wavelength, including de Broglie wavelength λ_dB
m	Mass
μ	Chemical potential
n	Number density
N	Number of particles, including critical number of particles N_c, and number of particles in i'th level, N_i
$\mathcal{N}_\mathrm{ps}$	Number of phase space cells
ω	Angular frequency, e.g. of wave or trap
$\boldsymbol{\omega}$	Vorticity
Ω	Rotation frequency
$\Omega(z)$	Complex potential
p	Momentum (vector $\mathbf{p}$, magnitude p)
$\mathcal{P}$	Condensate momentum
P	Pressure, including quantum pressure P'
Pr	Probability
ϕ	Velocity potential
ψ, Ψ	Condensate wavefunction
q	Vortex charge
ρ	Mass density
r	Radial coordinate, $r^2 = x^2 + y^2 + z^2$ or $r^2 = x^2 + y^2$
R_j	Thomas–Fermi radius in jth dimension
R	Local radius of curvature
R_0	Cylinder radius
σ	Variational width
S	Phase distribution
S	Entropy of vortex configuration (Sect. 5.12.2 only)

t	Time
T	Temperature, including critical temperature for BEC, T_c
u	Soliton speed
U	Internal energy
$\mathcal{U}$	Inter-atomic interaction potential
v	Fluid velocity
v_0	Frame velocity
V	Trapping potential
$\mathcal{V}$	Volume
W	Number of macrostates
ξ	Healing length
ξ_s	Bright soliton lengthscale
$\zeta(x)$	The Riemann zeta function, $\zeta(x) = \sum\limits_{p=1}^{\infty} \frac{1}{p^x}$

Chapter 1
Introduction

Abstract Quantum fluids have emerged from scientific efforts to cool matter to colder and colder temperatures, representing staging posts towards absolute zero (Fig. 1.1). They have contributed to our understanding of the quantum world, and still captivate and intrigue scientists with their bizarre properties. Here we summarize the background of the two main quantum fluids to date, superfluid helium and atomic Bose–Einstein condensates.

1.1 Towards Absolute Zero

The nature of cold has intrigued humankind. Its explanation as a primordial substance, *primum frigidum*, prevailed from the ancient Greeks until Robert Boyle pioneered the scientific study of the cold in the mid 1600s. Decrying the "almost totally neglect" of the nature of cold, he set about hundreds of experiments which systematically disproved the ancient myths and seeded our modern understanding. While working on an air-based thermometer in 1703, French physicist Guillaume Amontons observed that air pressure was proportional to temperature; extrapolating towards zero pressure led him to predict an "absolute zero" of approximately $-240\,°C$ in today's units, not far from the modern value of $-273.15\,°C$ (or $0\,K$). The implication was profound: the realm of the cold was much vaster than anyone had dared believe. An entertaining account of low temperature exploration is given by Ref. [1].

The liquefaction of the natural gases became the staging posts as low temperature physicists, with increasingly complex apparatuses, raced to explore the undiscovered territories of the "map of frigor". Chlorine was liquefied at 239 K in 1823, and oxygen and nitrogen at $T = 90$ and 77 K, respectively, in 1877. In 1898 the English physicist James Dewar liquefied what was believed to be the only remaining elementary gas, hydrogen, at 23 K, helped by his invention of the vacuum flask. Concurrently, however, chemists discovered helium on Earth. Although helium is the second most common element in the Universe and known to exist in the Sun, its presence on Earth is tiny. With helium's even lower boiling point, a new race was on. A dramatic series of lab explosions and a lack of helium supplies meant that Dewar's main competitor,
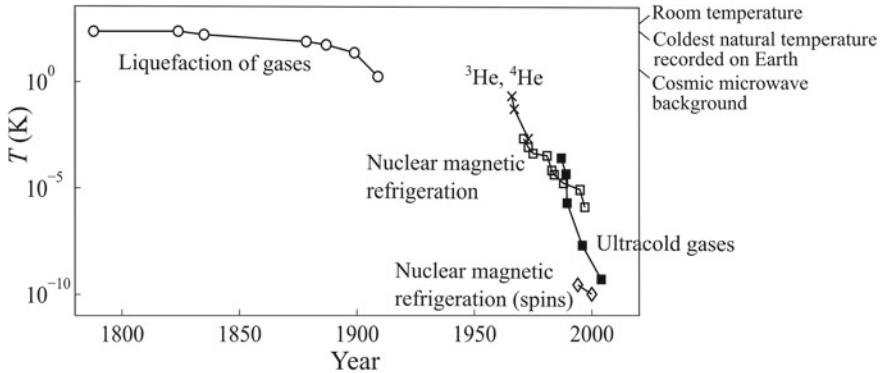
Fig. 1.1 Timeline of the coldest engineered temperatures, along with some reference temperatures

Heike Kamerlingh Onnes, pipped him to the post, liquifying helium at 4 K in 1908. This momentous achievement led to Onnes being awarded the 1913 Nobel Prize in Physics.

1.1.1 Discovery of Superconductivity and Superfluidity

These advances enabled scientists to probe the fundamental behaviour of materials at the depths of cold. Electricity was widely expected to grind to a halt in this limit. Using liquid helium to cool mercury, Onnes instead observed its resistance to simply vanish below 4 K. *Superconductivity*, the flow of electrical current without resistance, has since been observed in many materials, at up to 130 K, and has found applications in medical MRI scanners, particle accelerators and levitating "maglev" trains.

Onnes and his co-workers also observed unusual behaviour in liquid helium itself. At around 2.2 K its heat capacity undergoes a discontinuous change, termed the "lambda" transition due to the shape of the curve. Since such behaviour is characteristic of a phase change, the idea developed that liquid helium existed in two phases: helium I for $T > T_\lambda$ and helium II for $T < T_\lambda$, where T_λ is the critical temperature. Later experiments revealed helium II to have unusual properties, such as it remaining a liquid even as absolute zero is approached, the ability to move through extremely tiny pores and the reluctance to boil. These two liquid phases, and the fact that helium remains liquid down to $T \rightarrow 0$ (at atmospheric pressure), mean that the phase diagram of helium (Fig. 1.2) is very different to a conventional liquid (inset). In 1938, landmark experiments by Allen and Misener and by Kapitza revealed the most striking property of helium II: its ability to flow without viscosity. The amazing internal mobility of the fluid, analogous to superconductors, led Kapitza to coin the term "superfluid". Other strange observations followed, including "fluid creep" (the

Fig. 1.2 Phase diagram of helium. For a conventional substance (*inset*), there exists a *triple point* (TP), where solid, liquid and gas coexist. Helium lacks such a point. The *shaded region* illustrates where Bose–Einstein condensation is predicted to occur for an ideal gas
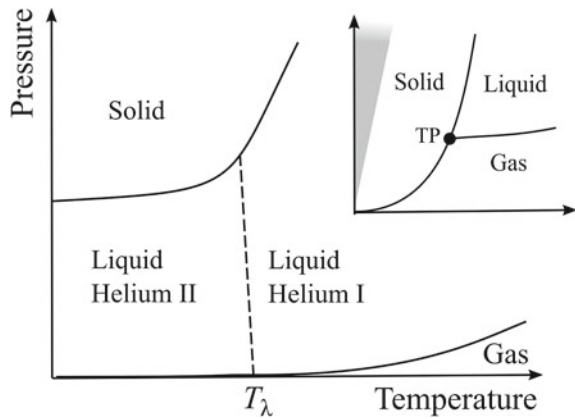
ability of helium to creep up the walls of a vessel and over the edge) and the "fountain effect" (generation of a persistent fountain when heat was applied to the liquid).

1.1.2 Bose–Einstein Condensation

Superfluidity and superconductivity were at odds with classical physics and required a new way of thinking. In 1938 London resurrected an obscure 1925 prediction of Einstein to explain superfluidity. Considering an ideal gas of quantum particles, Einstein (having developed the ideas put forward by Bose for photons) had predicted the effect of *Bose–Einstein condensation*, that at low temperatures a large proportion of the particles would condense into the same quantum state—the *condensate*—and the remainder of the particles would behave conventionally. This idea stalled, however, since the conditions for this gaseous phenomena lay in the solid region of the pressure-temperature diagram (shaded region in Fig. 1.2(inset)), making it inaccessible. We will follow Einstein's derivation in Chap. 2. Einstein's model predicts a discontinuity in the heat capacity, suggestively similar to that observed in helium. This, in turn, led to the development of the successful two-fluid model by Tizsa and Landau, in which helium-II is regarded as a combination of an viscosity-free superfluid and a viscous "normal fluid".

Bose–Einstein condensation applies to bosons (particles with integer spin, such as photons and ^{4}He atoms), but not to fermions (particles with half-integer spin, such as protons, neutrons and electrons). The Pauli exclusion principle prevents more than one identical fermion occupying the same quantum state. How then could Bose–Einstein condensation be responsible for the flow of electrons in superconductivity? The answer, put forward in 1957 by Bardeen, Cooper and Schrieffer was for the electrons to form *Cooper pairs*; these composite bosons could then undergo Bose–Einstein condensation. The observation of superfluidity in the fermionic

helium isotope ^{3}He in 1972 (at around 2 mK) further cemented this pairing mechanism. More information on superconductivity can be found in Ref. [2].

Superfluid helium and superconductors are both manifestations of Bose–Einstein condensation. Arising from the macroscopic quantum state that is the condensate, they represent fluids governed by quantum mechanics, i.e. quantum fluids (superconductors can be considered as fluids of charged Cooper pairs). However, the strong particle interactions in liquids and solids mean that these systems are much more complicated that Einstein's ideal-gas paradigm, and it took until the 1990s for an almost ideal state to be created.

Hallmarks of superfluidity include the capacity to flow without viscosity, the presence of a critical velocity above which superflow breaks down, the presence of quantized vortices, persistent flow, and macroscopic tunneling in the form of Josephson currents. We will detail all of these superfluid phenomena throughout this book, with the exception of Josephson currents which can be studied elsewhere [2].

1.2 Ultracold Quantum Gases

1.2.1 *Laser Cooling and Magnetic Trapping*

Liquids and solids have since been cooled down to milliKelvin and microKelvin temperatures using cryogenic refrigeration techniques and adiabatic demagnetization, respectively [3], and the coldest recorded temperature stands at 100 pK for the nuclear spins in a sample of rhodium; these achievements are shown in Fig. 1.1. Meanwhile, the cooling of gases was advanced greatly by *laser cooling*, developed in the 1980s [4]. Atoms and molecules in a gas are in constant random motion with an average speed related to temperature, for example, around 300 m/s in room temperature air. For a laser beam incident upon a gas of atoms (in a vacuum chamber), and under certain conditions, the photons in the beam can be made to impart, on average, momentum to atoms travelling towards the beam, thus slowing them down in that direction; applying laser beams in multiple directions then allows three-dimensional (3D) cooling. In 1985 this "optical molasses" produced a gas at 240 μK, with average atom speeds of ∼0.5 m/s. A few years later, 2 μK was achieved (∼1 cm/s). These vapours were extremely dilute, with typical number densities of $n \sim 10^{20}$ m^{-3} (c.f. $n \sim 10^{25}$ m^{-3} for room temperature air); this made the transition from a gas to a solid, the natural process at such cold temperatures (inset of Fig. 1.2), so slow as to be insignificant on the experimental timescales. In addition, magnetic fields allowed the creation of traps, bowl-like potentials to confine the atoms and keep them away from hot surfaces; with experimental advances, it is now possible to create such ultracold gases in a variety of configurations, from toruses to periodic potentials, and manipulate them in time. The development of laser cooling and magnetic trapping techniques was recognised with the 1997 Nobel Prize in Physics [5]; further details of these techniques can be found elsewhere [4, 6].

1.2.2 Bose–Einstein Condensate à la Einstein

The achievement of ultracold gases put Einstein's gaseous condensate within sight and a new race was on. Einstein's model predicted the condensate to form below a critical temperature $T_c \sim 10^{-19} n^{2/3}$, but the low gas densities employed predicted $T_c \sim 1\,\mu\text{K}$, colder than achievable by laser cooling alone. To cool even further, a stage of *evaporative cooling* was employed whereby the hottest atoms were selectively removed, just like how evaporation cools a cup of coffee.

In 1995 Cornell and Wieman cooled a gas of rubidium atoms down to 200 nK (200 billionths of a degree above absolute zero) to realize the first gaseous Bose–Einstein condensate (BEC) [7]. Figure 1.3 shows the famous experimental signature of this new state of matter. These images were obtained by releasing the trap which confines the gas, thus letting the atoms fly away and the gas to expand. Above T_c (left plot), the gas was an energetic "thermal" gas of atoms characterised by a wide distribution of speed; upon opening the trap, atoms with large speeds moved far away, hence the broad picture in the left plot. As the temperature was cooled through T_c, a narrow distribution emerged from the thermal gas (middle and right plots), characteristic of accumulation of atoms into a state of almost zero energy and speed; these atoms are the Bose–Einstein condensate. We derive these thermal and condensate profiles in Chap. 2. A few months later, Ketterle independently reported a BEC of sodium atoms [8]. Seventy years on, Einstein's prediction had been realized at the depths of absolute zero. Cornell, Wieman and Ketterle shared the 2001 Nobel Prize for this landmark achievement [9].
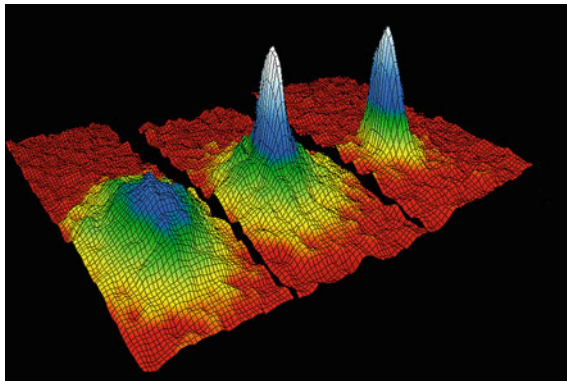
Fig. 1.3 The first observation of a gas Bose–Einstein condensate [7], showing the momentum distribution of a dilute ultracold gas of ^{87}Rb atoms, confined in a harmonic trap. As the temperature was reduced, the gas changed from a broad, energetic thermal gas (*left*) to a narrower distribution (*right*), characteristic of the condensate. Image reproduced from the NIST Image Gallery (Reference NIST/JILA/CU-Boulder)

There are now over 100 BEC experiments worldwide. These gases are typically 10–100 μm across (about the width of a human hair), exist in the temperature range 1 to 100 nK, contain $10^3 - 10^9$ atoms, and are many times more dilute than room temperature air. BECs are most commonly formed with rubidium (^{87}Rb) and sodium (^{23}Na) atoms, but many other atomic species, and a growing number of molecular species, have been condensed. It is also possible to create multi-component condensates, where two or more condensates co-exist. These gases constitute the purest and simplest quantum fluids available, with typically 99 % of the atoms lying in the condensed state. The last property makes condensates amenable to first-principles modelling; the work-horse model is provided by the Gross–Pitaevskii equation, which will be introduced and analysed in Chap. 3. Gaseous condensates have remarkable properties, such as superfluidity, as we see in Chaps. 4 and 5. Unlike superfluid helium, the interaction between the atoms is very weak, which makes them very close to Einstein's original concept of an ideal gas.

1.2.3 Degenerate Fermi Gases

For a fermionic gas, cooled towards absolute zero, the particles (in the absence of Cooper pairing) are forbidden to enter the same quantum state by the Pauli exclusion principle. Instead, they are expected fill up the quantum states, from the ground state upwards, each with unit occupancy. This effect was observed in 1999 when a degenerate Fermi gas was formed by cooling potassium (^{40}K) atoms to below 300 nK [10]. In this limit, the gas was seen to saturate towards a relatively wide distribution, indicating the higher average energy of the system, relative to a BEC. The Pauli exclusion principle exerts a very strong "pressure" against further contraction, an effect which is believed to stabilize neutron stars against collapse. A striking experimental comparison between bosonic and fermionic gases as the temperature is reduced is shown in Fig. 1.4: the distribution of the fermionic system cannot contract as the bosonic one. More recently, experiments have examined the formation of Cooper pairs in these systems [11].

1.3 Quantum Fluids Today

We have briefly told the story of the discoveries of superfluid helium and atomic condensates, but what about the wider implications of these discoveries and the current status of the field? Here we list some examples.

Many-body quantum systems: Quantum fluids embody quantum behaviour on a macroscopic scale of many particles; it is this property that gives rise to their remarkable properties. As such, quantum fluids provide fundamental insight into quantum many-body physics. Moreover, for the case of condensates, the
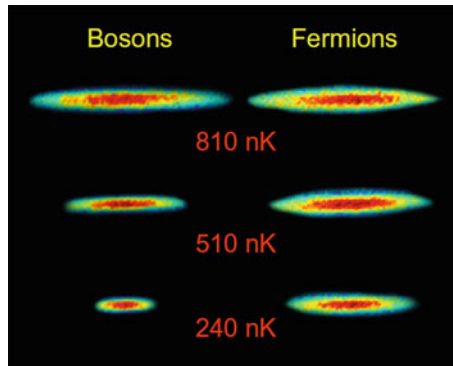
Fig. 1.4   Change in density profile as a ^{7}Li bosonic gas and a ^{6}Li fermionic gas are cooled towards absolute zero. The bosonic gas reduces to a narrow distribution corresponding to the low-energy condensate, while the fermionic gas saturates to a larger distribution due to the outwards Pauli pressure imposed by the fermions. Reproduced from http://apod.nas.gov with permission from A.G. Truscott and R.G. Hulet, and corresponding to the experiment of Ref.[12]

experimental capacity to engineer the system, e.g. its interactions, dimensionality, and the presence of disorder and periodicity, allows the controlled investigation of diverse many-body scenarios and emulation of complex condensed matter systems such as superconductors.

Nonlinear systems: Quantum fluids represent a prototype fluid, free from viscosity (as we see in Chap. 3) and whose vorticity is constrained to take the form of discrete, uniformly-sized mini-tornadoes. It is interesting then to consider complex fluid dynamics, notably turbulence, in this simplified fluid; we discuss this *quantum turbulence* in Chap. 5. Condensates also provide an idealized system to study nonlinear phenomena. The atomic interactions in a condensate give rise to a well-defined nonlinearity, and experimental tricks allow this nonlinearity to be controlled in size and nature (e.g. local versus non-local nonlinearity). Nonlinear effects such as solitons and four-wave mixing have been experimentally studied; we meet solitons in Chap. 4.

Extra-terrestrial phenomena: Condensates are analogous to curved space-time and support analog black holes and Hawking radiation, while both condensates and helium provide analogs of the quantum vacuum believed to permeate the universe and be responsible for its development from the Big Bang. These cosmological phenomena, not accessible on Earth, may thus be mimicked and explored in controlled, laboratory-based experiments.

Cooling: The excellent thermal transport property of helium II lends to its use as a coolant; helium is therefore present in superconducting systems, from MRI machines in hospitals to the Large Hadron Collider at CERN.

Sensors: Condensates are easily affected by external forces, and experiments have demonstrated extreme sensitivity to magnetic fields, gravity and rotational forces. Considerable efforts are currently underway to develop these ideas into

next-generation sensors, for applications such as testing fundamental laws of physics, geological mapping and navigation.

Since 2000, Bose–Einstein condensation has also been achieved in several new systems: magnons (magnetic quasi-particles) in magnetic insulators, polaritons (coupled light-matter quasi-particles) in semiconductor microcavities, and photons in optical microcavities. In particular, the latter two systems have realized quantum fluids of light, with superfluid properties.

References

1. T. Shachtman, *Absolute Zero and the Conquest of Cold* (Houghton-Mifflin, Boston, 2001)
2. J.F. Annett, *Superconductivity, Superfluids and Condensates* (Oxford University Press, Oxford, 2004)
3. F. Pobell, *Matter and Methods at Low Temperatures*, 3rd edn. (Springer, Berlin, 2007)
4. H.J. Metcalf, P. van der Straten, *Laser Cooling and Trapping (Graduate Texts in Contemporary Physics)* (Springer, Berlin, 2001)
5. The Nobel Prize in Physics (1997). www.nobelprize.org/nobel_prizes/physics/laureates/1997/
6. C.J. Pethick, H. Smith, *Bose-Einstein Condensation in Dilute Gases* (Cambridge University Press, Cambridge, 2008)
7. M.H. Anderson et al., Science **269**, 198 (1995)
8. K.B. Davis et al., Phys. Rev. Lett. **75**, 3969 (1995)
9. The Nobel Prize in Physics (2001). http://www.nobelprize.org/nobel_prizes/physics/laureates/2001/
10. B. DeMarco, D.S. Jin, Science **285**, 1703 (1999)
11. K. Levin, R.G. Hulet, The Fermi Gases and Superfluids: Experiment and Theory, in *Ultracold Bosonic and Fermionic Gases*, ed. by K. Levin, A.L. Fetter, D.M. Stamper-Kurn (Elsevier, Oxford, 2012)
12. A.G. Truscott, K.E. Strecker, W.I. McAlexander, G.B. Partridge, R.G. Hulet, Science **291**, 2570 (2001)

Chapter 2
Classical and Quantum Ideal Gases

Abstract Bose and Einstein's prediction of Bose–Einstein condensation came out of their theory for how quantum particles in a gas behaved, and was built on the pioneering statistical approach of Boltzmann for classical particles. Here we follow Boltzmann, Bose and Einstein's footsteps, leading to the derivation of Bose–Einstein condensation for an ideal gas and its key properties.

2.1 Introduction

Consider the air in the room around you. We ascribe properties such as temperature and pressure to characterise it, motivated by our human sensitivity to these properties. However, the gas itself has a much finer level of detail, being composed of specks of dust, molecules and atoms, all in random motion. How can we explain the macroscopic, coarse-grained appearance in terms of the fine-scale behaviour? An exact classical approach would proceed by solving Newton's equation of motion for each particle, based on the forces it experiences. For a typical room (volume $\sim$50 m^3, air particle density $\sim 2 \times 10^{25}$ m^{-3} at room temperature and pressure) this would require solving around 10^{28} coupled ordinary differential equations, an utterly intractable task. Since the macroscopic properties we experience are *averaged* over many particles, a particle-by-particle description is unnecessarily complex. Instead it is possible to describe the fine-scale behaviour *statistically* through the methodology of statistical mechanics. By specifying rules about how the particles behave and any physical constraints (boundaries, energy, etc.), the most likely macroscopic state of the system can be deduced.

We develop these ideas for an ideal gas of N identical and non-interacting particles, with temperature T and confined to a box of volume $\mathcal{V}$. The system is isolated, with no energy or particles entering or leaving the system[1] Our aim is to predict the equilibrium state of the gas. After performing this for classical (point-like) particles, we extend it to quantum (blurry) particles. This leads directly to the prediction of Bose–Einstein condensation of an ideal gas. In doing so, we follow the seminal

---

[1]In the formalism of statistical mechanics, this is termed the *microcanonical ensemble*.

Fig. 2.1 Two different classical particle trajectories through 1D phase space (x, p_x), with the same initial and final states. While classical phase space is a continuum of states, it is convenient to imagine phase space to be discretized into finite-sized cells, here with size Δp_x and Δx
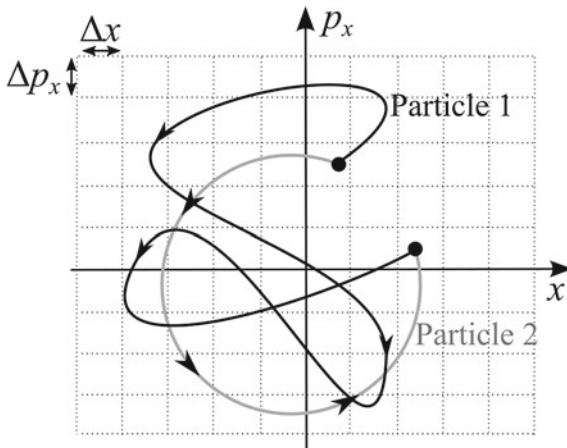
works of Boltzmann, Bose and Einstein. Further information can be found in an introductory statistical physics textbook, e.g., [1] or [2].

2.2 Classical Particles

The state of a classical particle is specified by its position **r** and momentum **p**. In the 3D Cartesian world, this requires six coordinates (x, y, z, p_x, p_y, p_z). Picturing the world as an abstract six dimensional *phase space*, the instantaneous state of the particle is a point in this space, which traces out a trajectory as it evolves. Accordingly, an N-particle gas is specified by N points/trajectories in this phase space. The accessible range of phase space is determined by the box (which provides a spatial constraint) and the energy of the gas (which determines the maximum possible momentum). Figure 2.1 (left) illustrates two particle trajectories in 1D phase space (x, p_x).

Classically, a particle's state (its position and momentum) can be determined to arbitrary precision. As such, classical phase space is continuous and contains an infinite number of accessible states. This also implies that each particle can be independently tracked, that is, that the particles are *distinguishable* from each other.

2.3 Ideal Classical Gas

We develop an understanding of the macroscopic behaviour of the gas from these microscopic rules (particle distinguishability, continuum of accessible states) following the pioneering work of Boltzmann in the late 1800s on the kinetic theory of

gases. Boltzmann's work caused great controversy, as its particle and statistical basis was at odds with the accepted view of matter as being continuous and deterministic. To overcome the practicalities of dealing with the infinity of accessible states, we imagine phase space to be discretized into cells of finite (but otherwise arbitrary) size, as shown in Fig. 2.1, and our N particles to be distributed across them randomly. Let there be M accessible cells, each characterised by its average momentum and position. The number of particles in the ith cell—its *occupancy number*—is denoted as N_i. The number configuration across the whole system is specified by the full set of occupancy numbers $\{N_1, N_2, \ldots, N_M\}$. We previously assumed that the total particle number is conserved, that is,

$$N = \sum_{i=1}^{i=M} N_i.$$

Conservation of energy provides a further constraint; for now, however, we ignore energetic considerations.

2.3.1 Macrostates, Microstates and the Most Likely State of the System

The macroscopic, equilibrium state of the gas is revealed by considering the ways in which the particles can be distributed across the cells. In the absence of energetic constraints, each cell is equally likely to be occupied. Consider two classical particles, A and B (the distinguishability of the particles is equivalent to saying we can label them), and three such cells. The nine possible configurations, shown in Fig. 2.2, are termed *microstates*. Six distinct sets of occupancy numbers are possible, $\{N_1, N_2, N_3\} = \{2, 0, 0\}, \{0, 2, 0\}, \{0, 0, 2\}, \{1, 1, 0\}, \{1, 0, 1\}$ and $\{0, 1, 1\}$; these are termed *macrostates*. Each macrostate may be achieved by one or more microstates.

The particles are constantly moving and interacting/colliding with each other in a random manner, such that, after a sufficiently long time, they will have visited all available microstates, a process termed *ergodicity*. It follows that each microstate is
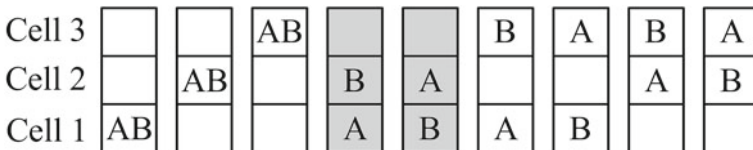
Fig. 2.2 Possible configurations of two classical particles, A and B, across three equally-accessible cells. If we treat the energies of cells 1–3 as 0, 1 and 2, respectively, and require that the total system energy is 1 (in arbitrary units), then only the shaded configurations are possible

equally likely (the assumption of "equal *a priori* probabilities"). Thus the most prob-
able macrostate of the system is the one with the most microstates. In our example, the
macrostates {1, 1, 0}, {1, 0, 1} and {0, 1, 1} are most probable (having 2 microstates
each). In a physical gas, each macrostate corresponds to a particular macroscopic
appearance, e.g. a certain temperature, pressure, etc. Hence, these abstract proba-
bilistic notions become linked to the most likely macroscopic appearances of the
gas.

For a more general macrostate {N_1, N_2, N_3, .., N_I}, the number of microstates is,

$$W = \frac{N!}{\prod_i N_i!}. \tag{2.1}$$

Invoking the principle of equal *a priori* probabilities, the probability of being in the
*j*th macrostate is,

$$\Pr(j) = \frac{W_j}{\sum_j W_j}. \tag{2.2}$$

W_j, and hence Pr(j), is maximised for the most even distribution of particles across
the cells. This is true when each cell is equally accessible; as we discuss next, energy
considerations modify the most preferred distribution across cells.

2.3.2 The Boltzmann Distribution

In the ideal-gas-in-a-box, each particle carries only *kinetic energy* $p^2/2m = (p_x^2 + p_y^2 + p_z^2)/2m$. Having discretizing phase space, particle energy also becomes
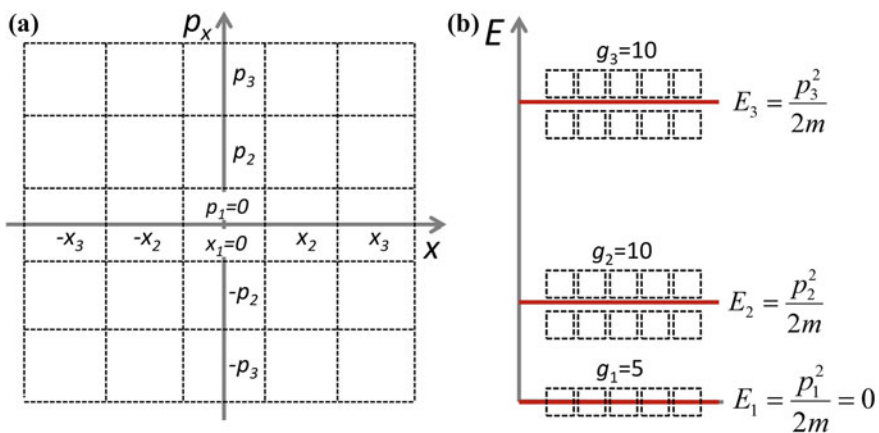
Fig. 2.3 For the phase space (x, p_x) shown in (**a**), the discretization of phase space, coupled
with the energy-momentum relation $E = p^2/2m$, leads to the formation of (**b**) energy levels. The
degeneracy g of the levels is shown

discretized, forming the notion of energy levels (familiar from quantum mechanics). This is illustrated in Fig. 2.3 for (x, p_x) phase space. Three energy levels, $E_1 = 0$, $E_2 = p_1^2/2m$ and $E_3 = p_2^2/2m$, are formed from the five momentum values $(p = 0, \pm p_1, \pm p_2)$. In two- and three-spatial dimensions, cells of energy E_i fall on circles and spherical surfaces which satisfy $p_x^2 + p_y^2 = 2mE_i$ and $p_x^2 + p_y^2 + p_z^2 = 2mE_i$, respectively. The lowest energy state E_1 is the *ground state*; the higher energy states are *excited states*.

The total energy of the gas U is,

$$U = \sum_i N_i E_i,$$

where E_i is the energy of cell i. Taking U to be conserved has important consequences for the microstates and macrostates. For example, imposing some arbitrary energy values in Fig. 2.2 restricts the allowed configurations. Particle occupation at high energy is suppressed, skewing the distribution towards low energy.

For a system at thermal equilibrium with a large number of particles, one macrostate (or a very narrow range of macrostates) will be greatly favoured. The preferred macrostate can be analytically predicted by maximising the number of microstates W with respect to the set of occupancy numbers $\{N_1, N_2, N_3, \ldots, N_I\}$; details can be found in, e.g. [1, 2]. The result is,

$$N_i = f_B(E_i), \tag{2.3}$$

where $f_B(E)$ is the famous Boltzmann distribution,

$$f_B(E) = \frac{1}{e^{(E-\mu)/k_B T}}. \tag{2.4}$$

The Boltzmann distribution tells us the most probable spread of particle occupancy across states in an ideal gas, as a function of energy. This is associated with the thermodynamic equilibrium state. Here k_B is Boltzmann's constant (1.38×10^{-23} m^2 kg s^{-2} K^{-1}) and T is temperature (in Kelvin degrees, K). On average, each particle carries kinetic energy $\frac{3}{2}k_B T$ ($\frac{1}{2}k_B T$ in each direction of motion); this property is referred to as the *equipartition theorem*.

The Boltzmann distribution function f_B is normalized to the number of particles, N, as accommodated by the chemical potential μ. Writing $A = e^{\mu/k_B T}$ gives $f_B = A/e^{E/k_B T}$, evidencing that A, and thereby μ, controls the amplitude of the distribution function.

The Boltzmann distribution function $f_B(E)$ is plotted in Fig. 2.4. Low energy states (cells) are highly occupied, with diminishing occupancy of higher energy states. As the temperature and hence the thermal energy increases, the distribution broadens as particles can access, on average, higher energy states. Remember, however, that this is the most *probable* distribution. Boltzmann's theory allows for the possibility, for example, that the whole gas of molecules of air in a room concentrates into a

Fig. 2.4 The Boltzmann
distribution function $f_B(E)$
for 3 different temperatures
(the direction of increasing
temperature is indicated)
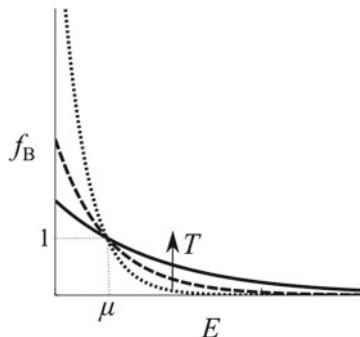
corner of the room. Due to the strong statistical bias towards an even distribution of
energy, momenta and position, such an occurrence has incredibly low probability,
but it is nonetheless possible, a fact which caused great discomfort with the scientific
community at the time.

It is often convenient to work in terms of the occupancy of *energy levels* rather than
states (phase space cells). To relate the Boltzmann result to energy levels, we must
take into account the number of states in a given energy level, termed the *degeneracy*
and denoted g_j (we reserve i as the labelling of states). The occupation of the jth
energy level is then,

$$N_j = g_j f_B(E_j). \tag{2.5}$$

2.4   Quantum Particles

Having introduced classical particles, their statistics and the equilibrium properties
of the ideal gas, now we turn to the quantum case. The statistics of quantum particles,
developed in the 1920s, was pivotal to the development of quantum mechanics, pre-
dating the well-known Schrödinger equation and uncertainty principle.

2.4.1   A Chance Discovery

Quantum physics arose from the failure of classical physics to describe the emission
of radiation from a black body in the ultraviolet range (the "ultraviolet catastrophe").
In 1900, Max Planck discovered a formula which empirically fit the data for all
wavelengths and led him to propose that energy is emitted in discrete quanta of units
hf (h being Planck's constant and f the radiation frequency). Einstein extended this
idea with his 1905 prediction that the light itself was quantized.

The notion of quantum particles was discovered by accident. Around 1920, the
Indian physicist Satyendra Bose was giving a lecture on the failure of the classical

theory of light using statistical arguments; a subtle mistake led to him prove the opposite. Indeed, he was able to derive Planck's empirical formula from first principles, based on the assumptions that (a) the radiation particles are indistinguishable and (b) phase space was discretized into cells of size h^3. Bose struggled at first to get these results published and sought support from Nobel Laureate Einstein; Bose's paper "Planck's law and the light quantum hypothesis" was then published in 1924 [3]. Soon after Einstein extended the idea to particles with mass in the paper "Quantum theory of the monoatomic ideal gas" [4].

The division of phase space was mysterious. Bose wrote "Concerning the kind of subdivision of this type, nothing definitive can be said", while Einstein confided in a colleague that Bose's "derivation is elegant but the essence remains obscure". It is now established as a fundamental property of particles, consistent with de Broglie's notion of wave-particle duality (that particles are smeared out, over a lengthscale given by the de Broglie wavelength $\lambda_{dB} = h/p$) and with Heisenberg's uncertainty principle (that the position and momentum of a particle have an inherent uncertainty $\Delta x \Delta y \Delta z \Delta p_x \Delta p_y \Delta p_z = h^3$). Each cell represents a distinct quantum state. The indistinguishability of particles follows since it becomes impossible to distinguish two blurry particles in close proximity in phase space.

2.4.2 Bosons and Fermions

Quantum particles come in two varieties—*bosons* and *fermions*:

Fermions   Soon after Bose and Einstein's work, Fermi and Dirac developed *Fermi-Dirac statistics* for fermions. Fermions possess half-integer spin, and include electrons, protons and neutrons. Fermions obey the Pauli exclusion principle (Pauli, 1925), which states that two identical fermions cannot occupy the same quantum state simultaneously.

Bosons   Bosons obey Bose–Einstein statistics, as developed by Bose and Einstein (above), and include photons and the Higgs boson. Bosons have integer spin, and since spin is additive, composite bosons may be formed from equal numbers of fermions, e.g. ^{4}He, ^{87}Rb and ^{23}Na. Unlike fermions, any number of bosons can occupy the same quantum state simultaneously.

The indistinguishability of quantum particles, and the different occupancy rules for bosons and fermions, affect their statistical behaviour. Consider 2 quantum particles across 3 cells, as shown in Fig. 2.5. Since the particles are indistinguishable, we can no longer label them. For bosons there are six microstates; for fermions there are only three (compared to nine for classical particles, Fig. 2.2). The relative probability of paired states to unpaired states is $\frac{1}{3}$, $\frac{1}{2}$ and 0 for classical particles, bosons and fermions, respectively. Bosons are the most gregarious, having the greatest tendency to bunch up, while fermions are the most anti-social of all and completely avoid each other.
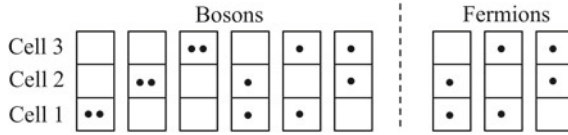
Fig. 2.5 Possible configurations of two bosons (*left*) and two fermions (*right*) across three equally-accessible cells. The classical case was shown in Fig. 2.2

2.4.3 The Bose–Einstein and Fermi-Dirac Distributions

Boltzmann's mathematical trick of discretizing classical phase space becomes physical reality in the quantum world, and the same methodology can be applied to find the distribution functions for bosons and fermions (accounting for their indistinguishability and occupancy rules). The Bose–Einstein and Fermi-Dirac particle distribution functions, which describe the mean distribution of bosons and fermions over energy E in an ideal gas, are,

$$f_{\mathrm{BE}}(E) = \frac{1}{e^{(E-\mu)/k_{\mathrm{B}}T} - 1}, \tag{2.6}$$

$$f_{\mathrm{FD}}(E) = \frac{1}{e^{(E-\mu)/k_{\mathrm{B}}T} + 1}. \tag{2.7}$$

The rather insignificant looking $-1/+1$ terms in the denominators have profound consequences. Figure 2.6 compares the Boltzmann, Bose–Einstein and Fermi-Dirac distributions.

We make the following observations of the distributions functions:

- To be physical, the distribution functions must satisfy $f \geq 0$ (for all E). This implies that $\mu \leq 0$ for the Bose–Einstein distribution. For the Fermi-Dirac and Boltzmann distributions, μ can take any value and sign.
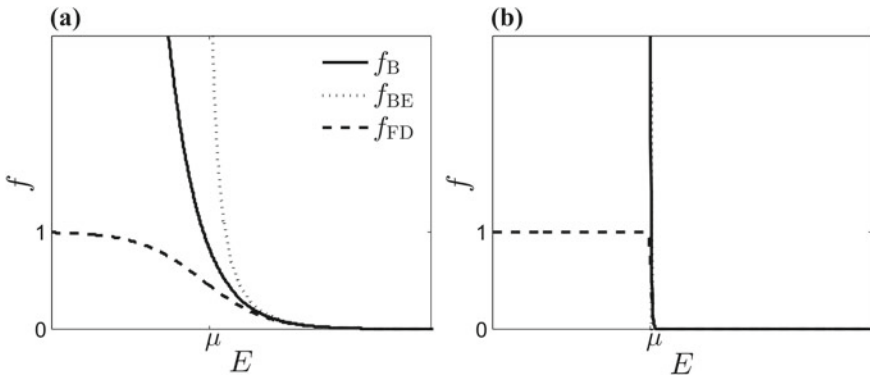
Fig. 2.6 The Boltzmann, Bose–Einstein and Fermi-Dirac distribution functions for **a** $T \gg 0$ and **b** $T \approx 0$

- For $(E - \mu)/k_{\mathrm{B}}T \gg 1$, the Bose–Einstein and Fermi-Dirac distributions approach the Boltzmann distribution. Here, the average state occupancy is much less than unity, such that the effects of particle indistinguishability become negligible. Note that the classical limit condition $(E - \mu)/k_{\mathrm{B}}T \gg 1$ should not be interpreted too directly, as it seems to predict, counter-intuitively, that low temperatures favour classical behaviour; this is because μ itself has a non-trivial temperature dependence.
- As $E \to \mu$ from above, the Bose–Einstein distribution diverges, i.e. particles accumulate in the lowest energy states.
- For $E \ll \mu$, the Fermi-Dirac distribution saturates to one particle per state, as required by the Pauli exclusion principle.
- For decreasing temperature, the distributions develop a sharper transition about $E = \mu$, approaching step-like forms for $T \to 0$.

2.5   The Ideal Bose Gas

A year after Einstein and Bose set forth their new particle statistics for a gas of bosons, Einstein published "Quantum theory of the monoatomic ideal gas: a second treatise" [5], elaborating on this topic. Here he predicted Bose–Einstein condensation. We now follow Einstein's derivation of this phenomena and predict some key properties of the gas.

2.5.1   Continuum Approximation and Density of States

We consider an ideal (non-interacting) gas of bosons confined to a box, with energy level occupation according to the Bose–Einstein distribution (2.6). For mathematical convenience we approximate the discrete energy levels by a continuum, valid providing there are a large number of accessible energy levels. Replacing the level variables with continuous quantities ($E_j \mapsto E$, $g_j \mapsto g(E)$ and $N_j \mapsto N(E)$), the number of particles at energy E is written,

$$N(E) = f_{\mathrm{BE}}(E)\, g(E) = \frac{g(E)}{e^{(E-\mu)/k_{\mathrm{B}}T} - 1}, \tag{2.8}$$

where $g(E)$ is the *density of states*. The total number of particles and total energy follow as the integrals,

$$N = \int N(E)\, \mathrm{d}E, \tag{2.9}$$

$$U = \int E\, N(E)\, \mathrm{d}E. \tag{2.10}$$

Fig. 2.7 The volume of momentum space from p to $p + dp$ is a spherical shell in 3D momentum space
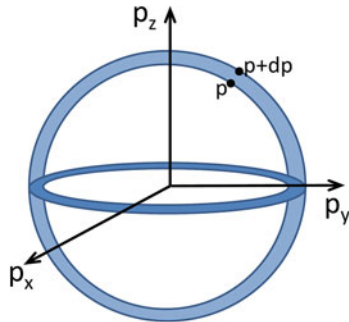
These are integrated in energy upwards from the $E = 0$ ($j = 1$) ground state.

The density of states $g(E)$ is defined such that the total number of possible states in phase space $\mathcal{N}_{ps}$ is,

$$\mathcal{N}_{ps} = \int g(E)dE = \int g(p)dp, \tag{2.11}$$

where we have also provided the corresponding expression in terms of momentum p, which is more convenient to work with. The quantity $g(p)dp$ represents the number of states lying between momenta p and $p + dp$. These states occupy a (6D) volume in phase space which is the product of their (3D) volume in position space and their (3D) volume in momentum space. The former is the box volume, $\mathcal{V}$. For the latter, the range p to $p + dp$ represents a spherical shell in momentum space of inner radius p and thickness dp, as illustrated in Fig. 2.7, with momentum-space volume $4\pi p^2 dp$. Hence the phase space volume is $4\pi p^2 \mathcal{V} dp$. Now recall that each quantum state takes up a volume h^3 in phase space. Thus the number of states between p and $p + dp$ is,

$$g(p)dp = \frac{4\pi p^2 \mathcal{V}}{h^3}dp. \tag{2.12}$$

Using the momentum-energy relation $p^2 = 2mE$, its differential form $dp = \sqrt{m/2E}\,dE$), and the relation $g(E)\,dE = g(p)\,dp$, Eq. (2.12) leads to,

$$g(E) = \frac{2\pi(2m)^{\frac{3}{2}}\mathcal{V}}{h^3}E^{\frac{1}{2}}. \tag{2.13}$$

This is the density of states for an ideal gas confined to a box of volume $\mathcal{V}$. There are a diminishing amount of states in the limit of zero energy, and an increasing amount with larger energy.

While the *occupancy of a state* goes like $1/(e^{(E-\mu)/k_B T} - 1)$ and diverges as $E \to \mu$, the *occupancy of an energy level* goes like $E^{\frac{1}{2}}/(e^{(E-\mu)/k_B T} - 1)$ and diminishes as $E \to 0$ (due to the decreasing amount of available states in this limit). These two distributions are compared in Fig. 2.8a.
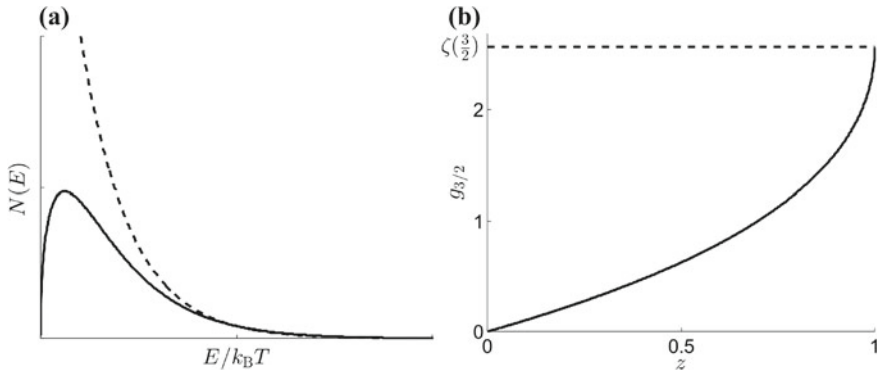
Fig. 2.8 a The occupancy of energy levels $N(E)$ (*solid line*), compared to the Bose–Einstein distribution f_{BE} (*dashed line*). The former vanishes as $E \to 0$ due to the diminishing density of states in this limit. **b** The function $g_{\frac{3}{2}}(z) = \sum_{p=1}^{\infty} z^p / p^{\frac{3}{2}}$ over the relevant range $0 < z \leq 1$

2.5.2 Integrating the Bose–Einstein Distribution

Using Eqs. (2.8, 2.13) we can write the number of particles (2.9) as,

$$N = \frac{2\pi(2m)^{\frac{3}{2}}\mathcal{V}}{h^3} \int_0^\infty \frac{E^{\frac{1}{2}}}{e^{(E-\mu)/k_B T} - 1} dE. \tag{2.14}$$

We seek to evaluate this integral. To assist us, we quote the general integral,[2]

$$\int_0^\infty \frac{x^\alpha}{e^x/z - 1} dx = \Gamma(\alpha + 1)g_{\alpha+1}(z), \tag{2.15}$$

where $\Gamma(x) = \int_0^\infty t^{x-1}e^{-t}dt$ is the *Gamma function*.[3] We have also defined a new function, $g_\beta(z) = \sum_{p=1}^{\infty} \frac{z^p}{p^\beta}$; an important case is when $z = 1$ for which it reduces to the *Riemann zeta function*,[4] $\zeta(\beta) = \sum_{p=1}^{\infty} \frac{1}{p^\beta}$.

---

[2]This result can be derived by introducing new variables $z = e^{\mu/k_B T}$ and $x = E/k_B T$ to rewrite part of integrand in the form $ze^{-x}/(1 - ze^{-x})$, and then writing as a power series expansion.
[3]Relevant values for us are $\Gamma(3/2) = \sqrt{\pi}/2$ and $\Gamma(5/2) = 3\sqrt{\pi}/4$.
[4]Relevant values for us are $\zeta(3/2) = 2.612$ and $\zeta(5/2) = 1.341$.

Taking $\alpha = \frac{1}{2}$, $x = E/k_{\mathrm{B}}T$ and $z = e^{\mu/k_{\mathrm{B}}T}$ in the general result (2.15), we evaluate Eq. (2.14) as,

$$N = \frac{(2\pi m k_{\mathrm{B}}T)^{\frac{3}{2}}\mathcal{V}}{h^3} g_{\frac{3}{2}}(z), \qquad (2.16)$$

where we have used the result $\Gamma(3/2) = \sqrt{\pi}/2$. Note that the relevant range of z is $0 < z \leq 1$: the lower limit is required since $z = e^{\mu/k_{\mathrm{B}}T} > 0$ while the upper limit $z \leq 1$ is required to prevent negative populations. Note also that $\mu \leq 0$ over this range, as required for the Bose–Einstein distribution (recall Sect. 2.4.3). In Fig. 2.8b we plot $g_{\frac{3}{2}}(z)$ over this range.

2.5.3   Bose–Einstein Condensation

The prediction of Bose–Einstein condensation in the style of Einstein arises directly from Eq. (2.16). Consider adding particles to the box, while at constant temperature. An increase in N is accommodated by an increase in the function $g_{\frac{3}{2}}(z)$. However, $g_{\frac{3}{2}}(z)$ is finite, reaching a maximum value of $g_{\frac{3}{2}} = \zeta(\frac{3}{2}) = 2.612$ at $z = 1$. In other words, the system becomes *saturated* with particles. This critical number of particles, denoted N_{c}, follows as,

$$N_{\mathrm{c}} = \frac{(2\pi m k_{\mathrm{B}}T)^{\frac{3}{2}}\mathcal{V}}{h^3} \zeta(\frac{3}{2}). \qquad (2.17)$$

Our derivation predicts a limit to how many particles the Bose–Einstein distribution can hold, but common sense tells us that it should always be possible to add more particles to the box. In fact, we made a subtle mistake. In calculating N we replaced the summation over discrete energy levels (from the $i = 1$ ground state upwards) by an integral over a continuum of energies (from $E = 0$ upwards). However, this continuum approximation does not properly account for the population of the ground state, since the density of states, $g(E) \propto E^{\frac{1}{2}}$, incorrectly predicts zero population in the ground state. What we have predicted is the *saturation of the excited states*; any additional particles added to the system enter the ground state (which comes at no energetic cost). For $N \gg N_{\mathrm{c}}$, the ground state acquires an anomalously large population.

As Einstein put it [5], "a number of atoms which always grows with total density makes a transition to the ground quantum state, whereas the remaining atoms distribute themselves... A separation occurs; a part condenses, the rest remains a saturated ideal gas." This effect is *Bose–Einstein condensation*, and the collection of particles in the ground state is the *Bose–Einstein condensate*. The effect is a condensation in momentum space, referring to the occupation of the zero momentum state. In practice, when the system is confined by a potential, a condensation in real space also takes place, towards the region of lowest potential. Bose–Einstein condensation is a *phase transition*, but whereas conventional phase transitions (e.g. transformation

from gas to liquid or liquid to solid) are driven by particle interactions, Bose–Einstein condensation is driven by the particle statistics.

Based on the above hindsight, we note that the total atom number N appearing in Eqs. (2.9), (2.14) and (2.16) should be replaced by the number in excited states, N_{ex}.

2.5.4 Critical Temperature for Condensation

If, instead, the particle number and volume are fixed, then there exists a critical temperature T_c below which condensation occurs. The population of excited particles at a given temperature is given by Eq. (2.16). For $T > T_c$, this is sufficient to accommodate all of the particles, and the gas is in the normal phase. As temperature is lowered, however, the excited state capacity also decreases. At the point where the excited states no longer accommodate all the particles, Bose–Einstein condensation occurs. The critical temperature is obtained by setting $z = 1$ in Eq. (2.16) and rearranging for T,

$$T_c = \frac{h^2}{2\pi m k_B} \left(\frac{N}{\zeta(\frac{3}{2})\mathcal{V}} \right)^{\frac{2}{3}}. \tag{2.18}$$

For further decreases in temperature, N_{ex} decreases and so more and more particles must enter the ground state. In the limit $T \to 0$, excited states can carry no particles and all particles enter the condensate.

2.5.5 Condensate Fraction

A useful quantity for characterising the gas is the *condensate fraction*, that is, the proportion of particles which reside in the condensate, N_0/N. Let us consider its variation with temperature. Writing $N = N_0 + N_{ex}$ leads to,

$$\frac{N_0}{N} = 1 - \frac{N_{ex}}{N}. \tag{2.19}$$

For $T \leq T_c$, the excited population N_{ex} is given by Eq. (2.16) with $z = 1$, and the total population is given by Eq. (2.14) with $z = 1$ and $T = T_c$. Substituting both into the above gives,

$$\frac{N_0}{N} = 1 - \left(\frac{T}{T_c} \right)^{3/2}. \tag{2.20}$$

For $T > T_c$, we expect $N_0/N \approx 0$. This behaviour is shown in Fig. 2.9.
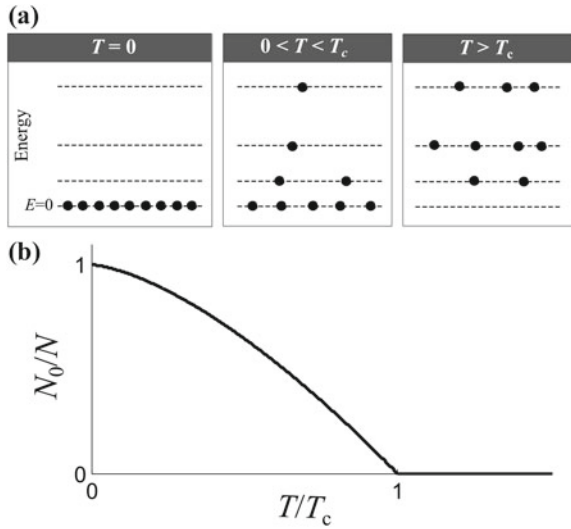
2.5.6 Particle-Wave Overlap

Bose–Einstein condensation occurs when $N > N_c$, with N_c given by Eq. (2.17). It is equivalent to write this criterion in terms of the number density of particles, $n = N/\mathcal{V}$, as,

$$n > \zeta\left(\frac{3}{2}\right) \frac{(2\pi m k_B T)^{3/2}}{h^3}. \tag{2.21}$$

According to de Broglie, particles behave like waves, with a wavelength $\lambda_{dB} = h/p$. For a thermally-excited gas, the particle wavelength is $\lambda_{dB} = \dfrac{h}{\sqrt{2\pi m k_B T}}$. Employing this, the above criterion becomes,

$$n\lambda_{dB}^3 > \zeta\left(\frac{3}{2}\right). \tag{2.22}$$

Upon noting that the average inter-particle distance $d = n^{-\frac{1}{3}}$ and $\zeta(\frac{3}{2})^{\frac{1}{3}} \sim 1$ we arrive at,

$$\lambda_{dB} \gtrsim d. \tag{2.23}$$

Thus, Bose–Einstein condensation coincides with the condition that the particle waves overlap with each other, as depicted in Fig. 2.10. The individual particles become smeared out into one giant wave of matter, the condensate.
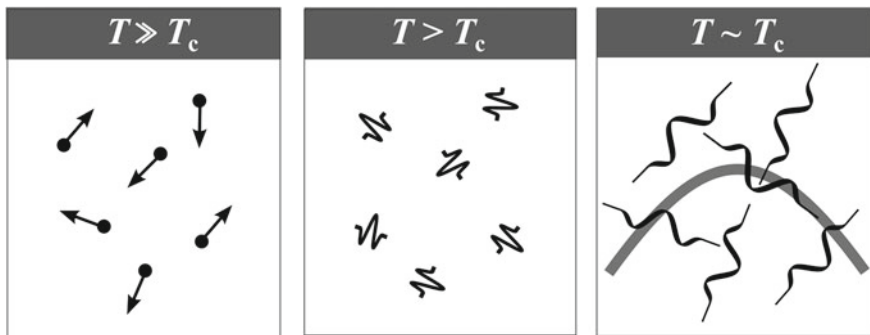
Fig. 2.10 Schematic of the transition between a classical gas and a Bose–Einstein condensate. At high temperatures ($T \gg T_c$) the gas is a thermal gas of point-like particles. At low temperatures (but still exceeding T_c) the de Broglie wavelength λ_{dB} becomes significant, yet smaller than the average spacing d. At T_c, the matter waves overlap ($\lambda_{dB} \sim d$), marking the onset of Bose–Einstein condensation

2.5.7 Internal Energy

The internal energy of the gas U is determined by the excited states only, since the ground state possesses zero energy; therefore we can express U by integrating across the excited state particles as,

$$U = \int_0^\infty E \, N_{ex}(E) \, dE. \tag{2.24}$$

Upon evaluating this integral below and above T_c we find,

$$U = \begin{cases} \dfrac{3}{2} \dfrac{\zeta(5/2)}{\zeta(3/2)} N k_B T \left(\dfrac{T}{T_c}\right)^{3/2} & \text{for } T < T_c, \\ \dfrac{3}{2} N k_B T & \text{for } T \gg T_c. \end{cases} \tag{2.25}$$

The $T \gg T_c$ result is consistent with the classical equipartition theorem for an ideal gas, which states that each particle has on average $\frac{1}{2} k_B T$ of kinetic energy per direction of motion. The different behavior for $T < T_c$ confirms the presence of a distinct state of matter.

2.5.8 Pressure

The pressure of an ideal gas is $P = 2U/3\mathcal{V}$. From Eq. (2.25), then for $T \gg T_c$ we recover the standard result for a classical ideal gas that $P \propto T/\mathcal{V}$. For $T < T_c$, and recalling that $T_c \propto 1/\mathcal{V}^{2/3}$, we find that $P \propto T^{5/2}$. The pressure of the condensate is zero at absolute zero and does not depend on the volume of the box! A consequence of this is that the condensate has infinite compressibility, as explored in Problem 2.6.

2.5.9 Heat Capacity

The heat capacity of a substance is the energy required to raise its temperature by unit amount. At constant volume it is defined as,

$$C_\mathcal{V} = \left(\frac{\partial U}{\partial T}\right)_\mathcal{V}. \tag{2.26}$$

From Eq. (2.25) we find,

$$C_\mathcal{V} = \begin{cases} 1.93 N k_B T^{3/2} & \text{for } T < T_c, \\ \dfrac{3}{2} N k_B & \text{for } T \gg T_c. \end{cases} \tag{2.27}$$

A more precise treatment, describing the dependence at intermediate temperatures, can be found in Ref. [6]. The form of $C_\mathcal{V}(T)$ is depicted in Fig. 2.11, showing a cusp-like dependence around T_c. In general, discontinuities in the gradient of $C_\mathcal{V}(T)$ are signatures of phase transitions between distinct states of matter. The similarity of
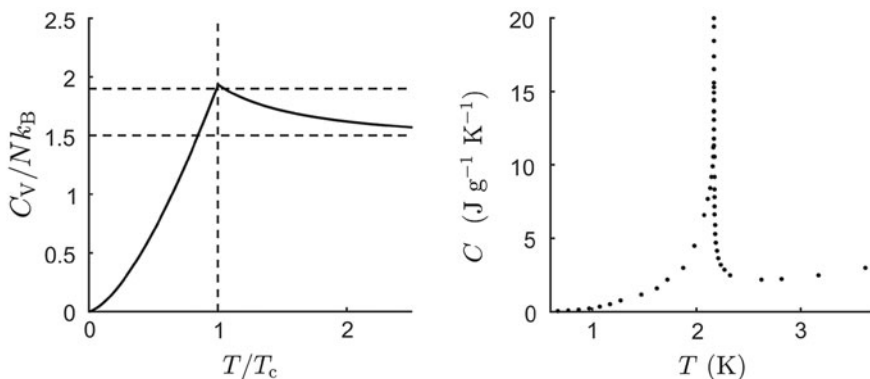
Fig. 2.11 *Left* Heat capacity $C_\mathcal{V}$ of the ideal Bose gas as a function of temperature T. *Right* Experimental heat capacity data of liquid Helium, taken from [7], about the λ-point of 2.2 K. Both curves show a similar cusped structure

this prediction to measured heat capacity curves for Helium about the λ-point was key evidence in linking helium II to Bose–Einstein condensation.

2.5.10   Ideal Bose Gas in a Harmonic Trap

2.5.10.1   Critical Temperature and Condensate Fraction

In typical experiments, atomic Bose–Einstein condensates are confined by harmonic (quadratic) potentials, rather than boxes,[5] with the general form,

$$V(x, y, z) = \frac{1}{2}m \left(\omega_x^2 x^2 + \omega_y^2 y^2 + \omega_z^2 z^2 \right), \tag{2.28}$$

where m is the atomic mass, and ω_x, ω_y and ω_z are trap frequencies which characterise the strength of the trap in each direction. Here the density of states is modified, being $g(E) = E^2/(2\hbar^3 \omega_x \omega_y \omega_z)$ in 3D. This leads, for example, to a critical temperature of the form,

$$T_c = \frac{\hbar}{k_B} (\omega_x \omega_y \omega_z)^{1/3} \left[\frac{N}{\zeta(3)} \right]^{1/3}, \tag{2.29}$$

and for the condensate fraction to vary with temperature as,

$$\frac{N_0}{N} = 1 - \left(\frac{T}{T_c} \right)^3. \tag{2.30}$$

These predictions agree well with experimental measurements of harmonically-trapped atomic BECs, as seen in Fig. 2.12. This is despite the fact that atomic BECs are not *ideal* but feature significant interactions between atoms.

2.5.10.2   Density Profile

We can deduce the density profile of the (non-interacting) condensate in a harmonic trap as follows. The ground quantum state in a harmonic trap is the ground harmonic oscillator state. For simplicity, assume a spherically-symmetric trap with $\omega_x = \omega_y = \omega_z \equiv \omega_r$. The ground quantum state for a single particle is provided by solving the time-independent Schrödinger equation under this harmonic potential, giving the ground harmonic oscillator wavefunction $\psi(r) = \left(\frac{m\omega}{\pi\hbar} \right)^{3/4} e^{-m\omega r^2/2\hbar}$. The quantity $|\psi(r)|^2$ represents the probability of finding the particle at position r. For a condensate of N_0 such particles, with $N_0 \gg 1$, the particle density profile will follow as,

---

[5]Box-like traps [8, 9] are also possible, and allow the condensate to have uniform density, facilitating comparison with the theory of homogeneous condensates.

$$n(r) = N_0|\psi|^2 = N_0(\hbar\ell_r^2)^{-3/2}e^{-r^2/\ell_r^2}, \tag{2.31}$$

where we have introduced the harmonic oscillator length $\ell_r = \hbar/m\omega_r$ which characterises the width of the density distribution.

We can also deduce the density profile of the thermal gas. Taking the classical limit, the atoms will be distributed over energy according to the Boltzmann distribution $N(E) \propto e^{-E/k_B T}$. The trapping potential $V(r)$ allows us to map energy (potential) to position, leading to a spatial particle distribution,

$$n(r) = N_{ex}(\hbar\ell_{r,th}^2)^{-3/2}e^{-r^2/\ell_{r,th}^2}, \tag{2.32}$$

where $\ell_{r,th} = \sqrt{2k_B T/m\omega_r^2}$ characterises the width of the thermal gas and the profile has been normalized to N_{ex} atoms. For increased temperature, the atoms have higher average energy and climb further up the trap walls, leading to a wider profile. While the profiles of the ideal condensate and ideal thermal gas are both Gaussian in space, their widths have different functional forms. In particular, the width of the thermal gas depends on temperature, whereas the condensate width does not.

The typical experimental protocol to form a BEC proceeds by cooling a relatively warm gas towards absolute zero. Above T_c the gas has a broad thermal distribution, which shrinks during cooling. As T_c is under-passed, the condensate distribution forms. In typical atomic BEC experiments, $\ell_r \ll \ell_{r,th}$, such that this is distinctly narrower than the thermal gas, and the combined density profile is bimodal. Under further cooling, the condensate profile grows (with fixed width) at the expense of the thermal profile, and for $T \ll T_c$ the thermal gas is negligible. In reality, atomic interactions modify the precise shapes of the density profiles but this picture *qualitatively* describes what is observed in experiments (see Figs. 1.3 and 1.4).

2.6   **Ideal Fermi Gas**

We outline the corresponding behaviour of the ideal Fermi gas. Since (identical) fermions are restricted to up to one per state, Bose–Einstein condensation is prohibited, and the Fermi gas behaves very differently as $T \to 0$. At $T = 0$ the Fermi-Dirac distribution (2.7) reduces to a step function,

$$f_{\text{FD}}(E) = \begin{cases} 1 & \text{for } E \le E_{\text{F}}, \\ 0 & \text{for } E > E_{\text{F}}. \end{cases} \tag{2.33}$$

All states are occupied up to an energy threshold E_{F}, termed the *Fermi energy* (equal to the $T = 0$ chemical potential). With this simplified distribution it is straightforward to integrate the number of particles,

$$N = \int N(E) \, \mathrm{d}E = \int_0^{E_{\text{F}}} g(E) \, f_{\text{FD}}(E) \, \mathrm{d}E = \frac{4\pi \mathcal{V}}{3} \left(\frac{2m E_{\text{F}}}{h^2} \right)^{3/2}, \tag{2.34}$$

where we have used the density of states (2.13). Note that the continuum approximation $N = \int g(E) \, N(E) \, \mathrm{d}E$ holds for $N \gg 1$ fermions since the unit occupation of the ground state is always negligible. Rearranging for the Fermi energy in terms of the particle density $n = N/\mathcal{V}$ gives,

$$E_{\text{F}} = \frac{\hbar^2}{2m} \left(6\pi^2 n \right)^{2/3}. \tag{2.35}$$

From this we define the Fermi momentum $p_{\text{F}} = \hbar k_{\text{F}}$ where $k_{\text{F}} = (6\pi^2 n)^{1/3}$ is the Fermi wavenumber. In momentum space, all states are occupied up to momentum p_{F}, termed the *Fermi sphere*.

Similarly, the total energy of the gas at $T = 0$ is,

$$U = \int N(E) E \, \mathrm{d}E = \frac{4\pi \mathcal{V}}{5} \left(\frac{2m}{h^2} \right)^{3/2} E_{\text{F}}^{5/2} = \frac{3}{5} N E_{\text{F}}. \tag{2.36}$$

From the pressure relation for an ideal gas, $P = 2U/3\mathcal{V}$, the pressure of the ideal Fermi gas at $T = 0$ is,

$$P = \frac{2}{5} n E_{\text{F}}. \tag{2.37}$$

This pressure is finite even at $T = 0$, unlike the Bose and classical gases, and does not arise from thermal agitation. Instead it is due to the stacking up of particles in energy levels, as constrained by the quantum rules for fermions. This *degeneracy pressure* prevents very dense stars, such as neutron stars, from collapsing under their own gravitational fields.
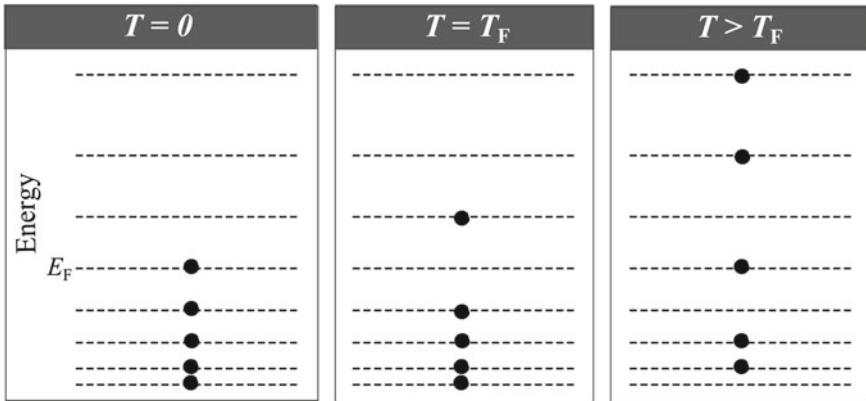
Fig. 2.13 Energy level occupations for an ideal Fermi gas. At $T = 0$, there is unit occupation of states up to the Fermi energy. At $T = T_F$, there is some excitation of states around $E = E_F$. For $T \gg T_F$, the system approaches the classical limit, with particles occupying many high-energy states

As temperature is increased from zero, the step-like Fermi-Dirac distribution becomes broadened about $E = E_F$, representing that some high energy particles become excited to energies exceeding E_F. It is useful to define the *Fermi temperature* $T_F = E_F/k_B$. At low temperatures $T \sim T_F$, only particles in states close to E_F can be excited out of the Fermi sphere, and the system is still dominated by the stacking of particles. For high temperatures $T \gg T_F$, there is significant excitation of most particles, thermal effects dominates, and the system approaches the classical Boltzmann result. The Fermi temperature is associated with the onset of degeneracy, i.e. when quantum effects dominate the system. These regimes are depicted in Fig. 2.13.

Now consider the Fermi gas to be confined in a harmonic trap. For $T \gg T_F$ the gas will have a broad, classical profile. As T is decreased, the profile will narrow but eventually saturates below T_F due to degeneracy pressure. The width of the Fermi gas at zero temperature is proportional to $N^{1/6}\ell_r$ [11], such that, for $N \gg 1$, this cloud is much wider than its classical and Bose counterparts. This picture is confirmed by the experimental images in Fig. 1.4.

2.7   Summary

In his 1925 prediction of Bose–Einstein condensation of an ideal gas, Einstein suggested hydrogen, helium and the electron gas were the best candidates for observing Bose–Einstein condensation. However, the former candidates are no longer gases at the required densities, and the latter (as soon realized) is fermionic. For over a decade, Bose–Einstein condensation had "the reputation of having only a purely

imaginary character" [12], deemed too fragile to occur in real gases with their finite size and particle interactions. In 1938 Einstein's idea became revived when Fritz London recognized the similarity to the heat capacity curves in Helium as it entered the superfluid phase. It took several more decades to cement this link with microscopic theory. Bose–Einstein condensation is now know to underly superfluid He^4 and He^3, superconductors and the ultracold atomic Bose gases. We explore the latter in the next chapter.

Problems

2.1 Consider a system with 6 classical particles, total energy of 6ϵ, and 7 cells with energies $0, \epsilon, 2\epsilon, 3\epsilon, 4\epsilon, 5\epsilon$ and 6ϵ. Complete the table below by entering the cell populations for each macrostate, the statistical weighting for each macrostate W, and the average population per cell $\bar{N}(E)$ (averaged over macrostates). What is the most probable macrostate? Plot $\bar{N}(E)$ versus E. It should be evident that the average distribution approximates the Boltzmann distribution, despite the small number of particles.

	Macrostates		
Cell energy E	$1 \cdots$	11	$\bar{N}(E)$
6ϵ	$? \cdots$	?	?
5ϵ	$? \cdots$	?	?
$\vdots$	$\vdots \cdots$	$\vdots$	$\vdots$
ϵ	$? \cdots$	?	?
0	$? \cdots$	?	?
Statistical weighting W	$? \cdots$	?	

2.2 Consider a system with N classical particles distributed over 3 cells (labelled 1, 2, and 3) of energy $0, \epsilon$ and 2ϵ. The total energy is $E = 0.5N\epsilon$.

(a) Obtain an expression for the number of microstates in terms of N and N_3, the population of cell 3.
(b) Plot the number of microstates as a function of N_2 (which parameterises the macrostate) for $N = 50$. Repeat for $N = 100$ and 500. Note how the distribution changes with N. What form do you expect the distribution to tend towards as N is increased to much larger values?

2.3 Consider an ideal gas of bosons in two dimensions, confined within a two-dimensional box of volume $\mathcal{V}_{2D}$.

(a) Derive the density of states $g(E)$ for this two-dimensional system.
(b) Using this result show that the number of particles can be expressed as,

$$N_{\mathrm{ex}} = \frac{2\pi m \mathcal{V}_{2D} k_\mathrm{B} T}{h^2} \int_0^\infty \frac{ze^{-x}}{1 - ze^{-x}} dx,$$

where $z = e^{\mu/k_\mathrm{B}T}$ and $x = E/k_\mathrm{B}T$. Solve this integral using the substitution $y = ze^{-x}$.

(c) Obtain an expression for the chemical potential μ and thereby show that Bose–Einstein condensation is possible only at $T = 0$.

2.4 Equation (2.25) summarizes how the internal energy of the boxed 3D ideal Bose gas scales with temperature. Derive the full expressions for the internal energy for the two regimes (a) $T < T_\mathrm{c}$ (for which $z = 1$), and (b) $T \gg T_\mathrm{c}$ (for which $z \ll 1$). Extend your results to derive the expressions for the heat capacity given in Eq. (2.27).

2.5 Bose–Einstein condensates are typically confined in harmonic trapping potentials, as given by Eq. (2.28). Using the corresponding density of states provided in Sect. 2.5.10.1:

(a) Derive the expression for the critical number of particles.
(b) Derive the expression (2.29) for the critical temperature.
(c) Determine the expression (2.30) for the variation of condensate fraction N_0/N with T/T_c.
(d) In one of the first BEC experiments, a gas of $40,000$ Rubidium-87 atoms (atomic mass 1.45×10^{-25} kg) underwent Bose–Einstein condensation at a temperature of 280 nK. The harmonic trap was spherically-symmetric with with $\omega_r = 1130$ Hz. Calculate the critical temperature according to the ideal Bose gas prediction. How does this compare to the result for the boxed gas (you may assume the atomic density as 2.5×10^{18} m^{-3}).

2.6 The compressibility β of a gas, a measure of how much it shrinks in response to a compressional force, is defined as,

$$\beta = -\frac{1}{\mathcal{V}} \frac{\partial \mathcal{V}}{\partial P}.$$

Determine the compressibility of the ideal gas for $T < T_\mathrm{c}$.

Hint: Since T_c is a function of $\mathcal{V}$, you should ensure the full $\mathcal{V}$-dependence is present before differentiating.

References

1. F. Mandl, *Statistical Physics*, 2nd edn. (Wiley, Chichester, 1988)
2. L.D. Landau, E.M. Lifshitz, *Statistical Physics*, 3rd edn. (Elsevier, Oxford, 1980)
3. S.N. Bose, Z. Phys. **26**, 178 (1924)
4. A. Einstein, Kgl. Preuss. Akad. Wiss. **261** (1924)
5. A. Einstein, Kgl. Preuss. Akad. Wiss. **3** (1925)

6. L.P. Pitaevskii, S. Stringari, *Bose-Einstein Condensation (International Series of Monographs on Physics)* (Oxford Science Publications, Oxford, 2003)
7. M.J. Buckingham, W.M. Fairbank, The nature of the lambda-transition in liquid helium, in *Progress in Low Temperature Physics*, vol. 3, ed. by C.J. Gorter (North Holland, Amsterdam, 1961)
8. A.L. Gaunt, T.F. Schmidutz, I. Gotlibovych, R.P. Smith, Z. Hadzibabic, Phys. Rev. Lett. **110**, 200406 (2013)
9. L. Chomaz et al., Nat. Comm. **6**, 6162 (2015)
10. J.R. Ensher, D.S. Jin, M.R. Matthews, C.E. Wieman, E.A. Cornell, Phys. Rev. Lett. **77**, 4984 (1996)
11. D.A. Butts, D.S. Rokhsar, Phys. Rev. A **55**, 4346 (1997)
12. F. London, Nature **141**, 643 (1938)

Chapter 3
Gross-Pitaevskii Model of the Condensate

Abstract The Gross-Pitaevskii equation (GPE) is a successful and well-established model for describing an atomic Bose-Einstein condensate. Here we introduce this model, along with its assumptions. Throughout the rest of this chapter we explore its properties and key time-independent solutions.

3.1 The Gross-Pitaevskii Equation

We assume that the gas is at zero temperature, such that the thermal gas and thermally-driven excitations of the condensate are non-existent. This is valid for $T \ll T_c$, which is often satisfied in BEC experiments. In any real gas, the particles also interact with each other, deviating from the ideal gas predictions of Chap. 2. Particle interactions amplify the fluctuations in any quantum field (so-called "quantum fluctuations"); these excite particles out of the ground state and deplete the condensate. An exact description of N interacting quantum particles would proceed by parameterising the system by an N-body wavefunction, $\mathbf{\Psi}(\mathbf{r}_1, \mathbf{r}_2, \ldots, \mathbf{r}_N, t)$, which obeys the many-body Schrödinger equation. However, the complexity of this approach makes it intractable for modelling more than a few particles, let alone the thousands or millions typical of an atomic BEC.

Fortunately, the interactions in atomic BECs are weak; this is due to their extreme diluteness and the weak forces between neutral atoms. As such, quantum fluctuations have a weak effect on the condensate, and will be ignored. Then, and assuming a large number of particles ($N \gg 1$), the many-body wavefunction can be approximated by an effective single-particle wavefunction, $\Psi(\mathbf{r}, t)$. Given the physical picture of the condensate as a giant matter wave (see Sect. 2.5.6), it is natural to describe it via a single wavefunction. This *macroscopic wavefunction* is a complex field that can be written as,

$$\Psi(\mathbf{r}, t) = \sqrt{n(\mathbf{r}, t)} \exp\left[i S(\mathbf{r}, t)\right], \tag{3.1}$$

where n and S are the density and phase distributions of the condensate, and is normalized to N atoms, i.e.,

$$\int |\Psi|^2 \, \mathrm{d}^3\mathbf{r} = N. \tag{3.2}$$

In the absence of interactions, this wavefunction would be governed by the single-particle Schrödinger equation, $i\hbar\partial\Psi/\partial t = [-(\hbar^2/2m)\nabla^2 + V(\mathbf{r}, t)]\Psi$, where ∇^2 is the Laplacian operator and $V(\mathbf{r}, t)$ is the potential acting on the wavefunction (which, in general, may depend on position and time). However, the governing equation must be modified to account for the interactions between atoms. The gas is sufficiently dilute that three-body (and higher) interactions are typically negligible. The dominant interactions are elastic two-body interactions arising from van der Waals forces between the neutral atoms. For two atoms at positions $\mathbf{r_1}$ and $\mathbf{r_2}$ this interaction is well-described by the contact (hard-sphere) interaction,

$$\mathcal{U}(\mathbf{r_1} - \mathbf{r_2}) = g\delta(\mathbf{r_1} - \mathbf{r_2}), \tag{3.3}$$

where δ is Dirac's delta function, and the coefficient g is given by,

$$g = \frac{4\pi\hbar^2 a_\mathrm{s}}{m}. \tag{3.4}$$

Here a_s is the *s-wave scattering length*, a quantity used in atomic physics for characterising the interactions of atoms in the low energy limit (for a detailed description see, e.g. Ref. [1]). For the two most common BEC atomic species, ^{87}Rb and ^{23}Na, $a_\mathrm{s} = 5.8$ and $2.8\,\mathrm{nm}$, respectively. While the true interaction potential between two atoms is more complicated, its detailed shape is unimportant provided that $a_\mathrm{s} \ll d$, where d is the average interparticle distance (or, equivalently, $na_\mathrm{s}^3 \ll 1$). Furthermore, within this picture, the condition for weak interactions is $a_\mathrm{s} \ll \lambda_\mathrm{dB}$.

Taking into account these interactions, the mean-field wavefunction $\psi(\mathbf{r}, t)$ can be shown to satisfy a modified Schrödinger equation called the *Gross-Pitaevskii equation*,

$$i\hbar\frac{\partial\Psi}{\partial t} = -\frac{\hbar^2}{2m}\nabla^2\Psi + V(\mathbf{r}, t)\Psi + g|\Psi|^2\Psi. \tag{3.5}$$

The formal derivation of the GPE is beyond our scope but can be found in, e.g. [1–3]. The first two terms on the right-hand side are familiar from the Schrödinger equation, accounting for kinetic and potential energy. The cubic term $g|\Psi|^2\Psi$ arises from the atomic interactions and makes the equation *nonlinear*. Similar *Nonlinear Schrödinger Equations (NLSEs)* arise in optics, plasma physics and water waves. In one spatial dimension, the NLSE has special mathematical properties, such as soliton solutions and infinite conservation laws (see Chap. 4). The physical interpretation of the nonlinear term is that, at a given point in space, there is an energy contribution arising from the mean-field interactions of all the atoms in the immediate vicinity. The quantity g depends on the given atomic species and can be positive or negative.

Experimentalists can also control sign and magnitude of g using Feshbach resonances. Here magnetic fields are used to couple the two-body scattering to a bound state; when this coupling is close to some resonant magnetic field, huge changes in the two-body scattering properties are possible. For $g > 0$ the interactions are *repulsive*, for $g < 0$ the interactions are attractive, and for $g = 0$ there are no interactions (and the equation reduces to the Schrödinger equation). The case of repulsive interaction is the most studied, so, unless we explicitly specify the sign of g, we take $g > 0$ hereafter.

The GPE can also be extended to take thermal and quantum effects into account, and further information can be found in Refs. [4–6].

3.1.1 Mass, Energy and Momentum

The total mass of the condensate is $M = mN$, where N is provided by the normalization condition on Ψ, Eq. (3.2).

The energy is,

$$E = \int \left[\frac{\hbar^2}{2m} |\nabla \Psi|^2 + V|\Psi|^2 + \frac{g}{2}|\Psi|^4 \right] d^3\mathbf{r} = E_{kin} + E_{pot} + E_{int}. \qquad (3.6)$$

The terms represent (from left to right) *kinetic energy* E_{kin}, *potential energy* E_{pot} and *interaction energy* E_{int}. Providing that the potential V is independent of time, then the energy $E = E_{kin} + E_{pot} + E_{int}$ is conserved during the time evolution of the condensate.

It can be useful, particularly when determining the energy numerically, to define $\Psi = \Psi_r + i\Psi_i$, where Ψ_r and Ψ_i are the real and imaginary parts of the wavefunction. Then, the $|\nabla\Psi|^2$ term in the energy can be expressed in a more convenient form, $|\nabla\Psi|^2 = (\nabla\Psi_r)^2 + (\nabla\Psi_i)^2$.

Meanwhile the momentum of the condensate is,

$$\mathcal{P} = \frac{i\hbar}{2} \int \left(\Psi\nabla\Psi^* - \Psi^*\nabla\Psi \right) d^3\mathbf{r}. \qquad (3.7)$$

3.2 Time-Independent GPE

Time-independent solutions of the GPE satisfy,

$$\Psi(\mathbf{r}, t) = \psi(\mathbf{r})e^{-i\mu t/\hbar}, \qquad (3.8)$$

where μ is a constant called the *chemical potential*. The exponential term represents the freedom for the phase to freely evolve with time, uniformly across the system,

while the density $n(\mathbf{r}, t) = |\psi(\mathbf{r})|^2$ is unaffected. Inserting Eq. (3.8) into Eq. (3.5), we obtain the *time-independent GPE* for the time-independent wavefunction $\psi(\mathbf{r})$,

$$\mu\psi = -\frac{\hbar^2}{2m}\nabla^2\psi + V(\mathbf{r})\psi + g|\psi|^2\psi. \tag{3.9}$$

Note that the potential V must be independent of time here. Solutions of the time-independent GPE are stationary solutions of the system, and the lowest energy solution is the ground state of the BEC. $\psi(\mathbf{r})$ is real for the simple solutions that we discuss in this Chapter.

The chemical potential is the eigenvalue of time-independent GPE, and direct integration leads to the expression,

$$\mu = \frac{1}{N}(E_{\text{kin}} + E_{\text{pot}} + 2E_{\text{int}}). \tag{3.10}$$

In the absence of interactions, this reduces to the energy per particle, consistent with the eigenvalue of the time-independent Schrödinger equation. More generally, the chemical potential is defined as $\mu = \partial E/\partial N$.

3.3   Fluid Dynamics Interpretation

There is a deep link between the GPE and fluid dynamics. Indeed, we can picture the condensate as a fluid, characterised by its density and velocity distributions. From the earlier relation, $\Psi(\mathbf{r}, t) = \sqrt{n(\mathbf{r}, t)}e^{iS(\mathbf{r},t)}$ (known in this context as the *Madelung transform*) the number density follows as $n(\mathbf{r}, t) = |\Psi(\mathbf{r}, t)|^2$. From this relation we have also the *mass density* $\rho(\mathbf{r}, t)$ conventionally used in fluid dynamics, $\rho(\mathbf{r}, t) = m\,n(\mathbf{r}, t)$.

The fluid velocity field $\mathbf{v}(\mathbf{r}, t)$ is defined from the phase via,

$$\mathbf{v}(\mathbf{r}, t) = \frac{\hbar}{m}\nabla S(\mathbf{r}, t). \tag{3.11}$$

Using the Madelung transform $\Psi = \sqrt{n}e^{iS}$ and the above velocity relation, we find that the energy integral of Eq. (3.6) can be written as,

$$E = \int \left[\frac{\hbar^2}{2m}\left(\nabla\sqrt{n}\right)^2 + \frac{mnv^2}{2} + Vn + \frac{gn^2}{2}\right] d^3\mathbf{r}. \tag{3.12}$$

The first two terms comprise the kinetic energy. The first of these is the quantum kinetic energy. It arises due to the zero-point motion of confined particles, and vanishes for a uniform system. The second term is the conventional kinetic energy associated with the flow of the fluid.

Inserting the Madelung transform into the GPE, and separating real and imaginary terms, we obtain two equations. The first is the classical *continuity equation*,

$$\frac{\partial n}{\partial t} + \nabla \cdot (n\mathbf{v}) = 0. \tag{3.13}$$

The continuity equation expresses conservation of the number of atoms (or, when written in terms of $\rho(\mathbf{r}, t)$, conservation of mass). By integrating the equation over a given volume, we see that, if the number of atoms changes in that volume, it is because fluid has moved in or out of it.

The second equation is,

$$m\frac{\partial \mathbf{v}}{\partial t} = -\nabla \left(\frac{1}{2}mv^2 + V + gn - \frac{\hbar^2}{2m}\frac{\nabla^2\sqrt{n}}{\sqrt{n}} \right). \tag{3.14}$$

The $\nabla^2\sqrt{n}/\sqrt{n}$ term is termed the *quantum pressure* term (see below). With some manipulation, we can write this in the equivalent form,

$$mn\left(\frac{\partial \mathbf{v}}{\partial t} + (\mathbf{v} \cdot \nabla)\mathbf{v} \right) = -\nabla(P + P') - n\nabla V, \tag{3.15}$$

where P and P' are respectively the *pressure* and the *quantum pressure*,

$$P = \frac{gn^2}{2}, \qquad P' = -\frac{\hbar^2}{4m}n\nabla^2(\ln n). \tag{3.16}$$

Equations (3.13) and (3.14) (or, equivalently, Eqs. (3.13) and (3.15)) are known as the *superfluid hydrodynamic equations*. They can also be written in index notation.[1]

Notice that the pressure depends only on the density. This property makes the condensate a *barotropic fluid*; as a consequence, surfaces of constant pressure are also surfaces of constant density. The quantum pressure is a pure quantum effect, and vanishes if we set Planck's constant equal to zero. It has the same origin as the quantum kinetic energy, i.e. zero point motion, which creates a pressure that opposes any 'squashing' or 'bending' of the condensate. In a uniform condensate the quantum pressure is zero because n is constant.

Equation (3.15) is very similar to the classical Euler equation for an inviscid fluid. To understand the relation between condensates and classical fluids, we compare the relative importance of pressure and quantum pressure. Using Eq. (3.16), we estimate

---

[1] In index notation, Eqs. (3.13) and (3.15) are $\dfrac{\partial n}{\partial t} + \dfrac{\partial(nv_j)}{\partial x_j} = 0$ and $mn\left(\dfrac{\partial v_k}{\partial t} + v_j\dfrac{\partial v_k}{\partial x_j} \right) = -\dfrac{\partial P}{\partial x_k} - \dfrac{\partial P'_{jk}}{\partial x_j} - n\dfrac{\partial V}{\partial x_k}$, where v_j is the jth Cartesian component ($j = 1, 2, 3$) of the velocity $\mathbf{v}$, we have assumed summation over repeated indices, and that the components P'_{jk} of the quantum stress tensor P' are $P'_{jk} = -\dfrac{\hbar^2}{4m}n\dfrac{\partial^2(\ln n)}{\partial x_j \partial x_k}$.

that the order of magnitude of P and P' are respectively $P \sim gn^2$ and $P' \sim \hbar^2 n/m\xi^2$, where ξ is the length scale of the variations of n. Then $P'/P \sim \hbar^2/(mng\xi^2)$, and hence the quantum pressure becomes negligible ($P' \ll P$) in the limit of length scales larger than ξ. If in addition, the trapping potential is absent ($V = 0$) then Eq. (3.15) become negligible, and the equation reduces to the classical Euler equation, which describes the motion of a classical fluid without viscosity.

The lengthscale in question is provided by the *healing length*, defined as,

$$\xi = \frac{\hbar}{\sqrt{gmn}}. \tag{3.17}$$

The typical value of the healing length in atomic BECs is $\xi \sim 10^{-6}$ m; for superfluid helium (^{4}He) the healing length is much smaller, $\xi \sim 10^{-10}$ m.

3.4 Stationary Solutions in Infinite or Semi–infinite Homogeneous Systems

In experiments, atomic condensates are confined by bowl-like trapping potentials $V(\mathbf{r})$. Condensates are therefore small (typically of the order of 10^{-5} or 10^{-4} m) and inhomogeneous (the density depends on the position). However, many general properties of atomic condensates can be understood from the simpler scenario of a homogeneous condensate in an infinitely-sized or semi-infinitely-sized system. The homogeneous condensate is also a useful model of superfluid helium, as the sizes of the samples of ^{4}He typically used in experiments range from 10^{-2} to 10^{-1} m, many orders of magnitude larger than the healing length. A homogeneous condensate would not be stable for $g < 0$ (as we see later) and so we consider $g > 0$ for now.

3.4.1 Uniform Condensate

For $V = 0$ (uniform condensate of infinite extent), the stationary solution is uniform, and the time-independent GPE becomes,

$$\mu\psi = g|\psi|^2\psi. \tag{3.18}$$

The solution is then,

$$\psi = \psi_0 = \sqrt{\mu/g}. \tag{3.19}$$

The corresponding number and mass densities are, respectively,

$$n = n_0 = |\psi_0|^2 = \mu/g, \qquad \rho = \rho_0 = m\mu/g. \tag{3.20}$$

3.4.2 Condensate Near a Wall

Consider a *one-dimensional hard wall* defined by,

$$V(x) = \begin{cases} \infty & \text{for } x < 0, \\ 0 & \text{for } x \geq 0. \end{cases}$$

No atoms exist in the region $x < 0$ (since this would require infinite energy), and so the boundary condition at $x = 0$ is $\psi(0) = 0$. Away from the wall (in the positive x direction) the condensate must recover its bulk form, giving the second boundary condition that $\psi(x) \to \psi_0 = \sqrt{\mu/g}$ for $x \to \infty$. In the semi-infinite region $x \geq 0$ the one-dimensional (1D) time-independent GPE is,

$$\mu\psi = -\frac{\hbar^2}{2m}\frac{\partial^2\psi}{\partial x^2} + g|\psi|^2\psi. \tag{3.21}$$

The solution of this equation which satisfies the boundary conditions is,

$$\psi(x) = \psi_0 \tanh\left(\frac{x}{\xi}\right). \tag{3.22}$$

The meaning of the healing length ξ is now apparent: it is the characteristic minimal distance over which ψ changes spatially. The 'healing' profile is supported at a wall by the balance between the kinetic energy term in the GPE and the interaction term. Denoting the spatial scale of the variation in the wavefunction as ξ, these terms are of the order of $\hbar^2/m\xi^2$ and gn_0, respectively. Equating these terms and rearranging leads to $\xi = \hbar/\sqrt{mn_0 g}$, the healing length as defined in Eq. (3.17). Note that the healing length is sometimes defined with a $\sqrt{2}$ in the denominator.
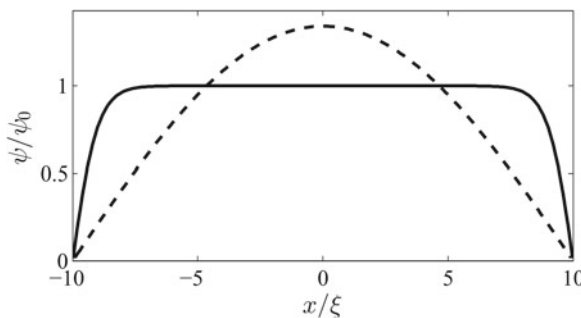
Fig. 3.1 Condensate wavefunction ψ (in units of ψ_0) as a function of position x (in units of ξ) within a 1D infinite square well of width (here with width 20ξ). Shown are the profiles for a non-interacting condensate ($g = 0$) and aAtomic condensates repulsively-interacting ($g > 0$) condensate. Note how the wavefunction "heals" at each boundary according to Eq. (3.22), recovering its bulk density at a distance from the wall of the order of few times the healing length ξ

In an infinite square well of width L_0, which is much wider than the healing length ($L_0 \gg \xi$), we then expect the wavefunction to 'heal' at each boundary, according to Eq. (3.22), and reach the bulk value in the centre of the well. This is shown in Fig. 3.1.

It is interesting to compare this to the case of $g = 0$, for which the ground state is given by the well-known solution of the Schrödinger equation for a particle in an infinite well, $\psi \sim \sin(\pi x/L_0)$. Clearly the interactions between the atoms broaden and flatten the density profile by increasing the energetic cost of concentrating atoms in one place.

3.5   Stationary Solutions in Harmonic Potentials

Atomic condensates are typically confined by harmonic potentials which may, in general, be anisotropic in space. For simplicity here we start by considering a spherically-symmetric harmonic trap,

$$V(\mathbf{r}) = \frac{m}{2}\omega_r^2 r^2, \tag{3.23}$$

where $r^2 = x^2 + y^2 + z^2$. The characteristic length scale of this potential is the *harmonic oscillator length*,

$$\ell_r = \sqrt{\hbar/m\omega_r}. \tag{3.24}$$

There is no general analytic solution for the ground state (lowest energy) solution of the BEC in a harmonic trap; usually the ground state is found by numerically solving Eq. (3.9). However, there exist useful analytic results for certain regimes which we describe below. It is useful to work in terms of the *interaction parameter*,[2] Na_s/ℓ_r. Below we distinguish the following cases: no interactions, strong repulsive interactions ($Na_s/\ell_r \gg 1$) and weak interactions ($|Na_s/\ell_r| \ll 1$).

3.5.1   No Interactions

In the absence of atomic interactions ($g = 0$) the time-independent GPE reduces to the Schrödinger equation,

$$\mu\psi = -\frac{\hbar^2}{2m}\nabla^2\psi + \frac{m\omega_r^2 r^2}{2}\psi. \tag{3.25}$$

The ground state harmonic oscillator solution is well-known to be a three-dimensional Gaussian wave function,

---

[2]More generally, for an anisotropic harmonic trap, the corresponding interaction parameter is $Na_s/\bar{\ell}$, where $\bar{\ell} = \sqrt{\hbar/m\bar{\omega}}$ and $\bar{\omega} = (\omega_x\omega_y\omega_z)^{1/3}$ is the geometric mean of the trap frequencies.

$$\psi(\mathbf{r}) = \frac{N^{1/2}}{\pi^{3/4}\ell_r^{3/2}} \exp\left(-\frac{r^2}{2\ell^2}\right). \tag{3.26}$$

Using Eq. (3.6), one can show that this has the expected 3D harmonic oscillator energy $E = \frac{3}{2}N\hbar\omega_r$.

3.5.2 Strong Repulsive Interactions

Let the interactions be strongly repulsive, satisfying $Na_s/\ell_r \gg 1$. We expect a condensate profile which is significantly broadened and flattened due to the repulsive interactions. An analytic solution is found if we neglect the $\nabla^2\psi$-term in the GPE; this is known as the *Thomas-Fermi approximation*. The time-independent GPE simplifies to,

$$\mu\psi = g|\psi|^2\psi + V\psi. \tag{3.27}$$

Substituting $n = |\psi|^2$ and $V(r) = \frac{1}{2}m\omega^2 r^2$, we obtain $n(r) = (2\mu - m\omega_r^2 r^2)/2g$. Density cannot be negative, so we assume that $n(r) = 0$ if $2\mu \le m\omega_r^2 r^2$. The last equality defines the *Thomas-Fermi radius* R_r, which satisfies,

$$\mu = \frac{1}{2}m\omega_r^2 R_r^2. \tag{3.28}$$

We conclude that the Thomas-Fermi density profile is,

$$n(r) = \begin{cases} \dfrac{\mu}{g}\left(1 - \dfrac{r^2}{R_r^2}\right) = \dfrac{m\omega_r^2(R_r^2 - r^2)}{2g} & \text{if } r \le R_r, \\ 0 & \text{if } r > R_r, \end{cases} \tag{3.29}$$

and has the shape of an inverted parabola. Provided that $Na_s/\ell_r \gg 1$, the Thomas-Fermi solution is an excellent approximation of the solution of the GPE determined numerically, and compares well with experimental data, as shown in Fig. 3.2. Note, however, the slight deviation from the true numerical solution close to the condensate's edge; here the gradient terms, neglected within the Thomas-Fermi model, become significant.

The application of the normalization condition, Eq. (3.2), to the above solution and manipulation of the resulting expression leads to useful relations for the chemical potential and the energy of the condensate in terms of the number of atoms N,

$$\mu = \frac{\hbar\omega_r}{2}\left(\frac{15Na_s}{\ell_r}\right)^{2/5}, \quad E = \frac{5}{7}\mu N. \tag{3.30}$$
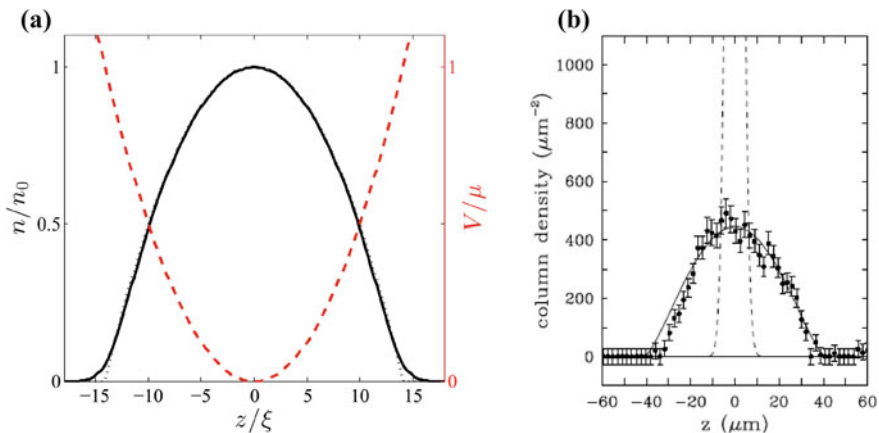
Fig. 3.2   a Density profile $n(z)$ plotted versus position z (in units of the healing length ξ). The agreement between the analytic Thomas-Fermi density profile (*dotted black line*) and the numerically-determined solution of the GPE (*solid black line*) is so good that the lines overlap everywhere but in the tails near $z \approx \pm 15\xi$. The harmonic trapping potential $V(z)$ is indicated by the dashed *red line*. **b** An experimental density profile, compared to the Thomas-Fermi prediction (*solid line*) and the non-interacting prediction (*dashed line*). Reprinted figure with permission from [7]. Copyright 1999 by the American Physical Society

The latter is obtained from the relation $\mu = \partial E/\partial N$. Since $Na_s/\ell_r \gg 1$, it is evident that in the Thomas-Fermi regime the chemical potential and energy per particle are considerably greater than the typical trap energy $\hbar\omega_r$.

In the more general case where the harmonic potential is anisotropic in space, $V(x, y, z) = m(\omega_x^2 x^2 + \omega_y^2 y^2 + \omega_z^2 z^2)/2$, the Thomas-Fermi boundary is an ellipsoidal surface satisfying the equation,

$$\frac{x^2}{R_x^2} + \frac{y^2}{R_y^2} + \frac{z^2}{R_z^2} = 1, \tag{3.31}$$

where the three Thomas-Fermi radii R_x, R_y and R_z satisfy,

$$\mu = \frac{1}{2}m\omega_x^2 R_x^2 = \frac{1}{2}m\omega_y^2 R_y^2 = \frac{1}{2}m\omega_z^2 R_z^2. \tag{3.32}$$

In this anisotropic case, it is most convenient to write the density profile as,

$$n(x, y, z) = \begin{cases} \dfrac{\mu}{g}\left(1 - \dfrac{x^2}{R_x^2} - \dfrac{y^2}{R_y^2} - \dfrac{z^2}{R_z^2}\right), & \text{within the ellipsoid,} \\ 0 & \text{elsewhere.} \end{cases} \tag{3.33}$$

From this the anisotropic versions of the chemical potential and energy, Eq. (3.30), can be determined.

3.5.3 Weak Interactions

The following variational approach determines an approximate solution of the time-independent GPE in a harmonic potential when the interactions (either positive or negative) are weak, that is $|Na_s/\ell_r| < 1$.

In the limiting case $g = 0$ we know that the exact wavefunction is the Gaussian harmonic oscillator ground state, Eq. (3.26). For weak interactions we assume the following trial wavefunction, or *ansatz*, which is Gaussian in shape but has variable width $\sigma\ell_r$,

$$\psi(\mathbf{r}) = \left(\frac{N}{\pi^{3/2}\sigma^3\ell_r^3} \right)^{1/2} \exp\left(-\frac{r^2}{2\sigma^2\ell_r^2} \right). \tag{3.34}$$

where σ is our *variational parameter*. If $g = 0$ then $\sigma = 1$, i.e. we recover the exact non-interacting result.

Using the energy integral (3.6), the energy of the ansatz is,

$$E(\sigma) = \hbar\omega_r N \left[\frac{3}{4\sigma^2} + \frac{3\sigma^2}{4} + \frac{1}{\sqrt{2\pi}} \left(\frac{Na_s}{\ell_r} \right) \frac{1}{\sigma^3} \right]. \tag{3.35}$$

From left to right, the terms in the bracket represent kinetic energy, potential energy and interaction energy. For a given system (i.e. for specific values of N, ω, a_s and ℓ_r), Eq. (3.35) tells us how the energy varies with σ. The variational solution is defined as the variational state with the lowest energy, i.e. the minimum of $E(\sigma)$; the corresponding width is denoted σ_{min}. Figure 3.3 plots $E(\sigma)$ for various values of the interaction parameter Na_s/ℓ. The behaviour is different depending on whether the interactions are repulsive or attractive:

- For **repulsive interactions** $(g > 0)$, $E(\sigma)$ diverges to infinity for both $\sigma \to 0$ (due to the positive kinetic and interaction energies) and $\sigma \to \infty$ (due to the potential energy), with a global minimum in-between, corresponding to the variational ground state. If $g = 0$, $\sigma_{min} = 1$, corresponding to the non-interacting Gaussian solution. For increasing g, σ_{min} increases, i.e., the condensate becomes wider.
- For **attractive interactions** $(g < 0)$, $E(\sigma)$ now diverges to minus infinity as $\sigma \to 0$. This is due to the dominance of the negative interaction energy in this limit. The lowest energy solution is thus a wavepacket of zero width, i.e. an unstable collapsed state![3] However, for small $|Na_s/\ell_r|$, a *local minimum* exists in $E(\sigma)$ at non-zero width, representing a stable condensate of finite size. For larger $|Na_s/\ell_r|$,

---

[3]In reality, the BEC does not quite collapse to zero width; at high densities, repulsive inter-atomic forces kick-in which cause the condensate to then explode outwards, an effect termed the *bosenova*.
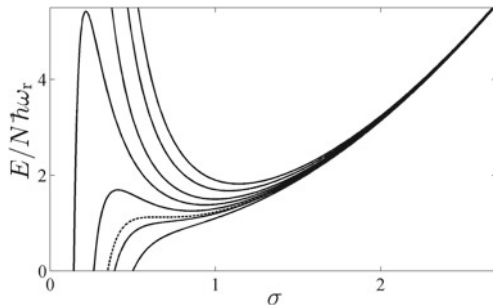
Fig. 3.3 Energy E (in units of $N\hbar\omega_r$) versus σ according to Eq. (3.35) for various values of the interaction parameter Na_s/ℓ_r corresponding, from *top* to *bottom*, to $[-1, -0.75, -0.67, -0.5, -0.25, 0, 0.5, 1]$. $Na_s/\ell_r = -0.67$ (*dashed line*) marks the critical point for the onset of collapse

the local minimum shifts to smaller widths; the attractive interactions cause the condensate to become narrower and more peaked. However, beyond some critical attractive interactions, the local minimum disappears and no stable solutions exist. In other words, all states collapse to zero width. The variational method predicts collapse to occur for $Na_s/\ell_r \leq -0.67$; this is close to the experimentally measured value of $Na_s/\ell_r \leq -0.64$. This tendency to collapse is the reason why repulsive condensates are more common and why we have avoided discussing condensates with attractive interactions so far.

Note that the above-assumed Gaussian profile is just an approximation. In the presence of repulsive interactions, the true condensate profile (e.g. as obtained by numerical solution of the GPE) is broader than a Gaussian (becoming more Thomas-Fermi like for increasing repulsive interactions), while for attractive interactions the shape is narrower and more peaked.

3.5.4 Anisotropic Harmonic Potentials and Condensates of Reduced Dimensionality

The shape of the condensate is determined by the shape of the trapping potential. A spherical harmonic potential induces a spherical condensate. It is also common to encounter elongated, or *cigar-shaped*, condensates and flattened, or *pancake-shaped*, condensates. The former case is achieved if the condensate is more tightly trapped in two directions, e.g. $\omega_x, \omega_y > \omega_z$, and the latter case, if it is more tightly trapped in one direction, e.g. $\omega_z > \omega_x, \omega_y$. These shapes are illustrated in Fig. 3.4.

By making these trap anisotropies more extreme, it is possible to engineer condensates of reduced dimensionality. Consider first a highly elongated trap ($\omega_x, \omega_y \gg \omega_z$). If the transverse trapping potential (which is of energy $\hbar(\omega_x\omega_y)^{1/2}$) is much larger
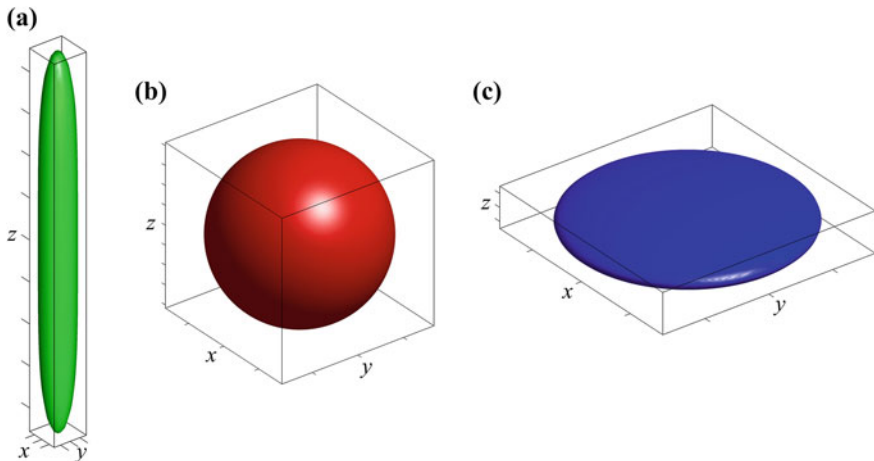
Fig. 3.4 The three most common condensate shapes that can be formed in an axisymmetric harmonic potential: **a** a cigar condensate ($\omega_x, \omega_y > \omega_z$), **b** a spherical condensate ($\omega_x = \omega_y = \omega_z$), and **c** a pancake condensate ($\omega_x, \omega_y < \omega_z$)

than the condensate energy scale (the chemical potential, μ), then excitations of the condensate in the x and y directions are highly suppressed, and the only significant dynamics occur in the z direction. The system has become effectively one-dimensional. An effectively two-dimensional condensate can be realized for $\omega_x, \omega_y \ll \omega_z$ and $\hbar\omega_z \gg \mu$.

In these limits the condensate can be described by suitable one-dimensional and two-dimensional GPEs. The reduction of the full three-dimensional GPE to these forms is straightforward, as we now outline for a one-dimensional system. Assuming the above criteria for an effectively one-dimensional condensate, we take the following ansatz for the condensate wavefunction,

$$\psi(x, y, z, t) = \psi_z(z, t)G_x(x)G_y(y). \tag{3.36}$$

In other words, we have decomposed ψ into independent components along x, y and z. Under the criterion $\hbar(\omega_x\omega_y)^{1/2} \gg \mu$ then the x and y component will be "locked" into the respective ground harmonic oscillator states, which are represented by the Gaussian functions,

$$G_x(x) = \frac{1}{(\pi\ell_x^2)^{1/4}}e^{-x^2/2\ell_x^2}, \qquad G_y(y) = \frac{1}{(\pi\ell_y^2)^{1/4}}e^{-y^2/2\ell_y^2}, \tag{3.37}$$

where $\ell_x = \sqrt{\hbar/m\omega_x}$ and $\ell_y = \sqrt{\hbar/m\omega_y}$ denote the harmonic oscillator lengths along x and y. The time-dependence now only appears in the axial wavefunction, ψ_z. Note that ψ_z is normalized to the number of atoms, i.e. $\int |\psi_z|^2 \, dz = N$; as a result the transverse wavefunctions are both normalized to unity (leading to their pre-factors).

To obtain a 1D GPE, one proceeds by inserting the wavefunction ansatz (3.36) into the 3D GPE and manipulating. Since,

$$\frac{d^2 G_x(x)}{dx^2} = \left(\frac{x^2}{\ell_x^4} - \frac{1}{\ell_x^2} \right) G_x(x), \tag{3.38}$$

and similarly for $G_y(y)$, each term in the GPE acquires a $G_x(x)G_y(y)$ factor. To eliminate these factors, one multiplies the equation through by $G_x^* G_y^*$ (where * denotes complex conjugate) and integrates over all x and y. It is helpful to note that $\int_{-\infty}^{\infty} e^{-x^2} dx = \sqrt{\pi}$. This leads to the following one-dimensional GPE for $\psi_z(z)$,

$$\mu_{1D} \psi_z = -\frac{\hbar^2}{2m} \frac{d^2 \psi_z}{dz^2} + g_{1D} |\psi_z|^2 \psi_z + \frac{1}{2} m \omega_z^2 z^2 \psi_z. \tag{3.39}$$

Here g_{1D} and μ_{1D} are the effective one-dimensional interaction strength and chemical potential, defined as,

$$g_{1D} = \frac{g}{2\pi \ell_x \ell_y}, \qquad \mu_{1D} = \mu - \frac{\hbar \omega_x}{2} - \frac{\hbar \omega_y}{2}. \tag{3.40}$$

Note that the trap geometries are often cylindrically symmetric, with $\omega_x = \omega_y$; this symmetry can simplify the integration steps.

Following similar arguments for an effectively two-dimensional condensate, one obtains the effective two-dimensional GPE for the two-dimensional wavefunction $\psi_{xy}(x, y, t)$,

$$\mu_{2D} \psi_\perp = -\frac{\hbar^2}{2m} \left(\frac{d^2 \psi_\perp}{dx^2} + \frac{d^2 \psi_\perp}{dy^2} \right) + g_{2D} |\psi_\perp|^2 \psi_\perp + \frac{1}{2} m (\omega_x^2 x^2 + \omega_y^2 y^2) \psi_\perp,$$

$$g_{2D} = \frac{g}{\sqrt{2\pi} \ell_z}, \qquad \mu_{2D} = \mu - \frac{\hbar \omega_z}{2}.$$

In this case the two-dimensional wavefunction is normalized according to $\int |\psi_\perp|^2 \, dx dy = N$.

In these one- and two-dimensional cases, the system energy is still described according to Eq. (3.6), with the gradient operator replaced by its one- and two-dimensional equivalents, and the integration taken over one and two dimensions, respectively. Moreover, the same analysis techniques presented for three-dimensional stationary solutions, e.g. the Thomas-Fermi approximation and the Gaussian variational approach, can be employed. In particular, the 1D GPE provides a simplified platform to study many generic properties of condensates, and, for example, its stationary solutions under hard-wall and periodic boundaries are well-established [8, 9]. Note, however, that the system stability can be significantly affected by the dimensionality of the system, for example, collapse under attractive interactions does not occur within the 1D GPE, as will be discussed further in Chap. 4.

Fig. 3.5 Absorption imaging of a BEC. Laser light incident upon the BEC creates a shadow behind it, whose darkness is proportional to the column-integrated density of the BEC
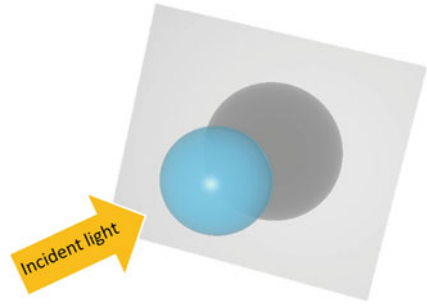
3.6 Imaging and Column-Integrated Density

The most common approach to image a condensate is via optical absorption imaging. The condensate is illuminated by an uniform light beam from one side. The atoms absorb a proportion of the light such that a two-dimensional shadow is cast behind the condensate; this is recorded by camera as shown in Fig. 3.5, forming an *absorption image* of the condensate. Examples are the images in Fig. 1.4. Importantly, the darkness of the shadow is proportional to the atomic density, integrated along the direction light is travelling in[4]; we call this the *column-integrated density*.

To enable comparison between experimental absorption images and theoretical models, one must relate three-dimensional wavefunctions to the corresponding two-dimensional column-integrated density profiles. Assuming imaging in the z-direction, the column-integrated density n_{CI} is,

$$n_{CI}(x, y) = \int_{-\infty}^{\infty} n(x, y, z) \, dz. \tag{3.41}$$

3.7 Galilean Invariance and Moving Frames

A condensate in a homogeneous ($V = 0$) system satisfies the GPE,

$$i\hbar \frac{\partial \Psi}{\partial t} = \left(-\frac{\hbar^2}{2m} \nabla^2 + g|\Psi|^2 \right) \Psi. \tag{3.42}$$

The stationary solution is $\Psi_0 = \sqrt{n_0} \exp\left[-i\mu t/\hbar\right]$, corresponding to a static ($\mathbf{v} = 0$) condensate. Now let us imagine, instead, that this condensate is moving with uniform velocity v_0 in the positive x direction, say. We can construct this moving solution as,

---

[4]Fortunately, the atomic density is so low that scattering of the light beam is negligible and so the light effectively takes a direct path through the condensate.

$$\Psi = \Psi_0(x - v_0 t, y, z) \exp \left[i \frac{m v_0 x}{\hbar} - \frac{m v_0^2 t}{2\hbar} \right]. \tag{3.43}$$

Note that the density remains n_0 throughout. This is a demonstration of *Galilean invariance*, i.e. that the laws of physics are the same in all *inertial frames* (frames moving at fixed relative speed to each other). This is true only if the system is translationally invariant, i.e. the potential is the same everywhere.

Above, we imagine the condensate flowing at speed v_0 relative to the static observer (the *lab frame*). Instead, we can take the observer to be moving with the condensate. We can then write the *moving frame GPE*,

$$i\hbar \frac{\partial \Psi}{\partial t} = \left(-\frac{\hbar^2}{2m} \nabla^2 + g|\Psi|^2 + i\hbar v_0 \frac{\partial}{\partial \tilde{x}} \right) \Psi, \tag{3.44}$$

where $\tilde{x}$ is the x-coordinate in the moving frame and the Laplacian is evaluated in terms of the moving frame coordinates. In this moving frame, the flowing condensate solution of Eq. (3.43) is actually a stationary solution. It can be useful to work in the moving frame when modelling flows of condensates.

3.8   Dimensionless Variables

The typical numbers which appear in the GPE equation are very small and cumbersome, for example the reduced Planck's constant is $\hbar = 1.055 \times 10^{-34}$ Js. When numerically solving the GPE to model a condensate, it would be better if the numbers which we compute were of order unity; this minimises the role of floating point errors which are inherent to modern digital computation. Another problem is that not all the parameters which appear in the GPE are independent: identifying the truly independent parameters reduces the number of numerical simulations which are needed to understand the nature of the solution. It is therefore useful to introduce *dimensionless variables* and write the GPE in simpler *dimensionless form*. To illustrate the procedure, we consider two examples: homogeneous and harmonically-trapped condensates.

Before we start, we notice for the sake of generality that we are free to introduce the chemical potential μ in the time-dependent GPE by letting, in analogy with Eq. (3.8),

$$\Psi(\mathbf{r}, t) = \psi(\mathbf{r}, t) e^{-i\mu t/\hbar}, \tag{3.45}$$

where now $\psi(\mathbf{r}, t)$ depends also on t; in other words, the exponential term takes care of part of (but not all of) the time dependence of the wavefunction. The resulting time-dependent GPE is,

$$i\hbar\frac{\partial\psi}{\partial t} = -\frac{\hbar^2}{2m}\nabla^2\psi + g|\psi|^2\psi + V\psi - \mu\psi. \tag{3.46}$$

3.8.1 Homogeneous Condensate

In the absence of trapping ($V = 0$), the governing equation is

$$i\hbar\frac{\partial\psi}{\partial t} = -\frac{\hbar^2}{2m}\nabla^2\psi + g|\psi|^2\psi - \mu\psi. \tag{3.47}$$

We have seen that the wavefunction of a uniform condensate at rest is $\psi_0 = \sqrt{\mu/g}$, corresponding to the number density $n_0 = \mu/g$. We have also seen that the characteristic minimum distance over which the wavefunction varies is the healing length $\xi = \hbar/\sqrt{m\mu}$. Therefore the quantities n_0 and ξ are convenient units of density and length. Similarly, it is apparent from Eq. (3.8) or Eq. (3.45) that $\tau = \hbar/\mu$ is the natural unit of time. These remarks suggest the introduction of the following dimensionless variables (hereafter denoted by primes):

$$x' = \frac{x}{\xi}, \qquad y' = \frac{y}{\xi}, \qquad z' = \frac{z}{\xi}, \tag{3.48}$$

(in other words, $\mathbf{r}' = \mathbf{r}/\xi$), and

$$t' = \frac{t}{\tau}, \qquad \psi' = \frac{\psi}{\psi_0}. \tag{3.49}$$

To begin substituting these new variables into the GPE, we need to develop relations for their derivatives. Using the chain rule,

$$\frac{d}{dx} = \frac{1}{\xi}\frac{d}{dx'}, \quad \frac{d}{dy} = \frac{1}{\xi}\frac{d}{dy'}, \quad \frac{d}{dz} = \frac{1}{\xi}\frac{d}{dz'}, \quad \frac{d}{dt} = \frac{1}{\tau}\frac{d}{dt'}. \tag{3.50}$$

Hence the gradient and Laplacian operators acting on the primed variables are defined as,

$$\nabla = \frac{1}{\xi}\nabla', \quad \nabla^2 = \frac{1}{\xi^2}\nabla'^2. \tag{3.51}$$

Introducing these relations, Eq. (3.47) becomes the following *dimensionless GPE*,

$$i\frac{\partial\psi'}{\partial t'} = -\frac{1}{2}\nabla'^2\psi' + |\psi'|^2\psi' - \psi'. \tag{3.52}$$

This equation contains no parameters - it has been simplified to its mathematical essence.[5] These units are often termed *natural* or *healing length* units.

3.8.2   Harmonically-Trapped Condensate

Here we assume that the condensate is confined by a spherical harmonic trap $V = m\omega_r^2 r^2/2$. Then the governing equation is,

$$i\hbar\frac{\partial\psi}{\partial t} = -\frac{\hbar^2}{2m}\nabla^2\psi + g|\psi|^2\psi + V\psi - \mu\psi. \tag{3.53}$$

In this case the natural units of length and time are based on the harmonic oscillator length $\ell_r = \sqrt{\hbar/m\omega_r}$ and the inverse of the trap frequency, ω_r^{-1}. We set $\mathbf{r}' = \mathbf{r}/\ell$ (that is to say $x' = x/\ell$, $y' = y/\ell$ and $z' = /\ell$) and $t' = t/\tau$, where $\tau = 1/\omega_r$.

It is conventional with these units to define the dimensionless wavefunction ψ' as being normalized to unity, i.e.,

$$\int |\psi'|^2 d^3\mathbf{r}' = 1. \tag{3.54}$$

Comparing to Eq. (3.2) and noting that $d^3\mathbf{r} = \ell_r^3 d^3\mathbf{r}'$, it follows that $\psi = (N/\ell_r^3)^{1/2}\psi'$.

Introducing these relations into Eq. (3.58) we arrive at the dimensionless form,

$$i\frac{\partial\psi'}{\partial t'} = -\frac{1}{2}\nabla'^2\psi' + C|\psi'|^2\psi' + \frac{r'^2}{2}\psi' - \mu'\psi'. \tag{3.55}$$

where $\mu' = \mu/\hbar\omega_r$ and,

$$C = \frac{4\pi a_s N}{\ell}. \tag{3.56}$$

is a dimensionless interaction parameter. These units are often termed *harmonic oscillator units*. For anisotropic harmonic traps, the harmonic units can be defined instead in terms of one of the trap frequencies or their geometric mean, $\bar{\omega} = (\omega_x\omega_y\omega_z)^{1/3}$.

Problems

3.1 (a) Using the normalization condition, determine the dimensions of the wavefunction Ψ in S.I. units (metres, kilograms, seconds).

---

[5]In the literature, after transforming the GPE into dimensionless form, it is common to drop the primes.

(b) Verify that all terms of the GPE have the same dimension.
(c) Show that $g|\Psi|^2$ has dimension of energy.

3.2 Consider a BEC in the Thomas-Fermi limit, confined within a three-dimensional spherical harmonic trap.
(a) Normalize the wavefunction, and hence determine an expression for the Thomas-Fermi radius R_r in terms of N, a_s and ℓ_r.
(b) Determine an expression for the peak density in terms of N and R_r.
(c) Find an expression for the ratio R_r/ℓ_r, and comment on its behaviour for large N.
(d) What is the energy of the condensate?

3.3 Derive the expression for the variational energy of a three-dimensional trapped condensate, Eq. (3.35). Repeat in two dimensions (for a potential $V(x, y) = m\omega_r^2(x^2 + y^2)/2$) and in one dimension (for a potential $V(x) = m\omega_r^2 x^2/2$). For each case plot $E/N\hbar\omega_r$ versus the variational width σ, for some different values of the interaction parameter Na_s/ℓ_r. What effect does dimensionality have on the shape of the curves? How do this change the qualitative behaviour described in Sect. 3.5.3?

3.4 Consider a BEC in the non-interacting limit with wavefunction

$$\psi(x, y, z) = \sqrt{n_0}\, e^{-x^2/2\ell_x^2} e^{-y^2/2\ell_y^2} e^{-z^2/2\ell_z^2}, \tag{3.57}$$

where n_0 is the peak density and ℓ_x, ℓ_y and ℓ_z are the harmonic oscillator lengths in three Cartesian directions. The BEC is imaged along the z-direction. Determine the form of the column-integrated density $n_{\mathrm{CI}}(x, y)$. Hint: $\int_0^\infty e^{ax^2} = \frac{1}{2}\sqrt{\pi/a}$.

3.5 Consider a 1D uniform static condensate with $V(x) = 0$. Obtain an expression for the energy E in a length L of the condensate, in terms of n_0, g and L.

Now consider the condensate to be flowing with uniform speed v_0, by constructing a solution according to Eq. (3.43). Show that the solution satisfies the 1D GPE, and confirm that the velocity field of this solution is indeed $v(x) = v_0$. What is the corresponding energy for the flowing condensate, and how does it differ from the static result? Finally, what is its momentum?

3.6 Consider a homogeneous condensate. Identify dimensionless variables so that the dimensionless GPE is,

$$i\frac{\partial\psi'}{\partial t'} = -\nabla'^2\psi' + |\psi'|^2\psi' - \psi', \tag{3.58}$$

i.e., without the 1/2 factor as in Eq. (3.52).

References

1. C.J. Pethick, H. Smith, *Bose-Einstein Condensation in Dilute Gases* (Cambridge University Press, Cambridge, 2008)
2. J.F. Annett, *Superconductivity, Super uids and Condensates* (Oxford University Press, Oxford, 2004)
3. L.P. Pitaevskii, S. Stringari, *Bose-Einstein Condensation (International Series of Monographs on Physics)* (Oxford Science Publications, Oxford, 2003)
4. N.P. Proukakis, B. Jackson, J. Phys. B **41**, 203002 (2008)
5. P.B. Blakie, A.S. Bradley, M.J. Davis, R.J. Ballagh, C.W. Gardiner, Adv. Phys. **57**, 363 (2008)
6. N.P. Proukakis, S.A. Gardiner, M. Davis, M. Szymańska (eds.), *Quantum Gases: Finite Temperature and Non-Equilibrium Dynamics* (Imperial College Press, London, 2013)
7. F. Dalfovo, S. Giorgini, L.P. Pitaevskii, S. Stringari, Rev. Mod. Phys. **71**, 463 (1999)
8. L.D. Carr, C.W. Clark, W.P. Reinhardt, Phys. Rev. A **62**, 063610 (2000)
9. L.D. Carr, C.W. Clark, W.P. Reinhardt, Phys. Rev. A **62**, 063611 (2000)

Chapter 4
Waves and Solitons

Abstract In the previous chapter we considered the shape of steady state condensates, either homogeneous or confined by trapping potentials. We have seen that the condensate described by the GPE is a special kind of fluid, similar to the idealized Euler fluid without viscosity that appears in classical fluid dynamics textbooks. Not surprisingly for a fluid, the dynamics of the condensate exhibit a variety of interesting time-dependent phenomena, from sound waves and shape oscillations, to solitons and vortices.

4.1 Dispersion Relation and Sound Waves

4.1.1 Dispersion Relation

Of particular importance are the behaviour of perturbations to the ground state (either homogeneous or in a trap). This includes *sound waves*, i.e., small-lengthscale density perturbations of the ground state which oscillate periodically, as illustrated in Fig. 4.1. We now derive the behaviour of these perturbations for a homogeneous condensate. The governing equation of motion is the GPE as it appears in either Eq. (3.5) or Eq. (3.46) with $V = 0$. We consider the latter. Assuming one-dimensional motion along the x direction, the GPE is,

$$i\hbar \frac{\partial \psi}{\partial t} = -\frac{\hbar^2}{2m} \frac{\partial^2 \psi}{\partial x^2} + g|\psi|^2 \psi - \mu\psi. \tag{4.1}$$

We know that, for a homogeneous condensate, the steady solution of this equation is the uniform state $\psi_0 = \sqrt{\mu/g}$, with number density $n_0 = |\psi_0|^2 = \mu/g$. We perturb this uniform state by assuming a wavefunction with the form,

$$\psi(x, t) = \psi_0 + \epsilon\psi_1(x, t) + \epsilon^2\psi_2(x, t) + \cdots, \tag{4.2}$$

where $\epsilon \ll 1$ is a small parameter and the functions ψ_1, ψ_2, etc., must be determined. Substituting Eq. (4.2) into Eq. (4.1), noting that temporal and spatial derivatives of
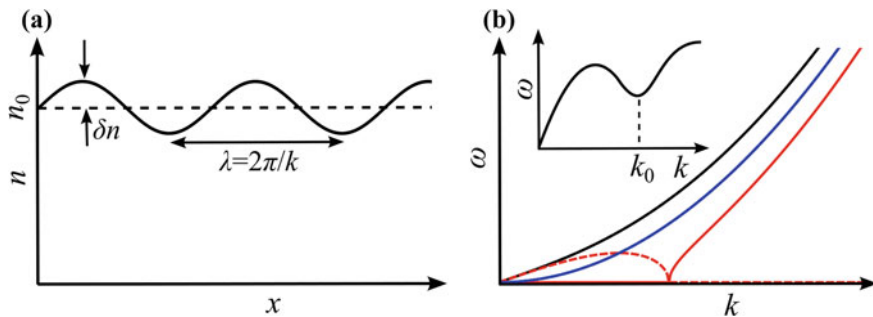
Fig. 4.1 a One dimensional sound waves, that is, sinusoidal perturbations of the background density n_0, of wavelength λ and amplitude $\delta n_0(x, t) \ll n_0$. **b** The dispersion relation $\omega(k)$ of the homogeneous (weakly-interacting) condensate, according to Eq. (4.5), for $g > 0$ (black line), $g = 0$ (*blue line*) and $g < 0$ (*red line*). Solid lines plot the real part of ω and dashed lines plot the imaginary part. For $g < 0$, ω becomes imaginary for small k; everywhere else ω is real. *Inset* In helium II, the dispersion relation has a different and distinct shape, featuring a maxon (local maximum) and roton (local minimum). The roton wavenumber is indicated as k_0

the steady uniform background ψ_0 are zero, and neglecting terms which are quadratic or of higher order in ϵ, we obtain,

$$i\hbar\frac{\partial \psi_1}{\partial t} = -\frac{\hbar^2}{2m}\frac{\partial^2 \psi_1}{\partial x^2} + \mu\psi_1^* + \mu\psi_1. \tag{4.3}$$

This is the *linearized equation of motion for the perturbations*. We look for travelling wave solutions of the general form,

$$\psi_1(x, t) = Ae^{i(kx-\omega t)} + B^*e^{-i(kx-\omega t)}, \tag{4.4}$$

where A and B are complex amplitudes which depend on the initial condition,[1] k is the *wavenumber* and ω the *angular frequency* of the wave. Substituting into Eq. (4.3), we find that non-trivial (non-zero) solutions for A and B exist only if,

$$\omega = \sqrt{\left(\frac{\hbar k^2}{2m}\right)^2 + \frac{n_0 g}{m}k^2}. \tag{4.5}$$

This is called the *dispersion relation*, or sometimes the *Bogoliubov dispersion relation* after Nikolay Bogoliubov who first derived it. It relates the wave's angular frequency ω to its wavenumber k, or equivalently, its period $2\pi/\omega$ to its wavelength $2\pi/k$.

---

[1] We write the amplitude of the second term as B^* rather than B for mathematical convenience.

Notice that the phase velocity of the wave[2] $v_{ph} = \omega/k$ depends, in general, on k. Suppose that the initial condition at $t = 0$ is a generic wave packet, i.e., the superposition of different plane waves with different amplitudes and phases; since these waves move at different phase velocities, the wave-packet spreads out as it propagates, or *disperses*.

Consider the behaviour of the dispersion relation $\omega(k)$ for different regimes of interactions, as plotted in Fig. 4.1b.

- In the **absence of interactions** ($g = 0$) the dispersion relation reduces to $\hbar\omega = \hbar^2 k^2/2m$, in other words the wave behaves like a free particle of momentum $p = \hbar k$ and energy $\hbar\omega$. Note that ω is real; then the exponential terms in the solution of Eq. (4.4) have imaginary exponents and so describe a temporally-oscillating solution.
- For **repulsive interactions** ($g > 0$), this free-particle behaviour ($\omega \sim k^2$) is recovered in the limit of large k/short waves. However, for low k/long waves, the dispersion relation is linear in k. This linear behaviour is characteristic of sound waves—see below. As for $g = 0$, the angular frequencies are real.
- For **attractive interactions**, the situation is fundamentally different. For $g < 0$ and in the regime of sufficiently small k, ω^2 is negative and, correspondingly, ω becomes complex. Then these exponential terms develop *real* and *positive* exponents, such that they exponentially increase in amplitude over time. This signifies the dynamical instability of the homogeneous attractively-interacting condensate—small perturbations are not stable and grow out of control. In fact, this instability is due to the collapse instability we've already described for an attractive condensate; here the condensate prefers to collapse rather than stay as a uniform density profile.

In helium II the shape of the dispersion curve is somewhat different (see Fig. 4.1(inset)), due to the strong inter-atomic interactions in the system. The dispersion relation is linear for small k, but then features a local maximum, termed the *maxon*, and a local minimum, termed the *roton*. At even higher k the dispersion relation flattens off.

4.1.2 Sound Waves

For repulsive interactions ($g > 0$) and in the limit of small k/long waves, the above dispersion relation predicts waves whose angular frequency increases linearly with wavenumber. This is characteristic of sound waves. The phase velocity of these waves is $v_{ph} = \omega/k \approx \sqrt{n_0 g/m}$, which is approximately constant for all wavelengths. This defines the speed of sound,

$$c = \sqrt{\frac{n_0 g}{m}}. \tag{4.6}$$

---

[2]The phase velocity of a wave is the rate at which its phase propagates in space.
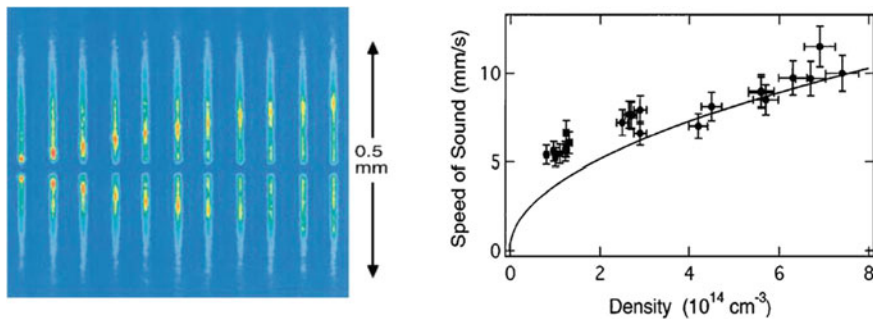
Fig. 4.2 *Left* experimental creation of sound waves after suddenly generating a 'hole' in the centre of the condensate using a laser beam. Shown is the column-integrated density profile of the condensate taken at regular intervals of time. *Yellow*, *red* and *blue* are respectively large, medium and small values of the density. *Right* the measured speed of sound c (points) as a function of the background number density, in agreement with Eq. (4.6) (*solid line*). Reprinted figures with permission from [1]. Copyright 1997 by the American Physical Society

The physical interpretation of these waves is readily obtained using the Madelung transform. By perturbing the state of uniform density $n = n_0 = \mu/g$, we obtain the one-dimensional wave equation,

$$\frac{\partial^2}{\partial t^2}\delta n = c^2 \frac{\partial^2}{\partial x^2}\delta n, \tag{4.7}$$

where $\delta n(x, t) \ll n_0$ are density perturbations about the background condensate (here taken to be the homogeneous condensate), as shown in Fig. 4.1. The wave solution which we have found is one-dimensional—the wave propagates along x— but can be easily generalized to two and three dimensions.

In a trapped condensate ($V \neq 0$) the speed of sound will vary with the position due to the spatial dependence of the density. The speed of sound is less near the edge of the condensate where the density tends to zero.

The prediction of sound waves was tested experimentally in Ref. [1] by using a laser beam to initially and suddenly "punch" a hole in the density at the centre of a condensate, much like a stone being thrown into a pond. This generated low amplitude ripples, i.e., sound waves, which travelled outwards along the condensate, as shown in Fig. 4.2a. The speed of the waves was found to follow the square-root of the density, as seen in Fig. 4.2b and in agreement with the prediction of Eq. (4.6).

4.2 Landau's Criterion and the Breakdown of Superfluidity

Under some perturbation the condensate can become excited. Here we develop a simple yet powerful criterion for excitations to develop, as developed by Landau [18]. Consider a homogeneous ground state condensate, into which an impurity

(e.g. another atom) of mass M enters with initial velocity $\mathbf{v_i}$. Let us imagine that the impurity imparts an excitation of the condensate with energy $\hbar\omega$ and momentum $\hbar\mathbf{k}$; this subsequent velocity of the impurity is $\mathbf{v_f}$. The initial energy (relative to the static background condensate) is just the initial kinetic energy of the impurity, $Mv_i^2/2$, while the final energy after generating the excitation is $Mv_f^2/2 + \hbar\omega$, where $v_i = |\mathbf{v_i}|$ and $v_f = |\mathbf{v_f}|$. Applying conservation of energy gives,

$$\frac{1}{2}Mv_i^2 = \frac{1}{2}Mv_f^2 + \hbar\omega. \tag{4.8}$$

Similarly, applying conservation of momentum before and after the event gives,

$$M\mathbf{v_i} = M\mathbf{v_f} + \hbar\mathbf{k}. \tag{4.9}$$

Inserting Eq. (4.9) into Eq. (4.8) and simplifying gives,

$$\hbar\omega = \frac{1}{2}Mv_i^2 - \frac{1}{2M}\left(M\mathbf{v_i} - \hbar\mathbf{k}\right)^2 = \hbar\mathbf{k}\cdot\mathbf{v_i} - \frac{\hbar^2k^2}{2M}. \tag{4.10}$$

If M is sufficiently large, the second term at the right hand side can be neglected; for excitations to be energetically favoured, the initial velocity v_i then has to satisfy,

$$v_i \geq \left|\frac{\mathbf{k}\cdot\mathbf{v_i}}{k}\right| \geq \frac{\omega}{k}. \tag{4.11}$$

One can instead write this as,

$$v_i \geq v_c, \tag{4.12}$$

where v_c is termed the critical superfluid velocity,

$$v_c = \min\left(\frac{\omega}{k}\right). \tag{4.13}$$

This is a defining property of superfluidity. For $v_i < v_c$ the impurity propagates with no damping, i.e. as a superfluid, while for $v_i \geq v_c$ excitations the motion becomes dissipated by the transfer of energy and momentum to the fluid. This marks the breakdown of superfluidity.

The function $\omega = \omega(k)$ (the dispersion relation) is typically a non-trivial function of k. For a weakly-interacting and homogeneous condensate, with dispersion relation given by Eq. (4.5), this gives,

$$v_c = c. \tag{4.14}$$

For $v < c$ the atom moves with no damping or hindrance, a defining characteristic of superfluidity. For $v > c$ damping can occur through the creation of condensate excitations.
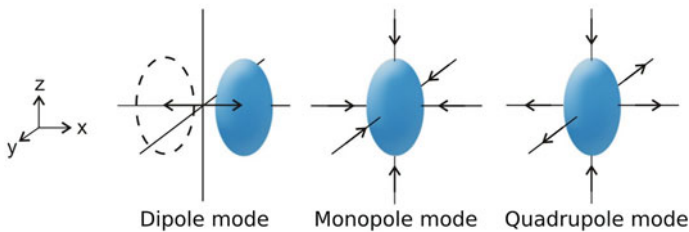
4.3 Collective Modes

In a trapped condensate of finite size, sound waves should have a wavelength considerably smaller than the condensate size (or, equivalently, the angular frequency of the wave should be considerably larger than the trap frequency); this, for example, is clearly satisfied in the experimental images in Fig. 4.2(left). However, if the wavelength of the density perturbations becomes of the order of the condensate size, then these excitations involve a motion of the whole system. These are the *collective modes*.

There is a wide family of collective modes which are supported under harmonic trapping. Here we consider the simplest and most common types, illustrated in Fig. 4.3:

- The **dipole mode** corresponds to an oscillation of the condensate's centre-of-mass about the trap centre. In a harmonic trap, this oscillation occurs at the trap frequency in the respective direction. This mode is not affected by g since, in a harmonic trap, the centre-of-mass motion is decoupled from the internal dynamics. For this reason, this mode is often excited experimentally to measure the trap frequency.
- The **monopole mode** involves contraction-expansion oscillations of the condensate, which are in-phase across the directions.
- The **quadrupole mode** also involves contraction-expansion oscillations, but where the oscillation in one direction is in anti-phase to that in the other directions. Both the quadrupole and monopole modes are sensitive to interactions.

4.3.1 Scaling Solutions

Experimentally, the collective modes are typically induced by forming a stationary condensate, and then suddenly changing the harmonic trap. To induce the dipole mode, the trap can be suddenly translated in space; the condensate finds itself up the trap wall and begins to undergo centre-of-mass oscillations about the trap centre. To induce the monopole, quadrupole or similar modes, the trap frequencies can be

Fig. 4.3 The three common collective modes of a harmonically-trapped condensate

suddenly changed in time. This scenario, in the absence of centre-of-mass motion, is the one we consider here. A similar methodology can be used to account for the centre-of-mass dynamics.

We consider a condensate which is at equilibrium at $t = 0$, with the trap frequencies suddenly changed for $t > 0$. We follow the approach introduced in Ref. [2]. We can model the ensuing oscillations of the condensate through the hydrodynamical description (Sect. 3.3), along with the Thomas–Fermi approximation (Sect. 3.5.2). Recalling the hydrodynamic equations, Eqs. (3.13 and 3.15), dropping terms which depend on the gradients of density, and introducing a general harmonic potential, leads to,

$$\frac{\partial n}{\partial t} + \nabla(n\mathbf{v}) = 0, \qquad (4.15)$$

$$m\frac{\partial \mathbf{v}}{\partial t} + \nabla\left(\frac{1}{2}mv^2 + \frac{1}{2}m(\omega_x^2 x^2 + \omega_y^2 y^2 + \omega_z^2 z^2) + gn\right) = 0. \qquad (4.16)$$

The equilibrium solution of the condensate at $t = 0$ is found by setting $\mathbf{v}$ and the time-derivatives to zero; then the second equation reduces to,

$$\nabla\left(\frac{1}{2}m(\omega_x^2 x^2 + \omega_y^2 y^2 + \omega_z^2 z^2) + gn\right) = 0. \qquad (4.17)$$

Integrating over space and rearranging gives,

$$n = \frac{2\mu - m(\omega_x^2 x^2 + \omega_y^2 y^2 + \omega_z^2 z^2)}{2g}, \text{ for } n \geq 0, \qquad (4.18)$$

where μ arises as the integration constant. This is the equilibrium density profile for the condensate in the Thomas–Fermi limit, as obtained in Sect. 3.5.2. We may also write this in the form,

$$n = n_0\left(1 - \frac{x^2}{R_{x,0}^2} - \frac{y^2}{R_{y,0}^2} - \frac{z^2}{R_{z,0}^2}\right), \text{ for } n(x, y, z) \geq 0, \qquad (4.19)$$

where $R_{j,0} = \sqrt{2\mu/m\omega_j}$, with $j = x, y, z$, are the Thomas–Fermi radii and n_0 is the central density of the condensate at $t = 0$. Applying the usual normalization condition $\int n(x, y, z)\, d^3\mathbf{r} = N$ gives the expression for the central density,

$$n_0 = \frac{15N}{8\pi R_{x,0} R_{y,0} R_{z,0}}. \qquad (4.20)$$

Following a sudden change in the trap frequencies, $\omega_j \to \omega_j(t)$, the condensate profile becomes time-dependent. We consider the time-dependent density to maintain the same general shape throughout but where its dimensions become scaled over

time. This is accounted for by making the radii time-dependent, $R_j \rightarrow R_j(t)$. If we further introduce *scaling parameters* $b_j(t) = R_j(t)/R_{j,0}$ then we can write the time-dependent profile as,

$$n(x, y, z, t) = \frac{n_0}{b_x b_y b_z} \left(1 - \frac{x^2}{b_x^2 R_{x,0}^2} - \frac{y^2}{b_y^2 R_{y,0}^2} - \frac{z^2}{b_z^2 R_{z,0}^2} \right), \qquad (4.21)$$

This is known as the *scaling solution*. The modified pre-factor accounts for the time-dependence of the central density. The initial conditions of the dynamics are,

$$b_j(t = 0) = 1, \quad \dot{b}_j(t = 0) = 0, \qquad (4.22)$$

where the dot represents the time derivative. To satisfy the continuity equation, the velocity field which matches this density must be of the form,

$$\mathbf{v}(\mathbf{r}, t) = \frac{1}{2} \nabla \left[\alpha_x(t)x^2 + \alpha_y(t)y^2 + \alpha_z(t)z^2 \right], \quad \alpha_j = \frac{\dot{b}_j}{b_j}. \qquad (4.23)$$

One proceeds (although the derivation is beyond our scope) to introduce the time-dependent density and velocity distributions into the Thomas–Fermi hydrodynamic equations (4.15) and (4.16). This leads to three coupled equations of motion for the scaling variables $b_j(t)$,

$$\ddot{b}_j + \omega_j(t)^2 b_j - \frac{\omega_{j,0}^2}{b_j b_x b_y b_z} = 0, \qquad (4.24)$$

where $\omega_{j,0}$ is the initial trap frequency in the jth direction. Remarkably, these equations involve the scaling variables b_i and the trap frequencies, only. What is also remarkable is that the same scaling equations of motion arise for a Gaussian ansatz, a justifiable approximation for weak interactions. As such these scaling equations have a much wider coverage than the strongly-interacting Thomas–Fermi limit.

For a cylindrically symmetric trap $V(r, z) = m(\omega_r^2 r^2 + \omega_z^2 z^2)/2$, where $r^2 = x^2 + y^2$, this description reduces to two equations of motion,

$$\ddot{b}_r + \omega_r(t)^2 b_r - \frac{\omega_{r,0}^2}{b_r^3 b_z} = 0, \quad \ddot{b}_z + \omega_z(t)^2 b_z - \frac{\omega_{z,0}^2}{b_r^2 b_z^2} = 0. \qquad (4.25)$$

To demonstrate the collective mode dynamics, we solve these two ordinary differential equations numerically for Thomas–Fermi condensate initially confined to a spherically-symmetric trap with $\omega_r = \omega_z = 2\pi \times 50\,\text{Hz}$. To induce a monopole mode, we reduce the trap frequencies by 10 % for $t > 0$. As seen in Fig. 4.4a, the widths increase initially, and continue to oscillate around a new, larger equilibrium width. Characteristic of a monopole mode, the oscillations are in phase along r and z. Meanwhile, a quadrupole mode is generated by simultaneously increasing ω_z and
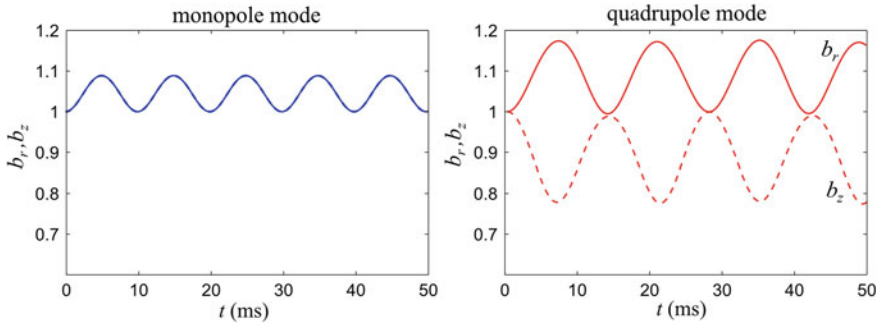
Fig. 4.4 A monopole mode and a quadrupole mode of a condensate in a cylindrically-symmetric harmonic trap. Shown are the radial and axial scaling parameters as a function of time, i.e. $b_r(t)$ and $b_z(t)$, as solved according to the Thomas–Fermi scaling equations of motion, Eq. (4.25). Note that for the monopole mode, the two curves lie on top of each other

decreasing ω_r (both by 10 %). As seen in Fig. 4.4b, the condensate initially expands radially and shrinks axially, and continues to oscillate in anti-phase.

The above scaling equations of motion are valid for arbitrarily large mode amplitudes (providing the Thomas–Fermi approximation is maintained). In the limit of perturbatively small-amplitude modes (e.g. by linearizing about the equilibrium condensate, similar to Sect. 4.1 for a homogeneous system), one can determine the frequency of the collective modes analytically [21]. Under cylindrical symmetry, the mode frequencies obey,

$$\omega_{M,Q}^2 = \omega_r^2 \left(2 + \frac{3}{2}\lambda^2 \pm \frac{1}{2}\sqrt{16 - 16\lambda^2 + 9\lambda^4} \right), \qquad (4.26)$$

where the "+" refers to the monopole mode frequency, ω_M, and the "−" to the quadrupole mode frequency, ω_Q, and $\lambda = \omega_z/\omega_r$ is the *trap ratio*. For an approximately spherical trap ($\lambda \approx 1$) this gives,

$$\omega_M \approx \sqrt{5}\omega_r, \quad \omega_Q \approx \sqrt{2}\omega_r. \qquad (4.27)$$

These are in close agreement with the frequencies of the oscillations in Fig. 4.4.

These scaling predictions give excellent agreement with the mode dynamics observed in experiments. These modes play an important role in this field. They are straightforward to generate experimentally and can be measured to high accuracy, and provide a versatile means to test theoretical models and assumptions. According to these predictions, the modes persist forever since the condensate has no viscosity. In reality, thermal dissipation causes the modes to decay over time, although usually on a much longer timescale than the oscillations themselves.

4.3.2   Expansion of the Condensate

A particular case of these scaling dynamics is when the trap is suddenly switched off and the condensate is allowed to expand freely. This is routinely performed in BEC experiments since some expansion of the gas is often necessary to enable imaging of small features such as dark solitons and vortices.

For $\omega_r(t) = \omega_z(t) = 0$ the cylindrically-symmetric scaling equations (4.25) reduce to,

$$\ddot{b}_r = \frac{\omega_{r,0}^2}{b_r^3 b_z}, \quad \ddot{b}_z = \frac{\omega_{z,0}^2}{b_r^2 b_z^2}. \tag{4.28}$$

Replacing the time variable with $\tau = \omega_z t$ and introducing the initial trap ratio, $\lambda = \omega_{z,0}/\omega_{r,0}$, gives,

$$\frac{d^2 b_r}{d\tau^2} = \frac{1}{b_r^3 b_z}, \quad \frac{d^2 b_z}{d\tau^2} = \frac{\lambda^2}{b_r^2 b_z^2}. \tag{4.29}$$

It is possible to obtain analytic expressions for $b_r(t)$ and $b_z(t)$ for the case of a cigar-shaped condensate, $\lambda \ll 1$ [2]. We proceed by expanding the solutions in powers of λ^2, i.e.,

$$b_r(\tau) = 1 + \alpha_r(\tau)\lambda^2 + \beta_r(t)\lambda^4 + \cdots, \quad b_z(\tau) = 1 + \alpha_z(\tau)\lambda^2 + \beta_z(\tau)\lambda^4 + \cdots$$

To lowest order in λ, the axial dynamics satisfy,

$$\frac{d^2 b_z}{d\tau^2} = 0, \quad b_z(\tau) = 1. \tag{4.30}$$

In obtaining this solution for b_z we have applied the initial conditions in Eq. (4.22). Employing this result, we find the radial dynamics satisfy,

$$\frac{d^2 b_r}{d\tau^2} = \frac{1}{b_r^3}, \quad b_r(t) = \sqrt{1 + \tau^2}. \tag{4.31}$$

Continuing to second order, we find that the axial expansion satisfies,

$$b_z(\tau) = 1 + \lambda^2 [\tau \arctan \tau - \ln \sqrt{1 + \tau^2}] + \mathcal{O}(\lambda^4). \tag{4.32}$$

The expansion develops very differently in the two directions. The radial size increases rapidly at first, whereas the axial spreading is weak, suppressed by the λ^2 factor. We define the aspect ratio of the condensate as $R_r/R_z = R_{r,0} b_r / R_{z,0} b_z$. Initially, $R_r/R_z = \omega_z/\omega_r = \lambda$. Over time the aspect ratio is modified by the scaling dynamics as $\lambda b_r / b_z$. Using the above analytic expressions, it can be shown that in the limit of large τ, the aspect ratio approaches the value,
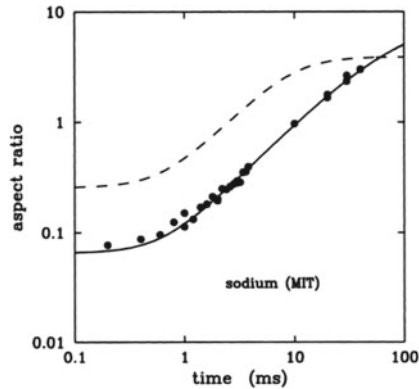
Fig. 4.5 The evolution of the aspect ratio R_r/R_z during expansion of a cylindrically-symmetric condensate, from the experiment of Ref. [3]. The circles are the experimental data points. The condensate evolves from its initial cigar shape ($R_r/R_z < 1$) to a pancake shape ($R_r/R_z > 1$). The numerical solution of the scaling Eq. (4.25) and the analytic predictions for $\lambda \ll 1$ are indistinguishable (appearing as the solid black line). The dot-dashed line is the corresponding prediction for non-interacting atoms. The figure is reproduced from Ref. [20] with permission of the Societa Italiana di Fisica

$$\left(\frac{R_r}{R_z}\right)_{\tau \to \infty} = \frac{2}{\pi \lambda}. \tag{4.33}$$

In other words the condensate reverses its aspect ratio. These predictions agree accurately with experimental observations of condensate expansion, as seen in Fig. 4.5.

4.4 Solitons

In one-dimension and in the absence of an external potential, the GPE is,

$$i\hbar \frac{\partial \psi}{\partial t} = -\frac{\hbar^2}{2m} \frac{\partial^2 \psi}{\partial x^2} + g|\psi|^2 \psi, \tag{4.34}$$

where the variables and parameters take their 1D definitions. This is a form of the 1D *nonlinear Schrödinger equation*. This equation is well-studied in the context of nonlinear optics. It has the special property of being *integrable* such that its solutions possess an infinite set of conserved quantities (integrals of motion). The simplest of these quantities (and those with a clear physical interpretation for our system) are the norm N, the momentum $\mathcal{P}$ and the energy E,

$$N = \int\limits_{-\infty}^{+\infty} |\psi|^2 \mathrm{d}x, \tag{4.35}$$

$$P = \frac{i\hbar}{2} \int\limits_{-\infty}^{+\infty} \left(\psi \frac{\partial \psi^*}{\partial x} - \psi^* \frac{\partial \psi}{\partial x} \right) \mathrm{d}x, \tag{4.36}$$

$$E = \int\limits_{-\infty}^{+\infty} \left(\frac{\hbar^2}{2m} \left| \frac{\partial \psi}{\partial x} \right|^2 + \frac{g}{2} |\psi|^4 \right) \mathrm{d}x. \tag{4.37}$$

It is due to these special properties that Eq. (4.34) supports solutions known as *solitons*. Solitons are nonlinear waves which arise in many areas of physics, from fluids to optics to plasmas [4]. Solitons have three characteristic properties [6]:

- They have a permanent, unchanging form.
- They are localized in space.
- They emerge unscathed from collisions with other solitons.

Their permanent form is due to dispersion being perfectly balanced by their non-linearity; as a consequence, solitons propagate without spreading out in space. This makes them analogous to particles, and motivated their particle-like name "solitons".

The soliton solutions of the nonlinear Schrödinger equation were obtained in the pioneering works of Zakharov and Shabat, using a technique called the *inverse scattering transform* (see Ref. [5] for more information). Depending on the sign of the interaction parameter g, *dark solitons* and *bright solitons* are supported, as we see next. Dark and bright solitons were first studied in the context of nonlinear optics; there they correspond to a dip and a peak in an optical intensity field, respectively, giving rise to their names.

Condensates are, in reality, three-dimensional and feature trapping potentials, and so "solitons" therein are not strictly solitons. However, they show the key solitonic properties, and so we continue to use the term "soliton". In other literature, they are often referred to as "solitary waves".

4.5 Dark Solitons

4.5.1 *Dark Soliton Solutions*

Dark solitons are supported for repulsive interactions ($g > 0$). These waves consist of a localized density dip with a phase jump across it, and propagate along at speed u. The speed can exist in the range $0 < u \leq c$, where c is the speed of sound. A broad review of dark solitons in condensates is given in Ref. [7].
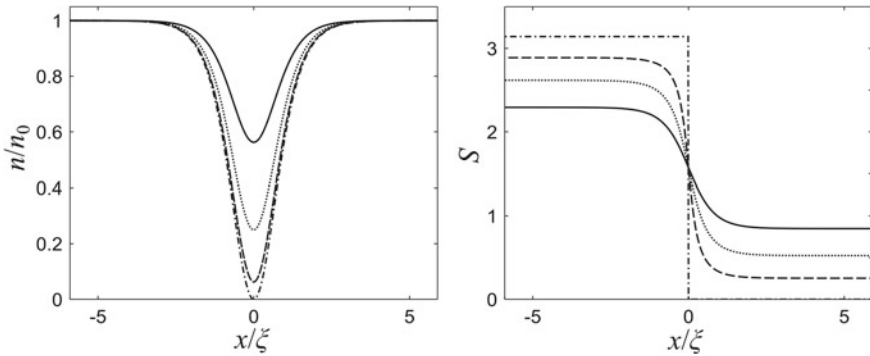
Fig. 4.6 Density $n(x)$ and phase $S(x)$ profiles of dark solitons with various speeds: $u/c = 0$ (*dot-dashed line*), $u/c = 0.25$ (*dashed line*), $u/c = 0.5$ (*dotted line*) and $u/c = 0.75$ (*solid line*). Density is scaled in terms of the background density of the homogeneous system, n_0, and position in terms of the healing length, ξ

The general dark soliton solution to Eq. (4.34) with $g > 0$ is,

$$\psi(x, t) = \sqrt{n_0} \left\{ B \tanh\left[\frac{B(x - ut)}{\xi} \right] + i\frac{u}{c} \right\} \exp\left(-\frac{i\mu t}{\hbar} \right), \qquad (4.38)$$

where $B = \sqrt{1 - u^2/c^2}$. The density and phase profiles of some dark solitons are shown in Fig. 4.6. The density depression and the phase profile vary with speed. Note that the soliton width is always of the order of the healing length ξ.

A dark soliton state is an excited state; the ground state is the soliton-free homogeneous density. In the lab frame (the frame at rest with the background condensate), the soliton is a moving solution. However, dark solitons become stationary solutions in the moving frame, e.g. the $u/c = 0.5$ soliton is a stationary (excited) state in the frame moving at the same speed.

If $u = 0$ then one obtains the stationary *black soliton*, whose density profile is,

$$n(x) = n_0 \tanh^2(x/\xi). \qquad (4.39)$$

The density of the black soliton goes to zero at its centre, and the phase jump is a sharp step of π. At the opposite speed extreme, the $u = c$ dark soliton has zero density depth and no phase slip, i.e. it is indistinguishable from the background. For more general speeds, the *soliton depth*, that is, the maximum depth of the soliton density depression, follows from Eq. (4.38) as,

$$n_{\rm d} = n_0(1 - u^2/c^2). \qquad (4.40)$$

The phase slip profile across the soliton also varies with speed. We define the total phase slip ΔS as the difference between the phases at $\pm\infty$, i.e. $\Delta S = S(x = -\infty) - $
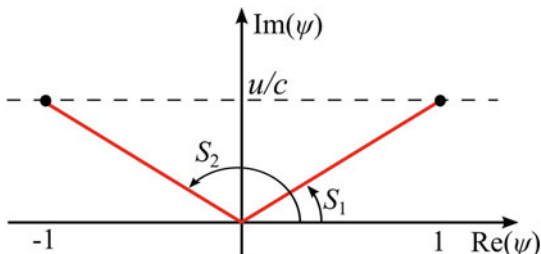
$S(x = \infty)$. The dark soliton solution becomes $\psi \to \sqrt{n_0}(1 + iu/c)$ for $x \to \infty$, and $\psi \to \sqrt{n_0}(-1 + iu/c)$ for $x \to -\infty$. Therefore, as we move from $x = \infty$, through the origin, to $x = -\infty$, the phase of ψ (that is, the angle S between $\text{Re}(\psi)$ and $\text{Im}(\psi)$) changes from $S = S_1$ at the point $(1, u/c)$ on the complex plane ψ, to $S = \pi/2$ at $(0, u/c)$, to $S = \pi - S_1$ at $(-1, u/c)$. Hence the change of the phase from $x = \infty$ to $x = -\infty$ is $\Delta S = 2 \arccos(u/c)$. Taking the limit $u/c \to 0$, we conclude that the phase jump is $\Delta S = \pi$, as we have said. A dark soliton is therefore a 1D *phase defect*: a discontinuity of the quantum mechanical phase (Fig. 4.7).

4.5.2 Particle-Like Behaviour

The energy and momentum of a dark soliton are $E_s = \frac{4}{3}n_0 \hbar c B^3$ and $\mathcal{P}_s = -2\hbar n_0 u B/c + 2\hbar n_0 \arctan(Bc/u)$, as obtained in Problem 4.1. Here we show that the dark soliton behaves like a classical particle. Differentiating its energy E_s and momentum $\mathcal{P}_s$ with respect to speed u gives,

$$\frac{dE_s}{du} = -\frac{4n_0 \hbar u B}{c}, \quad \frac{dP_s}{du} = -\frac{4n_0 \hbar B}{c}. \tag{4.41}$$

Note that the energy and momentum both *decrease* as the soliton gets faster! Using these results and the chain rule we can then form,

$$\frac{dE_s}{d\mathcal{P}_s} = \frac{dE_s}{du}\frac{du}{d\mathcal{P}_s} = u. \tag{4.42}$$

This result informs us that the dark soliton behaves like a classical particle. Its effective mass is defined as $m_s = \dfrac{d\mathcal{P}_s}{du}$, which we know from Eq. (4.41) is,

$$m_s = -\frac{4n_0 \hbar B}{c}. \tag{4.43}$$

The dark soliton behaves as a classical particle with *negative mass*. This is not surprising given that the dark soliton is an *absence of atoms*. We can also estimate the ratio of the soliton mass to the atomic mass,

$$\frac{|m_s|}{m} \sim \frac{4\hbar n_0}{mc} \sim 4\xi n_0. \tag{4.44}$$

ξn_0 is the number of atoms within a ξ-sized length of the system and typically $\xi n_0 \gg 1$ such that the soliton is considerably more massive than an atom.

In the limit of slow solitons ($B \approx 1$) the energetics of the soliton reduces to a particularly simple form. Taking the Taylor expansion of the soliton energy, Eq. (4.37), about $v = 0$ and up to terms in v^2 gives,

$$E(v) = E(0) + \frac{dE}{du}\Big|_0 u + \frac{1}{2}\frac{d^2 E}{du^2}\Big|_0 u^2 + \mathcal{O}(v^3) \tag{4.45}$$

$$= \frac{4}{3}n_0\hbar c - \frac{2n_0\hbar u^2}{c}. \tag{4.46}$$

Introducing the soliton mass in this limit, $m_s = -4n_0\hbar/c$, we obtain,

$$E(v) = E_0 + \frac{1}{2}m_s u^2, \tag{4.47}$$

which is the form for a classical particle moving in free space with *rest mass* E_0 and kinetic energy $m_s u^2/2$. This relation shows that, due to the negative effective mass, slower solitons have greater energy. Conversely, if the soliton loses energy (due to some dissipative processes) it will speed up!

4.5.3   Collisions

Solutions of Eq. (4.34) for arbitrary numbers of solitons can be obtained analytically using the inverse scattering transform [5], and the two soliton solution of the GPE can be found in Ref. [7]. The collisions of two dark solitons, with equal speeds, are shown in Fig. 4.8 over different incident speeds. Notice how the solitons emerge from the collision with unchanged form and speed, one of the fundamental properties of solitons. For low incoming speed ($u/c < 0.5$), the solitons appear to bounce, while for higher speeds ($u/c \geq 0.5$) they appear to pass through each other. The only overall effect of the collision on the outgoing solitons is a shift in their position, relative to how they would have moved in the absence of another soliton; this is known as the *phase shift* during the collision
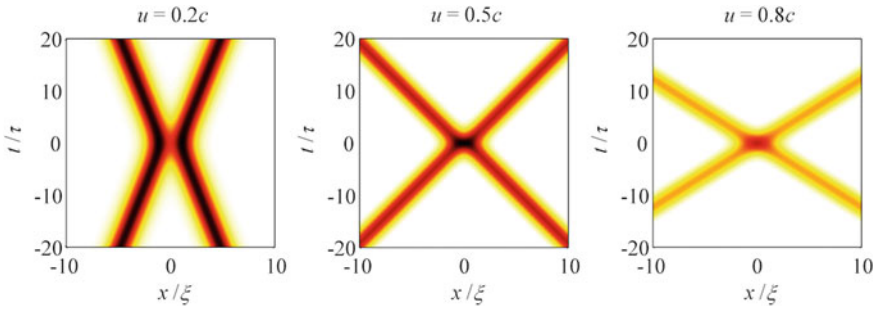
Fig. 4.8 Collisions of two dark solitons at different incoming speeds. *White* represents the background density n_0 and *darker shades* represents lower densities. Note that the time axis is centred on the soliton collision

4.5.4 Motion in a Harmonic Trap

The special integrable properties that give rise to the soliton solution of Eq. (4.38) hold only if the trapping potential $V(x)$ is zero or uniform in space. So what happens if a non-uniform potential, typical of real condensates, is applied to the system? The dark soliton then moves through a continuously changing background density; the soliton, in turn, must adjust to its new surroundings, and in doing so it emits energy in the form of sound waves. Remarkably, harmonic traps are special in that this decay is prohibited (in fact, the harmonic trap focuses the emitted sound energy back into the soliton). This stabilizes the soliton, and we find that the trapped soliton retains much of the key soliton properties, albeit with modified dynamics due to the trapping potential.

Figure 4.9 shows a simulation of the 1D GPE for a dark soliton in a condensate under a harmonic trap $V(x) = m\omega_x^2 x^2/2$. The dark soliton is started off away from
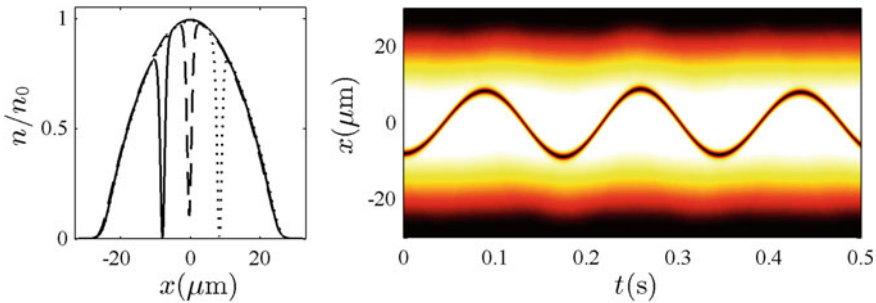
Fig. 4.9 A dark soliton oscillating in a harmonically-trapped condensate, simulated by the 1D GPE. The trap is $V(x) = m\omega_x^2 x^2/2$, with trap frequency $\omega_x = 2\pi \times 8$Hz. *left* shows the density profile at three times, while *right* shows a space-time plot of the condensate density (the dark soliton appearing as the oscillating dark line)

the trap origin as a black ($v = 0$) soliton. The soliton accelerates towards the trap centre and over-shoots, climbs up the far trap wall and decelerates until it becomes stationary. This motion repeats, such that the soliton oscillates sinusoidally in the trap. The motion is akin to a classic harmonic oscillator. The oscillations continue with uniform amplitude due to the absence of any dissipation in the system. The soliton oscillation induces a weak "wobbling" of the condensate. Note that if the soliton is black and at the trap centre, then it is stationary. Indeed, this state is the first excited state of the trapped condensate. If there were some dissipation acting on the soliton to reduce its energy, its oscillation amplitude will *grow* due to its negative effective mass (in contrast to a conventional damped oscillator). This effect is termed *anti-damping*.

One might expect the soliton to oscillate at the frequency of the trap. For the simulation in Fig. 4.9 the trap frequency is $\omega_x = 2\pi \times 8\,\text{Hz}$, whereas the soliton has a frequency $\omega_s = 2\pi/T_s \approx 2\pi \times 5.5\,\text{Hz}$, where $T_s \approx 0.18\,\text{s}$ is the observed soliton period. We can interpret this difference as follows. Assuming that the background density is slowly-varying in space, we can define the soliton energy as per the homogeneous system (see top of Sect. 4.5.2) but where the uniform density is replaced by its local value, $n(x)$. We then obtain,

$$E_s(u, x) = \frac{4}{3} \frac{\hbar}{\sqrt{mg}} \left(n(x)g - mu^2\right)^3. \tag{4.48}$$

Again, we take the condensate profile to follow the Thomas–Fermi form, $n(x)g = \mu - V(x) = \mu - m\omega^2 x^2/2$. Inserting into the above equation gives,

$$E_s(u, x) = \frac{4}{3} \frac{\hbar}{\sqrt{mg}} \left(\mu - \frac{1}{2}m\omega_x^2 x^2 - mu^2\right)^3. \tag{4.49}$$

We proceed to expand this expression for slow solitons ($u/c \ll 1$) and close to the origin, via a two-dimensional Taylor series,

$$E_s(u, x) = E(0, 0) + x\frac{\partial E}{\partial x}\bigg|_{(0,0)} + u\frac{\partial E}{\partial u}\bigg|_{(0,0)}$$
$$+ \frac{1}{2}\left[u^2\frac{\partial^2 E}{\partial u^2}\bigg|_{(0,0)} + 2ux\frac{\partial^2 E}{\partial x \partial z}\bigg|_{(0,0)} + x^2\frac{\partial^2 E}{\partial x^2}\bigg|_{(0,0)}\right] + \mathcal{O}(x^3, u^3).$$

This leads to the result,

$$E_s(u, x) = E_0 + \frac{1}{2}m_s u^2 + \frac{1}{4}m_s\omega_x^2 x^2, \tag{4.50}$$

where $m_s = -4\hbar n_0 c$ is the low-speed soliton effective mass and $E_0 = 4\hbar\mu^{3/2}/4\sqrt{mg}$ is the rest mass (as used for Eq. (4.46)). For a mass m obeying the classic har-

monic oscillator $\ddot{x} + \omega_x^2 x = 0$, the corresponding expression is $E = E_0 + mu^2/2 + m\omega_x^2 x^2/2$. By comparison we see that the soliton behaves like an oscillator with effective frequency,

$$\omega_s = \frac{\omega_x}{\sqrt{2}}. \tag{4.51}$$

This result was first predicted in Ref. [8]. For the example in Fig. 4.9, this predicts $\omega_s = 2\pi \times 5.66\,\text{Hz}$ and $T_s = 0.177\,\text{s}$, which is in excellent agreement with the simulations. It has also been found to agree well with experimental observations.

4.5.5 Experiments and 3D Effects

Dark solitons were first created in condensates in experiments [9, 10], although they were short-lived. A more recent experiment, working in a highly-elongated, effectively one-dimensional geometry and at very cold temperature, generated dark solitons which persisted for several seconds, equivalent to tens of oscillations in the trap [11]. The dynamics were in good agreement with the predictions of the 1D GPE. The eventual disappearance of the soliton was attributed to thermal dissipation acting on the soliton; this causes the soliton to lose energy and anti-damp, eventually becoming indistinguishable from the rest of the condensate.

The typical approach to generate a dark soliton, as used in the above experiments, is to first form a condensate in the trap, and then briefly illuminated a portion using masked laser light. Due to the atom-light interaction, the illuminated part of the condensate develops a different phase to the un-illuminated part, such that an effective 1D step in the phase is created. This then evolves into one or more dark solitons. In 3D, these solitons appears as stripes of low density, aligned perpendicular to their axis of propagation, and a phase step along this axis, as illustrated in Fig. 4.10 (left).
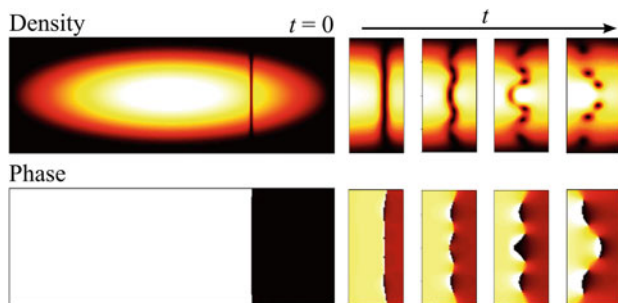
Fig. 4.10 Two-dimensional density and phase images through a 3D condensate, which has a 3D dark soliton positioned initially to one side (*left*). The initial phase appears as a step profile. If the condensate is too wide, the soliton undergoes the snake instability (*right*), leading to its decay into vortex rings (which appear as vortex-antivortex pairs in this 2D image)

If the condensate is too wide, the 3D dark soliton is not dimensionally stable. The soliton stripe becomes unstable to transverse perturbations, causing a bending of the soliton stripe, known as the *snake instability*. The soliton stripe gets torn apart into vortex rings, which are stable excitations in 3D condensates. This decay is illustrated in Fig. 4.10 (right). To prevent the snake instability, the condensate should be quasi-one-dimensional (with a transverse size of the order or less than the healing length ξ—see Sect. 3.5.4). At the crossover between 1D and 3D, it is possible to form *solitonic vortices*, which have combined properties of dark solitons and vortices [12, 19].

4.6   Bright Solitons

For attractive interactions ($g < 0$) the 1D GPE (4.34) supports *bright solitons*. In contrast to dark solitons, these are self-trapped condensates in which the attractive interactions overcome wavepacket dispersion. We saw in Sect. 4.1.1 that the homogeneous condensate in 1D with attractive interactions is unstable. Actually the stable ground state is a bright soliton. A detailed review of bright solitons in condensates can be found in Ref. [13].

The general solution for a single bright soliton, containing N atoms and moving at speed u, is,

$$\psi(x, t) = \sqrt{\frac{N}{2\xi_s}} \operatorname{sech}\left(\frac{x - ut}{\xi_s}\right) \exp\left[if(x, t) + i\phi\right], \tag{4.52}$$

where $\xi_s = 2\hbar^2/m|g|N$ characterises the soliton width, ϕ is a global phase offset, and

$$f(x, t) = \frac{mux}{\hbar} - \frac{t}{\hbar}\left(\frac{mu^2}{2} - \frac{\hbar^2}{2m\xi_s^2}\right), \tag{4.53}$$

is a time- and space-dependent phase factor. The soliton maintains a sech-squared density profile, shown in Fig. 4.11a, as it propagates. For stronger attractive interactions and/or more atoms, the soliton is narrower, indicative of a stronger binding effect. For a dark soliton, the density profile of the soliton is related to its speed; for bright solitons, the density profile and speed are decoupled, and a bright soliton can take on any speed u.

To understand the manner is which the soliton is supported, we take a variational approach. As an ansatz for the soliton solution, we adopt a Gaussian wavepacket of width ℓ, normalised to N atoms, i.e.,

$$\psi(x) = \frac{N^{1/2}}{\pi^{1/4}\ell^{1/2}} \exp\left(-\frac{x^2}{2\ell^2}\right). \tag{4.54}$$
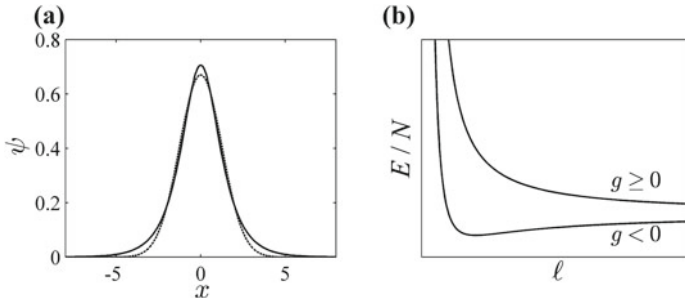
Fig. 4.11 **a** Density profile $n(x) = |\psi|^2$ of the bright soliton solution of Eq. (4.52), taking $u = 0$ (*solid line*). The variational solution of the Gaussian ansatz (4.54) is in good agreement (*dashed line*). **b** The energy-per-particle E/N of the Gaussian ansatz, given by Eq. (4.55), versus the width of the ansatz, ℓ, for two regimes of interactions

Using Eq. (3.6), the energy-per-particle E/N of this wavepacket is,

$$\frac{E(\ell)}{N} = \frac{\hbar^2}{4m\ell^2} + \frac{gN}{2\sqrt{2\pi}\ell}. \tag{4.55}$$

Consider the form of E/N for two regimes of interactions (illustrated in Fig. 4.11a):

- For $g \geq 0$, E/N decreases monotonically with ℓ. All states are prone to expanding and there is no stationary state. For $g = 0$ the expansion is driven by dispersion, while for $g > 0$ the repulsive interactions also contribute to the expansion.[3]
- For $g < 0$ there exists a local minimum in $E(\ell)/N$, implying that a stable stationary state exists. This is due to a delicate balance between the dispersive term, which scales like $1/\ell^2$ and dominates for small ℓ, and the attractive nonlinear term, which scales like $-1/\ell$ and dominates elsewhere.

For $g < 0$ the variational width is found by locating the position of the energy minimum. Differentiating E/N with respect to ℓ, setting to zero and rearranging gives the width of the variational solution, $\ell_v = \frac{\sqrt{2\pi}\hbar^2}{m|g|N}$, which agrees well with the true solution—see Fig. 4.11a.

4.6.1 Collisions

Being a self-contained condensate, a bright soliton has a global phase, ϕ, and this significantly affects the manner in which bright solitons interact. Dark solitons, in contrast, have no such phase freedom.

---

[3]If a harmonic potential is included, then a positive x^2 term is added to $E(\ell)/N$ which then does support an energy minimum, representing the ground trapped condensate.

To get some insight, consider two bright solitons, each with N atoms. Soliton 1 begins at position $-x_0$ (with $x_0 > 0$) and propagates to the right with speed u, while soliton 2 begins at position x_0 and propagates to the left with the same speed. Their individual solutions are,

$$\psi_1(x, t) = \sqrt{\frac{N}{2\xi_s}} \text{sech}\left(\frac{x + x_0 - ut}{\xi_s}\right) e^{if(x,t)} e^{i\phi_1}, \tag{4.56}$$

$$\psi_2(x, t) = \sqrt{\frac{N}{2\xi_s}} \text{sech}\left(\frac{x - x_0 + ut}{\xi_s}\right) e^{if(x,t)} e^{i\phi_2}. \tag{4.57}$$

Note that due to the symmetric configuration, both solitons have the same time- and space-dependent phase factor $e^{if(x,t)}$, but we allow for different global phase offsets, ϕ_1 and ϕ_2.

Assuming that the solitons are well-separated we can construct their superposition as $\psi' = \psi_1 + \psi_2$.[4] We proceed to calculate the density profile of this superposed state, $|\psi'| = |\psi_1 + \psi_2|^2$,

$$|\psi'(x, t)|^2 = \left||\psi_1| e^{if(x,t)} e^{i\phi_1} + |\psi_2| e^{if(x,t)} e^{i\phi_2}\right|^2 \tag{4.58}$$

$$= |\psi_1|^2 + |\psi_2| + |\psi_1||\psi_2| \left(e^{i\Delta\phi} + e^{-i\Delta\phi}\right), \tag{4.59}$$

where we have introduced the *relative phase* $\Delta\phi = \phi_2 - \phi_1$. Using the identity $\cos\theta = (e^{i\theta} + e^{-i\theta})/2$ we obtain,

$$|\psi'(x, t)|^2 = |\psi_1|^2 + |\psi_2| + 2|\psi_1||\psi_2| \cos\Delta\phi. \tag{4.60}$$

Let us see how this affects the overlap of the two solitons by calculating the density at their midpoint (the origin). Introducing the form of ψ_1 and ψ_2 from Eq. (4.57) and setting $x = 0$ gives,

$$|\psi'(0, t)|^2 = \frac{N}{2\xi_s} \left[2\text{sech}^2\left(\frac{x_0 - ut}{\xi_s}\right) + 2\cos\Delta\phi \, \text{sech}^2\left(\frac{x_0 - ut}{\xi_s}\right)\right]. \tag{4.61}$$

If $\Delta\phi = 0$ then the density at the midpoint reinforces (constructive interference), in other words, the solitons overlap with each other. However, for $\Delta\phi = \pi$ the midpoint density is forced to zero (destructive interference), and the overlap of the solitons is prohibited. For intermediate values of the relative phase, the overlap varies smoothly between these extremes.

Figure 4.12 shows the collisions for different relative phases. True to their solitonic character, the solitons emerge unscathed from the collision, barring a shift. The role of relative phase becomes clear: for $\Delta\phi = 0$ the solitons merge at the point

---

[4] The superposition theorem does not apply to the GPE since it is a nonlinear equation; constructing a superposition is only a valid approximation if the density is low. This condition is satisfied here since we are concerned with the weak overlap between well-separated solitons.
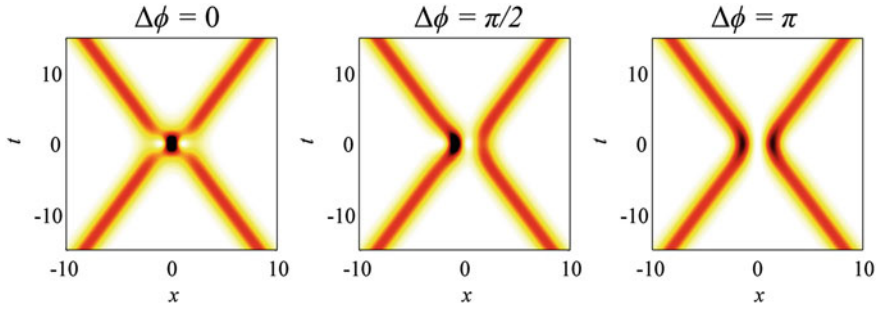
Fig. 4.12 Density profile $n(x, t) = |\psi(x, t)|^2$ during the collision of two bright solitons, with speed $u = 0.2$ and for different relative phases

of collision, while for $\Delta\phi = \pi$ overlap is prohibited and they appear to bounce. In between the collision becomes asymmetric. Despite these different behaviours during the collision, it is remarkable that the outgoing solitons are independent of $\Delta\phi$.

4.6.2 Experiments and 3D Effects

The addition of a harmonic potential to the 1D GPE (4.34) breaks the integrability of the system, and true soliton solutions no longer exist. The state adopts behaviours of a trapped condensate, such as collective modes. The ground state becomes narrower and more peaked than the soliton solution, and in the limit of a very strong trap, the ground state tends towards the Gaussian ground harmonic oscillator state. As such the width of the wavepacket varies between the two limiting cases, ξ_s and l_x, respectively. However, the solutions continue to show soliton-like behaviour: an initially off-centre soliton will oscillate in the trap (the dipole mode) with unchanged form, and two solitons will collide repeatedly and emerge unscathed.

In reality, bright solitons are 3D objects, and this introduces the collapse instability discussed in Sect. 3.5.3. This physical effect is not modelled within the 1D GPE. This difference can be understood as follows. For a generalized static attractively-interacting condensate of characteristic size ℓ in $\mathcal{D}$ dimensions, its kinetic energy (due to zero-point motion) scales as $\mathcal{D}/\ell^2$ and its interaction energy scales as $-1/\ell^{\mathcal{D}}$. For $\mathcal{D} = 1$ we recover the behaviour discussed above—the kinetic energy term always wins in the $\ell \to 0$ limit, negating a collapse instability. For $\mathcal{D} = 3$, however, the negative interaction term always dominates in this limit, such that the packet can lower its energy by shrinking, i.e. a collapse instability. $\mathcal{D} = 2$ is a borderline case where stability to collapse depends on the system parameters.
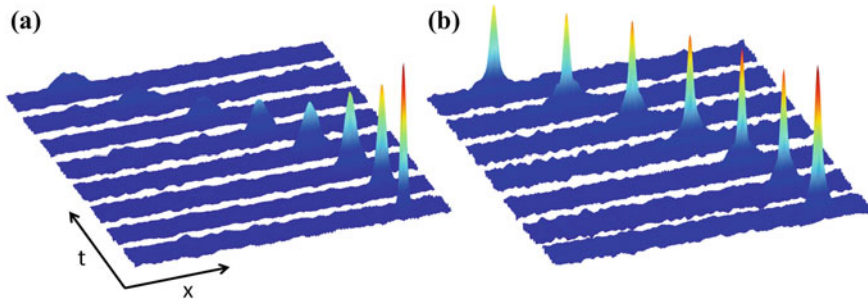
Fig. 4.13 a As a repulsive BEC travels along a waveguide (with tight transverse harmonic trapping and very weak axial confinement) it spreads out. **b** For attractive interactions, the condensate is seen to maintain its shape over time, characteristic of a bright soliton. Image courtesy of S. L. Cornish (University of Durham)

A 3D bright soliton can be formed within a *waveguide potential*, $V(r, z) = m\omega_r^2 r^2/2$, which has tight harmonic confinement in the transverse directions but is untrapped along z. Then a 3D bright soliton can form, which is self-trapped along z. This state is stable to collapse up to a critical interaction strength $N|a_s|/l_r \approx 0.7$.

Bright solitons were first formed with condensates in 2002 [14, 15]. They are typically generated as follows. A stable repulsive condensate is first formed in a highly-elongated harmonic trap. The interaction strength is then tuned to being attractive by means of a magnetic Feshbach resonance. In these early experiments, the critical number of atoms was exceeded, driving a collapse. Out of the collapse one or more bright solitons formed. More recent experiments form bright solitons by choosing parameters which avoid the collapse instability. The weak axial trap is either kept on, in which case the soliton/s oscillate axially, or is switched off, such that the solitons propagate freely. An experimental proof of bright solitons is shown in Fig. 4.13. For repulsive interactions it was seen that the condensate expanded over time, while for attractive interactions it was seen to maintain its shape, characteristic of a soliton. More recent experiments have studied the collisions of bright solitons with each other [16] and with potential barriers [17].

Problems

4.1 For a dark soliton, the integrals of motion in Eqs. (4.35)–(4.37) are renormalized so as to remove the contribution from the background and lead to finite values,

$$N_\text{s} = \int\limits_{-\infty}^{+\infty} (n_0 - |\psi|^2)\, \mathrm{d}x$$

$$\mathcal{P}_\text{s} = \frac{i\hbar}{2} \int\limits_{-\infty}^{+\infty} \left(\psi \frac{\partial \psi^*}{\partial x} - \psi^* \frac{\partial \psi}{\partial x} \right) \left(1 - \frac{n_0}{|\psi|^2} \right) \mathrm{d}x$$

$$E_\text{s} = \int\limits_{-\infty}^{+\infty} \left(\frac{\hbar^2}{2m} \left| \frac{\partial \psi}{\partial x} \right|^2 + \frac{g}{2}(|\psi|^2 - n_0)^2 \right) \mathrm{d}x$$

Evaluate these integrals using the dark soliton solution Eq. (4.38), leaving your answers in terms of ξ, n_0, u and c.

4.2 Consider a dark soliton in a harmonically-trapped condensate. Approximating the background condensate with the Thomas–Fermi profile $n(x) = n_0(1 - x^2/R_x^2)$ (for $x \leq R_x$, otherwise $n = 0$) and treating the soliton depth n_d to be constant, obtain an expression for the soliton speed as a function of its position x and depth n_d. Hence obtain an expression for the turning points of its motion.

4.3 Show that the static ($u = 0$) bright soliton solution, obtained from Eq. (4.52), is a solution to the 1D attractive time-independent GPE with $V(x) = 0$, i.e.,

$$\mu\psi = -\frac{\hbar^2}{2m} \frac{\mathrm{d}^2\psi}{\mathrm{d}x^2} - |g||\psi|^2\psi, \tag{4.62}$$

and hence determine an expression for the chemical potential of the soliton.

4.4 Using the general bright soliton solution, Eq. (4.52), evaluate the soliton integrals of motion according to Eqs. (4.35)–(4.37). The soliton solution is already normalized to the number of atoms, N. Show that the bright soliton behaves as a classical particle with positive mass.

4.5 Consider a 3D bright soliton in a cylindrically-symmetric waveguide with tight harmonic confinement (of frequency ω_r) in r and no trapping along z. We can construct the ansatz for the soliton,

$$\psi(z, r) = A\,\mathrm{sech}\left(\frac{z}{l_r \sigma_z} \right) \exp\left(-\frac{r^2}{2 l_r^2 \sigma_r^2} \right), \tag{4.63}$$

where $l_r = \sqrt{\hbar/m\omega_r}$ is the harmonic oscillator length in the radial plane and σ_r and σ_z are the dimensionless variational length parameters.

(a) Normalize the ansatz to N atoms to show that $A = (N/2\pi l_r^3 \sigma_r^2 \sigma_z)$.
(b) Show that the variational energy of this ansatz is,

$$E = \hbar\omega_r N \left(\frac{1}{6\sigma_z^2} + \frac{1}{2\sigma_r^2} + \frac{\sigma_r^2}{2} + \frac{\gamma}{3\sigma_r^2 \sigma_z} \right), \tag{4.64}$$

where $\gamma = N a_s / l_r$.

(c) Make a 2D plot of the variational energy per particle, $E/N\hbar\omega_r$ (scaled by the transverse harmonic energy) as a function of the two variational length parameters, and plot this for $\gamma = -0.5$. Locate the variational solution in this 2D "energy landscape". Repeat for $\gamma = -1$; what happens to the variational solution? By varying γ estimate the critical value at which the solutions no longer exist (and they become prone to collapse).

4.6 Consider an object of mass M moving at velocity $\mathbf{v}_i$ which creates an excitation of energy E and momentum $\mathbf{p} = \hbar\mathbf{k}$. Show that Landau's critical velocity, $v_c = \min(E/p)$, is equivalent to $dE/dp = E/p$. Compare Landau's critical velocity for the ideal gas (dispersion relation $E(p) = p^2/2M$) against the weakly-interacting Bose gas. Finally show that in liquid helium II, Landau's critical velocity is $v_c \approx 60$ m/s. Hint: assume that near the roton minimum the dispersion relation, shown in Fig. 4.1b, has the approximate form $E(p) = \Delta_0 + (p - p_0)^2/(2\mu_0)$ where (at very low pressure) $\Delta_0 = 1.20 \times 10^{-22}$ J is the energy gap, $p_0 = \hbar k_0 = 2.02 \times 10^{-24}$ kg m/s is the momentum at the roton minimum, $\mu_0 = 0.161\, m_4$ is the effective roton mass, and $m_4 = 6.65 \times 10^{-27}$ kg is the mass of one ^{4}He atom.

References

1. M.R. Andrews et al., Phys. Rev. Lett. **79**, 553 (1997)
2. Y. Castin, R. Dum, Phys. Rev. Lett. **77**, 5315 (1996)
3. M.-O. Mewes et al., Phys. Rev. Lett. **77**, 416 (1996)
4. T. Dauxois, M. Peyrard, *Physics of Solitons* (Cambridge University Press, Cambridge, 2006)
5. M.J. Ablowitz, H. Segur, *Solitons and the Inverse Scattering Transform* (SIAM, Philadelphia, 1981)
6. P.G. Drazin, R.S. Johnson, *Solitons: An Introduction*, 2nd edn. (Cambridge University Press, Cambridge, 1989)
7. D.J. Frantzeskakis, J. Phys. A **43**, 213001 (2010)
8. Th Busch, J.R. Anglin, Phys. Rev. Lett. **84**, 2298 (2000)
9. S. Burger et al., Phys. Rev. Lett. **83**, 5198 (1999)
10. J. Denschlag et al., Science **287**, 97 (2000)
11. C. Becker et al., Nat. Phys. **4**, 496 (2008)
12. J. Brand, W.P. Reinhardt, Phys. Rev. A **65**, 043612 (2002)
13. T.P. Billam, A.L. Marchant, S.L. Cornish, S.A. Gardiner, N.G. Parker, Bright solitary matter waves: formation, stability and interactions, in *Spontaneous Symmetry Breaking, Self-Trapping and Josephson Oscillations*, ed. by B.A. Malomed (Springer, Berlin, 2013)
14. K.E. Strecker, G.B. Partridge, A.G. Truscott, R.G. Hulet, Nature **417**, 150 (2002)
15. L. Khaykovich et al., Science **296**, 1290 (2002)
16. J.H.V. Nguyen, P. Dyke, D. Luo, B.A. Malomed, R.G. Hulet, Nat. Phys. **10**, 918 (2014)
17. A.L. Marchant, T.P. Billam, T.P. Wiles, M.M.H. Yu, S.A. Gardiner, S.L. Cornish, Nat. Commun. **4**, 1865 (2013)
18. P. Nozieres, D. Pines, The Theory of Quantum Liquids (Perseus Books, Cambridge, 1999)
19. S. Serafini, M. Barbiero, M. Debortoli, S. Donadello, F. Larcher, F. Dalfovo, G.Lamporesi, G. Ferrari, Phys. Rev. Lett. **115**, 170402 (2015)
20. F. Dalfovo, Dynamics of trapped Bose-condensed gases in mean-field theory. in Proceedings of the International School of Physics Enrico Fermi, Bose-Einstein Condensation in Atomic Gases, ed. by M. Inguscio, S. Stringari, C.E. Wieman (IOS Press, Amsterdam, 1999)

21. L.P. Pitaevskii, S. Stringari, Bose-Einstein Condensation. International Series of Monographs on Physics (Oxford Science Publications, Oxford, 2003)

Chapter 5
Vortices and Rotation

Abstract As well as being free from viscosity, the Bose–Einstein condensate has another striking property—it is constrained to circulate only through the presence of whirlpools of fixed size and quantized circulation. In contrast, in conventional fluids, the eddies can have arbitrary size and circulation. Here we establish the form of these quantum vortices, their key properties, and how they are formed and modelled.

5.1 Phase Defects

The condensate's wavefunction is a complex quantity. We have seen that it can be written as $\Psi(\mathbf{r}, t) = R(\mathbf{r}, t)e^{iS(\mathbf{r},t)}$ (Madelung transform), where $R(\mathbf{r}, t)$ and $S(\mathbf{r}, t)$ are respectively the phase and amplitude distributions at time t. Consider following a closed path C of arbitrary shape through a region of the condensate. As we go around the path, the integrated change in the phase is

$$\Delta S = \oint_C \nabla S \cdot d\boldsymbol{\ell}, \tag{5.1}$$

where the vector $d\boldsymbol{\ell}$ is the line element of integration. Let the wavefunction be Ψ_0 and Ψ_1 respectively at the starting point and at the final point of C. Since the two points are the same and Ψ must be single-valued, the condition $\Psi_1 = \Psi_0$ means that,

$$\Delta S = 2\pi q, \qquad q = 0, \pm 1, \pm 2, \ldots \tag{5.2}$$

If the integer number $q \neq 0$ then, somewhere within the region enclosed by C, there must be a *phase defect*, a point where the phase wraps by the amount $2\pi q$. At this point the phase of the wavefunction takes on every value, and the only way that Ψ can remain single-valued here is if Ψ is exactly zero.

5.2   Quantized Vortices

What does the presence of a phase defect mean for the condensate as a fluid? Recalling that the phase distribution defines the fluid's velocity via $\mathbf{v} = (\hbar/m)\nabla S$, Eq. (5.2) implies that the *circulation* Γ around the path C is either zero or a multiple of the *quantum of circulation* κ,

$$\Gamma = \oint_C \mathbf{v} \cdot d\boldsymbol{\ell} = q\kappa, \qquad \kappa = \frac{h}{m}. \tag{5.3}$$

This important result (the *quantization of the circulation*) tells us that the condensate flows very differently from ordinary fluids, where the circulation takes arbitrary values.

Assume that $q \neq 0$, and that the path C is a circle of radius r centred at the singularity. Consider the simple case of two-dimensional flow in the xy plane. Using polar coordinates (r, θ), the line element is $d\boldsymbol{\ell} = r d\theta\, \widehat{\boldsymbol{e}}_\theta$, where $\widehat{\boldsymbol{e}}_\theta$ is the unit vector in the azimuthal direction θ. Then the circulation becomes,

$$\Gamma = \oint_C \mathbf{v} \cdot d\boldsymbol{\ell} = \int_0^{2\pi} r\mathbf{v} \cdot \widehat{\boldsymbol{e}}_\theta\, d\theta = 2\pi r v_\theta. \tag{5.4}$$

Comparison with Eq. (5.3) shows that the fluid's azimuthal speed around the singularity is,

$$v_\theta = \frac{q\hbar}{mr} = \frac{q\kappa}{2\pi r}. \tag{5.5}$$

Since the condensate is a fluid without viscosity, this flow around the singularity should go on forever, at least in principle!

For $q \neq 0$, Eq. (5.5) tells us that the velocity around the singularity decreases to zero at infinity ($v_\theta \to 0$ as $r \to \infty$), and that, as we approach the axis, the flow becomes faster and faster, and diverges ($v_\theta \to \infty$ as $r \to 0$). If we increase q, the flow speed increases discontinuously, because q takes only discrete values. The sign of q determines the direction of the flow (clockwise or anticlockwise) around the singularity.

We now have a better picture of the nature of the singularity: it is a *quantized vortex line*, a whirlpool in the fluid. The quantity q is called the *charge* of the vortex. Figure 5.1 (left) represents a straight vortex line through the origin, parallel to the z axis. Since the flow is the same on all planes perpendicular to the z axis, the flow of the (three-dimensional) straight vortex can be more simply described as the flow due to a two-dimensional *vortex point* on the xy plane, as in Fig. 5.1 (middle). If these conditions are not met, such as the curved vortex line shown in Fig. 5.1 (right), then the flow is fully three-dimensional and cannot be represented by a vortex point.
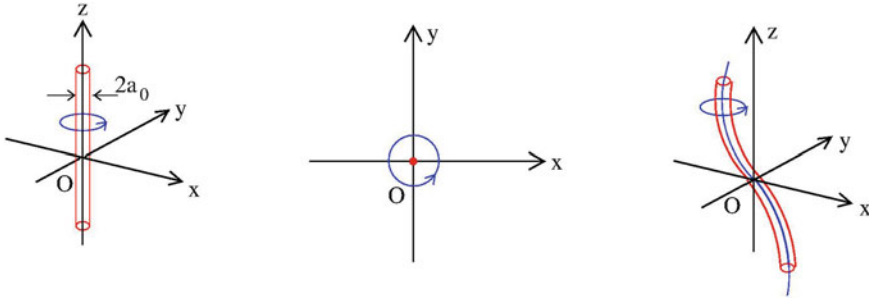
Fig. 5.1 *Left* Schematic (three-dimensional) straight vortex line through the origin and parallel to the *z* axis. The *red tube* around the vortex axis of radius a_0 represents the vortex core. *Middle* Since the vortex line is straight, it suffices to consider the two-dimensional flow of a vortex point on the *xy* plane (the flow on other planes parallel to the *xy* plane will be the same). *Right* For a more general bent vortex line the flow is fully three-dimensional

5.3   Classical Versus Quantum Vortices

The flow of the condensate is different from the flow of an ordinary fluid in two respects. Firstly, and as we showed in Sect. 3.3, it is inviscid (there is no viscosity to slow down the flow and bring it to a stop). Secondly, the circulation is quantized, as we showed above. To appreciate the second difference we recall the *vorticity* field (the local rotation), defined as,

$$\boldsymbol{\omega} = \nabla \times \mathbf{v}. \tag{5.6}$$

The following examples illustrate velocity fields with the associated vorticity fields:

(i) Consider water inside a bucket rotating at constant angular velocity Ω. We use cylindrical coordinates (r, θ, z) where z is the axis of rotation.[1] The velocity field is $\mathbf{v} = v_\theta \widehat{\boldsymbol{e}}_\theta = \Omega r \widehat{\boldsymbol{e}}_\theta$ and the vorticity is $\boldsymbol{\omega} = 2\Omega \widehat{\boldsymbol{e}}_z$ (where $\widehat{\boldsymbol{e}}_\theta$ and $\widehat{\boldsymbol{e}}_z$ are the unit vectors along θ and z). The azimuthal speed v_θ of this flow as a function of r is shown by case (i) of Fig. 5.2a. This flow is called *solid body rotation*.

(ii) As derived above, the velocity field around a vortex line in a condensate is $v_\theta = q\hbar/(mr)$, shown by case (ii) in Fig. 5.2a. It is easy to verify that its vorticity is zero: we say that this flow is *irrotational*. Physically, a parcel of fluid which goes around the vortex axis does not 'turn' (as it does in solid body rotation), but retains its orientation (like a gondola of a Ferris wheel); this flow is depicted in case (ii) of Fig. 5.2b. The property of irrotationality also follows mathematically: the condensate's velocity is proportional to the gradient of the

---

[1]We recall that in cylindrical coordinates, the curl of the vector $\mathbf{A} = (A_r, A_\theta, A_z)$ is

$$\nabla \times \mathbf{A} = \left(\frac{1}{r}\frac{\partial A_z}{\partial \theta} - \frac{\partial A_\theta}{\partial z}, \frac{\partial A_r}{\partial z} - \frac{\partial A_z}{\partial r}, \frac{1}{r}\frac{\partial (rA_\theta)}{\partial r} - \frac{1}{r}\frac{\partial A_r}{\partial \theta} \right).$$

.
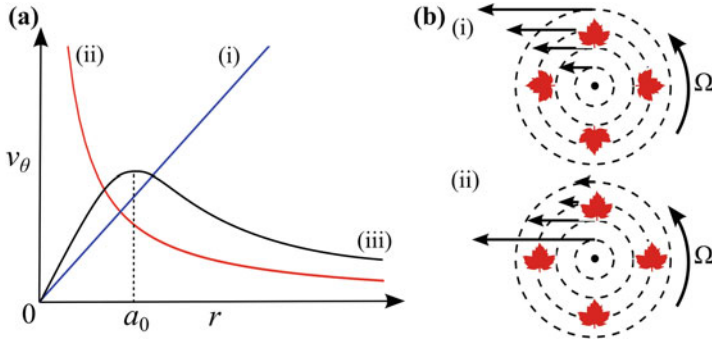
Fig. 5.2 a Examples of rotation curves. (i) solid body rotation, (ii) vortex line in a condensate (irrotational flow), and (iii) flow around a hurricane or a bathtub vortex, which combines solid body rotation in the inner region $r \ll a_0$ and irrotational flow in the outer region $r \gg a_0$. **b** Schematic of the two-dimensional flow for cases (i) and (ii), showing the orientation of an object, here a leaf, in the flow

quantum mechanical phase, and the curl of a gradient is always zero. However, the singularity itself contributes vorticity according to,

$$\boldsymbol{\omega} = \kappa \delta^2(\mathbf{r})\widehat{\boldsymbol{e}}_z, \tag{5.7}$$

where $\delta^2(\mathbf{r})$ is the two-dimensional delta function satisfying $\delta^2(\mathbf{r} = 0) = 1$ and $\delta^2(\mathbf{r} \neq 0) = 0$. At first it may surprise that a quantum vortex has zero vorticity, but the result is expected—the key point is that motion in the condensate is irrotational, but isolated vortex line singularities are allowed.

(iii) The velocity of the wind around the centre of a hurricane, case (iii) of Fig. 5.2a, combines solid body rotation in the inner region ($r \ll a_0$) with irrotational motion in the outer region ($r \gg a_0$) where a_0 is called the *vortex core radius*.

In ordinary fluids the vorticity $\boldsymbol{\omega}$ is arbitrary, and therefore vortices can be weak or strong, big or small. In a condensate, Eq. (5.3) is a strict quantum mechanical constraint: motion around a singularity has fixed form and intensity.

5.4   The Nature of the Vortex Core

A natural question is: what is the structure of the vortex, particularly towards the axis of the vortex ($r \rightarrow 0$), where, according to Eq. (5.5), the velocity becomes infinite? Using cylindrical coordinates (r, θ, z) again, we consider a straight vortex line aligned in the z direction in a homogeneous condensate ($V = 0$). Assuming
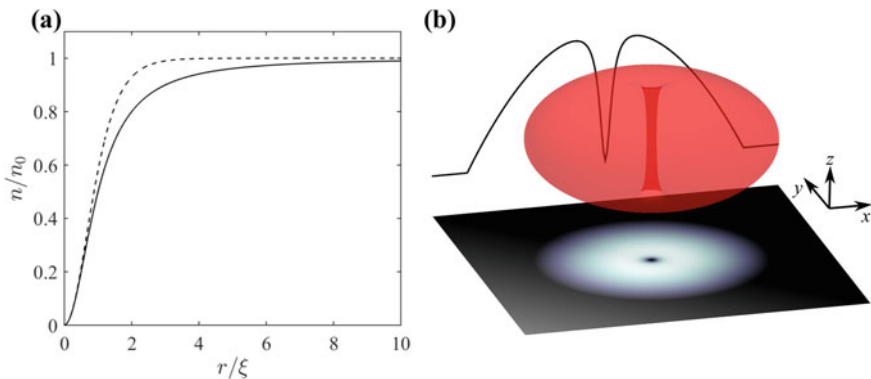
Fig. 5.3 a The radial density profile $n(r)$ of a $q = 1$ vortex in a homogeneous condensate (*solid line*). Shown for comparison is the 'healing' profile for a static condensate whose density is pinned to zero. **b** Appearance of a vortex lying along the axis of a trapped condensate. Shown is an isosurface of the 3D density (with the vortex appearing as a central tube), a 2D density profile column integrated along z (with the vortex appearing as a *black dot*), and a 1D density profile column-integrated along y and z

$\Psi(r, \theta, z) = A(r)e^{iq\theta}$ and substituting into the GPE of Eq. (3.9) we obtain the following differential equation,[2] for the function $A(r)$,

$$\mu A = -\frac{\hbar^2}{2m}\frac{1}{r}\frac{d}{dr}\left(r\frac{dA}{dr}\right) + \frac{\hbar^2 q^2}{2mr^2}A + gA^3, \qquad (5.9)$$

The terms on the right-hand side arise from the quantum kinetic energy, the kinetic energy of the circulating flow and the interaction energy, respectively. The boundary conditions are that $A(r) \to 0$ for $r \to 0$ and $A(r) \to \psi_0$ for $r \to \infty$. The equation has no exact solution and must be solved numerically for $A(r)$; the corresponding density profile $n(r) = A^2$ is shown in Fig. 5.3a. It is apparent that the axis of the vortex is surrounded by a region of depleted density, essentially a tube of radius $a_0 \approx 5\xi$, called the *vortex core radius*. For small r, the density scales as $r^{|q|}$. We see that although the velocity diverges for $r \to 0$, the density vanishes—no atom moves at infinite speed! We can therefore interpret a vortex as a 'hole' surrounded by (quantized) circulation. Recall from Sect. 3.4.2 that if a static and otherwise homogeneous condensate is pinned to zero density, then the density 'heals' back to the background density with a characteristic profile $\tanh^2(x/\xi)$. The vortex density profile is slightly wider than this profile and relaxes more slowly to the background density, as seen in

---

[2]We have expressed the Laplacian in its cylindrically symmetric form,

$$\nabla^2 = \frac{1}{r}\frac{\partial}{\partial r}\left(r\frac{\partial}{\partial r}\right) + \frac{1}{r^2}\frac{\partial^2}{\partial\theta^2} + \frac{\partial^2}{\partial z^2}. \qquad (5.8)$$

Fig. 5.3a. This is due to the kinetic energy of the circulating flow, which gives rise to an outwards centrifugal force on the fluid.

While there is no exact analytic form for the vortex density profile, a useful approximation for a single-charged vortex is,

$$n(r) = n_0 \left(1 - \frac{1}{1 + r'^2} \right),$$
(5.10)

where $r' = r/\xi$.

This result (a vortex line is a 'hole' surrounded by circulating flow) has an interesting mathematical consequence: a condensate with vortices is a multiply-connected region, and the classical Stokes Theorem[3] does not apply.

In a trapped condensate the vortex creates a similar tube surrounded by quantised circulation; the only difference is that the density of the condensate is not uniform (as in a homogeneous condensate). In typical 2D column-integrated images of the condensate, the vortex appears as a low density dot. Since the healing length depends on the local density, in a trapped condensate the thickness of the vortex core depends on the position. If the condensate is in the Thomas–Fermi regime and the vortex along the z axis, then an approximation for the density profile can be constructed as the product of the static Thomas–Fermi profile, Eq. (3.33), and the vortex density, Eq. (5.10), i.e.,

$$n(x, y, z) = n_0 \left(1 - \frac{x^2}{R_x^2} - \frac{y^2}{R_y^2} - \frac{z^2}{R_z^2} \right) \left(1 - \frac{1}{1 + r'^2} \right),$$
(5.11)

where $r' = r/\xi$ is defined is terms of the healing length evaluated at the condensate centre.

5.5   Vortex Energy and Angular Momentum

We now evaluate some useful properties associated with a quantum vortex: its energy and angular momentum. For simplicity, we still consider the case of a single straight vortex lying along the z-axis of a cylindrically-symmetric condensate of constant density; assuming that the condensate's size is much larger than the healing length, the density depletion at the axis of the vortex and near the walls can be neglected. A cylindrical bucket of height H_0 and radius R_0 containing superfluid liquid helium would be a realistic example. For trapped atomic condensates, where the vortex size

---

[3]Stokes Theorem states that

$$\oint_C \mathbf{A} \cdot d\boldsymbol{\ell} = \int_S (\nabla \times \mathbf{A}) \cdot d\mathbf{S},$$

where the surface S enclosed by the oriented curve C is simply-connected, i.e. any closed curve on S can be shrunk continuously to a point within S.

is significant relative to the system size and the condensate density varies in space, these ideas can be generalized by, for example, taking the density profile to be of the form of Eq. (5.11), or by estimating the necessary integrals numerically.

The kinetic energy E_{kin} of the swirling fluid is obtained from summing the contributions of the atoms, each carrying kinetic energy $mv_\theta^2/2$ where $\mathbf{v} = v_\theta \widehat{\boldsymbol{e}}_\theta = (q\hbar/mr)\,\widehat{\boldsymbol{e}}_\theta$ is the velocity. Summing over all atoms we have,

$$E_{\mathrm{kin}} = \int \frac{1}{2} mn(\mathbf{r}) v_\theta^2(\mathbf{r})\,\mathrm{d}^3\mathbf{r}, \tag{5.12}$$

where the integral is performed over the bucket's volume. Using cylindrical coordinates,

$$E_{\mathrm{kin}} = \int_0^{H_0} \mathrm{d}z \int_0^{2\pi} \mathrm{d}\theta \int_0^{R_0} \frac{mn_0}{2} \left(\frac{q\hbar}{mr}\right)^2 r\,\mathrm{d}r = \pi H_0 \frac{n_0 q^2 \hbar^2}{m} \int_0^{R_0} \frac{\mathrm{d}r}{r}. \tag{5.13}$$

To prevent the integral from diverging at $r \to 0$ we introduce a cutoff length a_0,[4] the vortex core radius; in doing so, we recognize that the density vanishes at the axis of the vortex, but simplify the core structure, assuming that the core is hollow up to the distance $r = a_0$. Notice that without the outer limit of integration (the size of the container R_0) the integral would also diverge at $r \to \infty$. We then obtain,

$$E_{\mathrm{kin}} = \pi H_0 \frac{n_0 q^2 \hbar^2}{m} \int_{a_0}^{R_0} \frac{\mathrm{d}r}{r} = \pi H_0 \frac{n_0 q^2 \hbar^2}{m} \ln\left(\frac{R_0}{a_0}\right). \tag{5.14}$$

We conclude that the kinetic energy per unit length of the vortex, $E_{\mathrm{kin}}/H_0 = \pi n_0 (q^2 \hbar^2/m) \ln(R_0/a_0)$, is constant.

Each atom swirling around the axis of the vortex carries angular momentum $L_z = mv_\theta r$. The total angular momentum of the flow is therefore,

$$L_z = \int mn(\mathbf{r}) v_\theta(\mathbf{r}) r\,\mathrm{d}^3\mathbf{r}. \tag{5.15}$$

Proceeding as for the kinetic energy, we find,

$$L_z = 2\pi H_0 n_0 q\hbar \left(\frac{R_0^2}{2} - \frac{a_0^2}{2}\right) \approx \pi H_0 n_0 q\hbar R_0^2. \tag{5.16}$$

Consider a condensate in a state with an arbitrary high angular momentum L_z. We can construct this state as either (i) one vortex with large q or (ii) many vortices with $q = 1$. Which situation is preferred? Since E_{kin} scales as q^2, a state with many singly-charged vortices has less energy than a state with a single multi-charged

---

[4]Often this cutoff is taken instead as the healing length ξ.

vortex. Experiments confirm that this is indeed the case: in Ref. [1] a $q = 2$ vortex was seen to quickly decay into two singly-charged vortices. Hereafter we assume that all vortices are singly-charged, with $q = \pm 1$.

5.6 Rotating Condensates and Vortex Lattices

5.6.1 Buckets

Vortices are easily created by rotating the condensate [22, 23]. Consider again a cylindrical condensate of height H_0, radius R_0 and uniform density. A vortex appears only if the system, by creating a vortex, lowers its energy. In a rotating system at very low temperature, it is not the energy E which must be minimized, but rather the free energy $F = E - \Omega L_z$ where Ω is the angular velocity of rotation. A state without any vortex, hence without angular momentum, has free energy $F_1 = E_0$ where E_0 is the internal energy. A state with a vortex has free energy $F_2 = E_0 + E_{\text{kin}} - \Omega L_z$. The free energy difference is thus,

$$\Delta F = F_2 - F_1 = E_{\text{kin}} - \Omega L_z = 2\pi H_0 \frac{\hbar^2}{m^2} \ln\left(\frac{R_0}{a_0}\right) - \Omega \pi H_0 n_0 \hbar R_0^2. \quad (5.17)$$

Therefore $\Delta F < 0$ (the free energy is reduced by creating a vortex) provided that the rotational velocity is larger than a critical value Ω_{c1},

$$\Omega > \Omega_{c1} = \frac{\hbar}{m R_0^2} \ln\left(\frac{R_0}{a_0}\right). \quad (5.18)$$

For superfluid helium ($m = 6.7 \times 10^{-27}$ kg, $\kappa = 9.97 \times 10^{-8}$ m^2/s, $a_0 \approx 10^{-10}$ m) inside a container of radius $R_0 = 10^{-2}$ m, the critical angular velocity is $\Omega_{c1} = 3 \times 10^{-3}$ s^{-1}. States with two, three and more vortices onset at higher critical velocities Ω_{c2}, Ω_{c3} etc., as shown in Fig. 5.4 for superfluid helium and in Fig. 5.7 for atomic condensates. Note that the vortices are parallel to the rotation axis and arrange themselves in a *vortex lattice* like atoms in a crystal with triangular symmetry. The vortex lattice is therefore a steady configuration in the frame of reference rotating at angular velocity Ω.

Vortices are topological defects which can only be created at a boundary or spontaneously with an oppositely-charged vortex.[5] Where then do the vortices in a vortex lattice originate from?

For a rotating container of helium, with even a relatively small rotation frequency, the roughness of the container surface is expected to seed vortices, providing a

---

[5] An exception is through the technique of phase imprinting, in which the condensate phase can be directly and almost instantaneously imprinted with a desired distribution. In this manner vortices can be suddenly formed within the condensate.
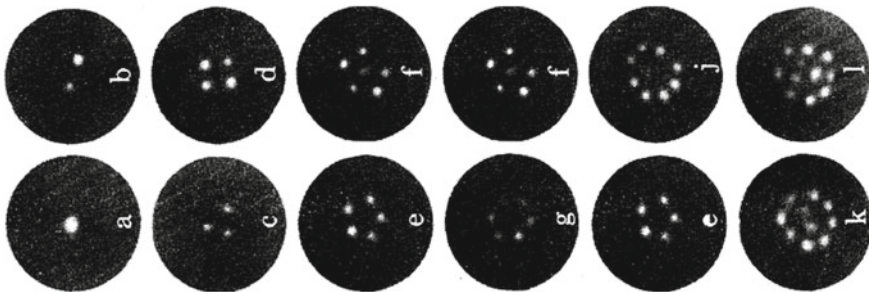
Fig. 5.4 Experimental images of vortex lattices at increasing angular velocities Ω in superfluid helium. Reprinted figure with permission from [3]. Copyright 1979 by the American Physical Society

constant source of vortices from which to develop a vortex lattice in the bulk if the critical rotation frequency is exceeded.

According to *Feynman's rule*, the density of vortices (number of vortices per unit area) is,

$$n_v = \frac{2\Omega}{\kappa}. \tag{5.19}$$

Since each vortex contributes vorticity according to Eq. (5.7), the average vorticity per unit area is,

$$\bar{\omega} = \kappa n_v \widehat{e}_z = 2\Omega \widehat{e}_z. \tag{5.20}$$

This tells us that the averaged vorticity (averaged over distance larger than the inter-vortex spacing) reproduces the vorticity 2Ω of an ordinary fluid in rotation. Similarly, the large-scale azimuthal flow is $\mathbf{v} \approx \Omega r \widehat{e}_\theta$. Remarkably, the many quantized vortices mimic classical solid body rotational flow. Note that the local velocity field around vortices can remain rather complicated.

In the frame rotating at angular frequency Ω about the z-axis, the GPE of Eq. (3.46) is,

$$i\hbar \frac{\partial \psi}{\partial t} = -\frac{\hbar^2}{2m}\nabla^2 \psi + g|\psi|^2 \psi + V\psi + \Omega L_z \psi - \mu\psi, \tag{5.21}$$

where,

$$L_z = i\hbar \left(y\frac{\partial}{\partial x} - x\frac{\partial}{\partial y} \right), \tag{5.22}$$

is the angular momentum operator in the z direction. The vortex lattices are the ground-state stationary solutions of this equation (providing Ω is large enough). Figure 5.5 shows such a vortex lattice solution for a condensate being rotated in a bucket. The above bucket scenario is modelled through the *bucket potential*,
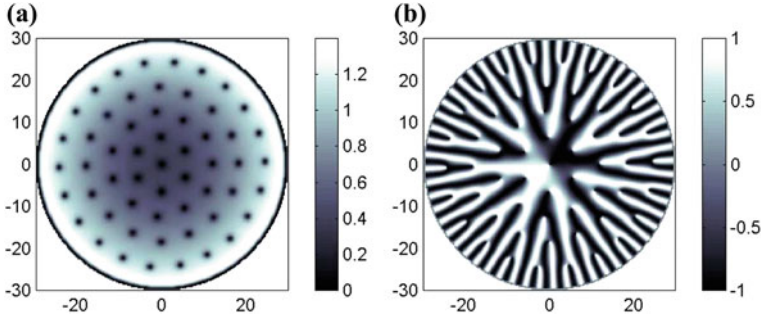
Fig. 5.5 Vortex lattice formed in a bucket potential rotating about the z-axis. Shown are the **a** density (in arbitrary units) and **b** phase (in units of π) in the xy-plane (position presented in units of the healing length ξ), corresponding to the stationary solution of the rotating-frame GPE of Eq. (5.21). The bucket has radius $R = 29\xi$ and the rotation frequency is $\Omega = 0.08\,c/\xi$. Image courtesy of Thomas Winiecki [2]

$$V(r) = \begin{cases} 0 & \text{if } r \leq R_0, \\ \infty & \text{if } r > R_0. \end{cases} \qquad (5.23)$$

The lattice features $N_v = 56$ vortices. Note the appearance of the phase "dislocations" in the phase profile at each vortex position. At the boundary there are as many 2π phase slips as there are vortices. The average flow speed around the edge of the bucket can then be approximated by evaluating the magnitude of $\mathbf{v} = (\hbar/m)\nabla S$ around the boundary, i.e.,

$$v_r(r = R_0) = \frac{\hbar}{m}\frac{2\pi N_v}{2\pi R_0} = \frac{\hbar}{m}\frac{56}{29\xi} \approx 1.93c. \qquad (5.24)$$

This is close to what one would expect for solid body rotation, $v_r(r = R_0) = \Omega R_0 = 2.3c$.

In a small system, at the same value of Ω one often observes vortex configurations which are slightly different from each other. This is because there is a very small energy difference between these slightly rearranged states. For example, Fig. 5.4 shows two states with six vortices each (in one case the six vortices are distributed around a circle, in the other case there are five vortices around a circle and one vortex in the middle).

Notice how the background density for the rotating bucket solution in Fig. 5.5 features a *meniscus*, that is, it is raised towards the edge of the bucket. Let us determine this background density profile. We denote the rotation vector $\mathbf{\Omega} = \Omega\widehat{\mathbf{e}}_z$.

Recall the fluid interpretation of the GPE. Using the Madelung transformation $\psi = \sqrt{n}e^{iS}$ and the fluid velocity definition $\mathbf{v} = (\hbar/m)\nabla S$, the rotating-frame GPE of Eq. (5.21) is equivalent to the modified fluid equations,

$$\frac{\partial n}{\partial t} = -\nabla \cdot [n(\mathbf{v} - \boldsymbol{\Omega} \times \mathbf{r})], \tag{5.25}$$

$$m\frac{\partial \mathbf{v}}{\partial t} = -\nabla \cdot \left(\frac{1}{2}mv^2 + V + gn - \frac{\hbar^2}{2m}\frac{\nabla^2 \sqrt{n}}{\sqrt{n}} - m\mathbf{v} \cdot [\boldsymbol{\Omega} \times \mathbf{r}]\right), \tag{5.26}$$

where the $\boldsymbol{\omega} \times \mathbf{r}$ terms account for frame rotation and $\mathbf{v}$ is the velocity field in the laboratory frame (expressed in the coordinates of the rotating frame). We assume the Thomas–Fermi approximation by neglecting the quantum pressure term in Eq. (5.26), and seek the stationary density profile. Setting $\partial \mathbf{v}/\partial t = 0$ and integrating gives,

$$\frac{1}{2}mv^2 + V + gn - m\mathbf{v} \cdot [\boldsymbol{\Omega} \times \mathbf{r}] = \mu, \tag{5.27}$$

where the chemical potential μ is the integration constant.

We consider a coarse-grained scale, ignoring the structure of the individual vortices and for which the velocity field approximates the solid body form $\mathbf{v}(r) = \Omega r \widehat{\boldsymbol{e}}_\theta$. We then obtain,

$$gn + V - \frac{1}{2}m\Omega^2 r^2 = \mu, \tag{5.28}$$

where we have used $\widehat{\boldsymbol{e}}_z \times \widehat{\boldsymbol{e}}_r = \widehat{\boldsymbol{e}}_\theta$. Rearranging for the density,

$$n(r) = \frac{1}{g}\left(\mu - V + \frac{1}{2}m\Omega^2 r^2\right), \tag{5.29}$$

which is valid for $n(r) > 0$; otherwise $n(r) = 0$. We conclude that rotation causes a parabolic increase in the coarse-grained density, consistent with the behaviour visible in Fig. 5.5. The is due to centrifugal effects, and is observed in rotating classical fluids. Note that μ can be determined by normalizing the profile to the required number of atoms or average density.

5.6.2 Trapped Condensates

To predict the critical rotation frequency for vortices to become favoured in a harmonically-trapped condensate, one can repeat the above approach but the inhomogeneous density profile must be accounted for (i.e. replacing n_0 above with $n(\mathbf{r})$). One way to approximate this is by the Thomas–Fermi density profile. For a trap which is symmetric in the plane of rotation, with frequency $\omega_\perp$, the critical rotation frequency is then,

$$\Omega_{c1} = \frac{5}{2}\frac{\hbar}{m R_\perp^2} \ln\left(\frac{0.67 R_\perp}{\xi}\right), \tag{5.30}$$

where $R_\perp$ is the Thomas–Fermi radius in the plane of rotation. For typical atomic condensates, $\Omega_{c1} \sim 0.3\omega_\perp$.

Rotating an axi-symmetric harmonic trap applies no torque to the condensate, and so in practice the trap is made slightly anisotropic in the plane of rotation in order to form a vortex lattice. Surprisingly, experiments observed vortices at rotation frequencies $\Omega \sim 0.7\omega_\perp$, considerably higher than the frequency at which they become energetically favourable. The traps are so smooth that vortex nucleation is very different to that of helium.

We can examine this by considering the planar potential to be weakly elliptical, with frequencies $\omega_x = \sqrt{1-\epsilon}\omega_\perp$ and $\omega_y = \sqrt{1+\epsilon}\omega_\perp$, where ϵ is the *trap ellipticity*. We follow the approaches of Refs. [6, 7]. We seek the stationary solutions of the trapped vortex-free condensate under rotation about z. Under the Thomas–Fermi approximation, the solutions must satisfy Eq. (5.27). Furthermore, we look for solutions with the phase profile, and corresponding velocity profile, given by,

$$S(x, y) = \beta xy, \quad \mathbf{v}(x, y) = \frac{\hbar}{m}\nabla S = \frac{\beta\hbar}{m}(y\widehat{\boldsymbol{e}}_x + x\widehat{\boldsymbol{e}}_y). \tag{5.31}$$

where β is a parameter to be determined below. Inserting into Eq. (5.27), and noting that $\boldsymbol{\Omega} \times \mathbf{r} = \Omega(x\widehat{\boldsymbol{e}}_y - y\widehat{\boldsymbol{e}}_x)$, leads to the density profile,

$$n = \frac{1}{g}\left(\mu - \frac{1}{2}(m\tilde{\omega}_x^2 x^2 + \tilde{\omega}_y^2 y^2 + \omega_z^2 z^2)\right), \tag{5.32}$$

where the effect of the rotation is to introduce *effective trap frequencies* in the xy-plane,

$$\tilde{\omega}_x^2 = (1-\epsilon)\omega_\perp^2 + \beta^2 - 2\beta\Omega, \tag{5.33}$$
$$\tilde{\omega}_y^2 = (1+\epsilon)\omega_\perp^2 + \beta^2 + 2\beta\Omega. \tag{5.34}$$

Plugging this density profile into the rotating-frame continuity equation, Eq. (5.25), and setting $\partial n/\partial t = 0$, leads to an expression for β,

$$\beta^3 + \beta(\omega_\perp^2 - 2\Omega^2) - \epsilon\Omega\omega_\perp^2 = 0. \tag{5.35}$$
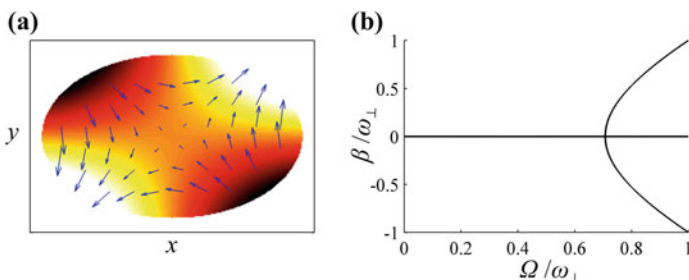
Fig. 5.6 a Illustration of the irrotational flow pattern of a rotating elliptically-trapped condensate, according to Eq. (5.31). The color indicates the phase $S(x, y)$ while the velocity field is shown by *arrows*. **b** The velocity field amplitude β as a function of rotation frequency Ω for an axi-symmetric trap ($\epsilon = 0$). At $\Omega = \omega_\perp/\sqrt{2}$ the solutions trifurcate. In this region, these solutions become unstable

Hence the stationary solution of the condensate in the rotating frame has been completely specified. In the laboratory frame, this solution has an elliptical density profile which rotates about z. However, the fluid remains irrotational, thanks to the special velocity field which distorts the density is such a way as to mimic rotation, as depicted in Fig. 5.6a.

Analysing the case of $\epsilon = 0$ for simplicity, there exists one solution, with $\beta = 0$, for $\Omega \leq \omega_\perp/\sqrt{2}$; this represents a motion-less and axi-symmetric condensate. However, for $\Omega > \omega_\perp/\sqrt{2}$ the solutions trifurcate, with two new branches with $\beta \neq 0$ and corresponding to non-axi-symmetric solutions of the form shown in Fig. 5.6. This trifurcation leads to an instability of the condensate (as can be confirmed via linearizing about these solutions [7]) in which perturbations grow at the condensate
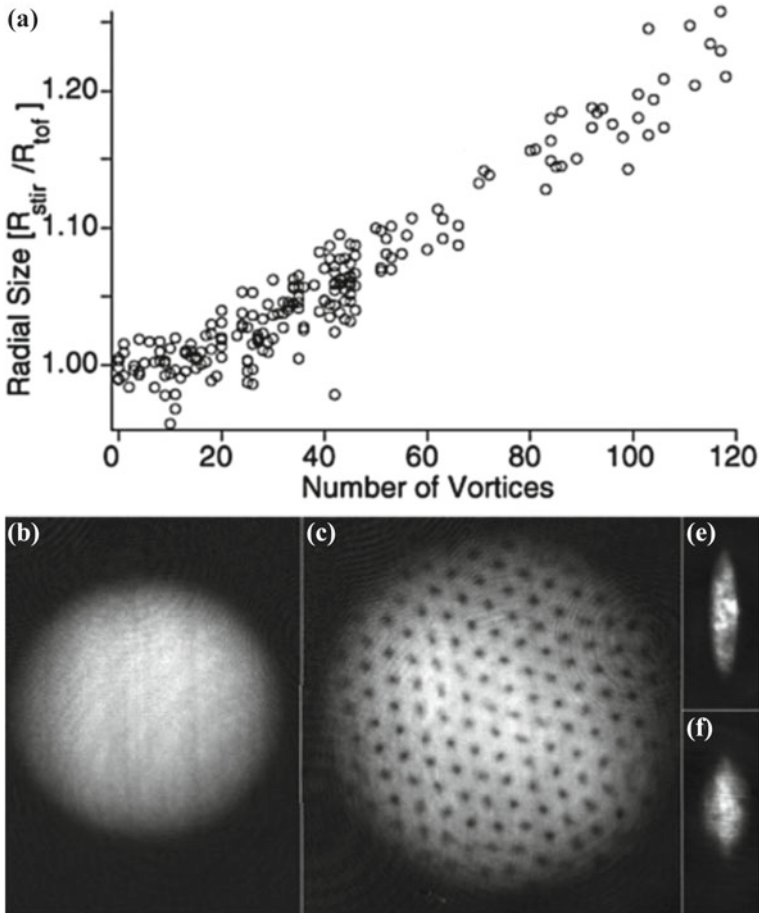
Fig. 5.7 An experimental vortex lattice **c** formed in a flattened trapped rotating atomic condensate (image represents the condensate density). **b** shows the profile of the corresponding non-rotating condensate. **d** and **e** show the side views of the non-rotating and rotating condensates, respectively. The condensate grew in radius with the number of vortices, as shown in **a**. Reprinted figure with permission from [5]. Copyright 2001 by the American Physical Society

surface and develop into vortices. Experiments [8] and simulations [9] of the GPE show that this instability then allows the condensate to evolve into a vortex lattice, the lowest energy state.

Figure 5.7 shows a vortex lattice produced in a rotating trapped atomic condensate. Note the regularity and density of the vortex lattice. Note also that the rotating condensate is significantly broader than the non-rotating condensate. In the presence of the vortex lattice, we can predict the coarse-grained density profile of the condensate. Considering an axi-symmetric trap ($\omega_x = \omega_y \equiv \omega_\perp$), then the coarse-grained density profile of Eq. (5.29) gives,

$$n(r) = \frac{1}{g}\left(\mu - \frac{1}{2}m(\omega_r^2 r^2 - \Omega^2)r^2\right). \tag{5.36}$$

There is a competition between the quadratic trapping potential, which pushes atoms inwards, and the quadratic centrifugal potential, which pushes atoms outwards. The net potential is quadratic with effective harmonic potential $\omega_r^2 - \Omega^2$. As Ω is increased, the condensate expands, and when $\Omega \geq \omega_r$ it becomes untrapped!

5.7   Vortex Pairs and Vortex Rings

An important property of a vortex is that it moves with the local fluid velocity, and this means that two vortices in proximity induce each other to move. We now consider some important examples.

5.7.1   Vortex-Antivortex Pairs and Corotating Pairs

Consider a pair of vortices of opposite circulation and separation d, a state called a *vortex-antivortex pair* or *vortex dipole*, shown schematically in Fig. 5.8. In the figure, the flow around the vortex at the left is anticlockwise, and the flow around the anti-vortex at the right is clockwise. Each vortex is carried along by the flow field of the other vortex, and at each vortex the flow field has speed $v = \hbar/md$ acting perpendicular to the line separating the vortices. Moreover, this flow acts in the *same direction* for both vortices, and hence they propagate together at this speed.

If instead the vortices have the same circulation, then the flow which carries each vortex now acts in *opposite directions* (again, perpendicular to the line separating the vortices and with the above speed). The net effect is for the vortices to *co-rotate* about their mid-point. The angular frequency of this motion is $\omega = 2v/d = 2\hbar/md^2$. From this simple example, one can imagine how many vortices of the same circulation rotate together in a vortex lattice. Note that the above predictions for the pair speed ignore core effects, and so are only valid for $d \gg a_0$.

Fig. 5.8 Schematic of a vortex-antivortex pair
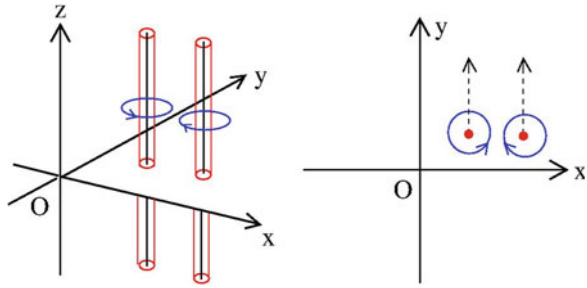
We can estimate the energy of the vortex pairs in a cylindrical condensate (radius R_0, height H_0) by assuming a uniform density and integrating the kinetic energy, as we did to calculate the energy of a single vortex line in Eq. (5.14). The vortices have circulation q_1 and q_2, and individual velocity fields $\mathbf{v}_1$ and $\mathbf{v}_2$, respectively. The net velocity field of the two vortices is $\mathbf{v}_1 + \mathbf{v}_2$. Assuming $\xi \ll d \ll R_0$ then the (kinetic) energy of the pair is,

$$E_{\text{kin}} = \int mn_0 |\mathbf{v}_1 + \mathbf{v}_2|^2 \, d\mathbf{r} = \frac{\pi n_0 H_0 \hbar^2}{m} \left[q_1^2 \ln \frac{R_0}{a_0} + q_2^2 \ln \frac{R_0}{a_0} + 2q_1 q_2 \ln \frac{R_0}{d} \right]. \quad (5.37)$$

The first two terms are the energies of the individual vortices if they were isolated. The second term is the *interaction energy*, the change in energy arising from the interaction between the vortices. For a vortex-antivortex pair ($q_1 = -q_2$) the interaction energy is negative. This is because the flow fields tend cancel out in the bulk, reducing the total kinetic energy. Indeed, in the limit $d \to a_0$, the flow fields completely cancel and the total energy tends to zero; in reality the vortices annihilate with each other in this limit. For a corotating pair ($q_1 = q_2$), the interaction energy is positive; in the bulk the flow fields tend to reinforce, increasing the total kinetic energy.

In the presence of dissipation on the vortices, this result also informs us that vortex-antivortex pairs will shrink (ultimately annihilating when their cores begin to overlap) and corotating pairs will expand. Interestingly, at finite temperature and in 2D condensates, vortex-antivortex pairs can be created spontaneously [10].

5.7.2 Vortex Rings

A vortex line either terminates at a boundary (e.g. the vortex in the cylindrical container discussed in the previous section) or is a closed loop. A circular vortex loop is called a *vortex ring*. It is the three-dimensional analog of the (two-dimensional) vortex-antivortex pair: each element of the ring moves due to the flow induced by the rest of the ring, resulting in the ring travelling in a straight line at a constant speed
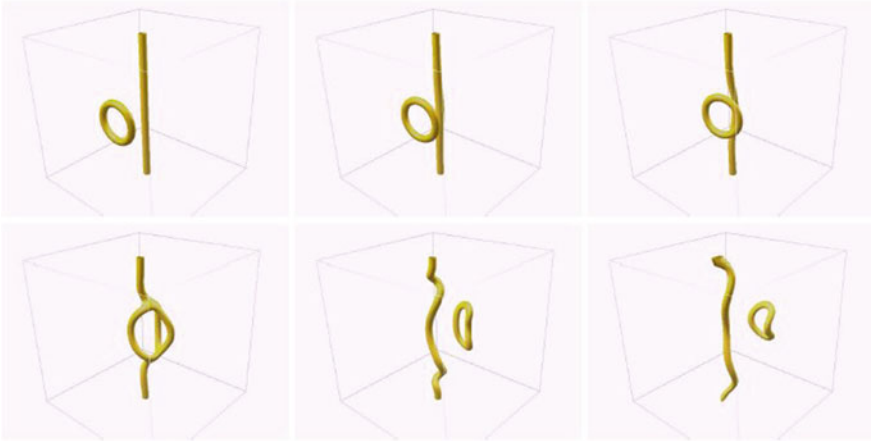
Fig. 5.9 Vortex ring travelling towards a vortex line computed by numerically solving the GPE (courtesy of A.J. Youd) in a periodic box (hence the vortex line appears to terminate at the *top* and at the *bottom*)

which is inversely proportional to its radius. Figure 5.9 shows a vortex ring travelling towards, and interacting with, a straight vortex line.

Both vortex rings and vortex-antivortex pairs are forms of solitary waves, since they propagate without spreading. Moreover, like dark solitons, they are stationary (excited) solutions of the homogeneous condensate in the frame moving with the ring/pair.

5.7.3   Vortex Pair and Ring Generation by a Moving Obstacle

Vortex rings are easily generated in ordinary fluids by pushing the fluid through an orifice: cigarette smokers, volcanoes and dolphins can make vortex rings. In condensates and helium, rings and vortex-antivortex pairs can be formed by moving obstacles.

To understand this mechanism, recall Landau's criterion for the generation of excitations in the condensate (Sect. 4.2). In the hydrodynamic picture, the speed of the atom/impurity is replaced by the local fluid velocity. Consider the scenario of a homogeneous condensate flowing with bulk speed v_∞ past a cylindrical obstacle (this is equivalent to the cylindrical obstacle moving at speed v_∞ through a static condensate but more convenient to simulate). For low v_∞, the condensate undergoes undisturbed laminar flow around the obstacle, as shown in Fig. 5.10 (left). Note that the local flow speed is approximately twice as large, i.e. $2v_\infty$ at the poles of the obstacle than it is in the bulk (indeed, for an inviscid Euler fluid one would expect it to be exactly $2v_\infty$). When $v_\infty \approx 0.5c$, the local flow at the poles exceeds the speed
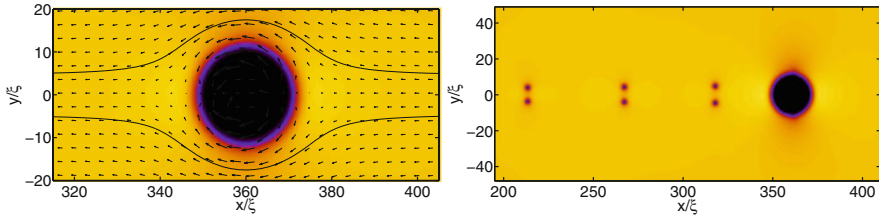
Fig. 5.10 Flow of a homogeneous condensate past a cylindrical obstacle, below (*left*) and above (*right*) the critical velocity. Shown is the condensate density, and the *arrows* (*left*) show the velocity field. Note that the obstacle punches a large hole in the condensate. Results are based on simulations of the 2D GPE in the moving frame. Figure reproduced from Ref. [11] under a CC BY licence
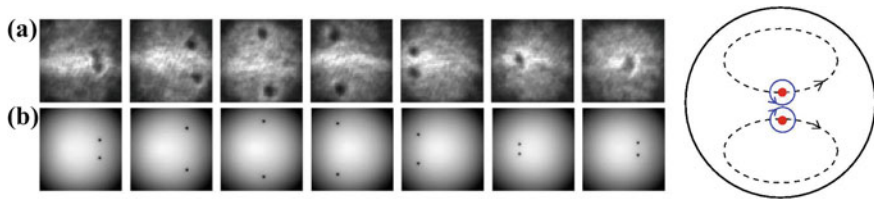

Fig. 5.11 a Experimental images of a vortex-antivortex pair moving within a trapped condensate. **b** The vortex-antivortex pair's trajectory is reproduced by numerically solving the GPE. Note that the vortex core appears larger in the experimental images since the condensate is first expanded to aid in resolving the cores. Figure adapted with permission from Ref. [14]. Copyrighted by the American Physical Society. A schematic of the trajectory of a vortex-antivortex pair in a trapped condensate is shown on the *right*

of sound, and, as per Landau's prediction, excitations are created. These take the form of pairs of opposite circulation vortices, which periodically peal off from the poles of the obstacle and travel downstream, as seen in Fig. 5.10 (right).

This process has been studied experimentally in atomic condensates [14, 15]. The obstacle is engineered by a laser beam which exerts a localized repulsive potential on the condensate, and is moved relative to the condensate. Figure 5.11 shows an experimental vortex-antivortex pair which moves within a trapped condensate (top). The dynamics can be reproduced by simulating the GPE (bottom). Note that whereas in an infinite condensate the vortex-antivortex pair has constant translational velocity, within a harmonically-trapped condensate the motion of each vortex of the pair follows a curved trajectory.

Similarly, vortex rings arise when a spherical obstacle exceeds a critical speed relative to the condensate. They can be created in superfluid helium by injecting electrons with a sharp high-voltage tip; the electron's zero point motion carves a small, charged spherical bubble in the liquid of radius approximately 16×10^{-10} m which can be accelerated by an applied electric field. Upon exceeding a critical velocity, a vortex ring peels off at the bubble's equator; subsequently the electron falls into the vortex core, leaving a vortex ring with an electron bubble attached; the last part of the sequence is shown in Fig. 5.12.
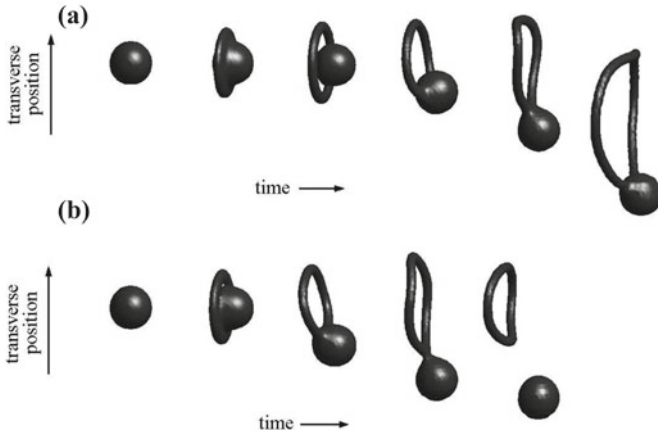
Fig. 5.12 Vortex rings nucleated by moving bubbles, computed by numerically solving the GPE. Figure reproduced from [16] with permission from EDP Sciences

## 5.8 Motion of Individual Vortices

We have seen how vortices move due to their interactions with other vortices. Isolated vortices can also move under a variety of scenarios.

First imagine a condensate in a static bucket with a straight vortex line positioned close to the edge. The fluid velocity must be zero at the boundary. In effect, it is as if an *image vortex*, with opposite circulation, exists on the other side of the boundary. As such the vortex moves around the boundary of the container as a virtual pair with its image.

In a harmonically-trapped condensate, an off-centre vortex precesses about the trap centre. The slow variation of the density towards the edge complicates an image interpretation. Instead, we can interpret the precession in terms of a Magnus force. Imagine the vortex line as a rotating cylinder, shown in Fig. 5.13 (left). The vortex line feels a radial force due to its position in the condensate, and this gives rise to a motion of the vortex line which is perpendicular to the force, $\mathbf{v}_L$, an effect well known in classical hydrodynamics. This force can be deduced from the free energy of the system. This energy decreases with the vortex position, r_0, as shown in Fig. 5.13 (right). This radial force, which follows as $-\partial E/\partial r_0$, acts outwards and has contributions from the "buoyancy" of the vortex, which behaves like a bubble, as well as its kinetic energy. This force balances the Magnus force $-mn\kappa \times \mathbf{v}_L$, leading to the expression,

$$\frac{\partial E}{\partial r_0}\widehat{\mathbf{e}}_r = mn\boldsymbol{\kappa} \times \mathbf{v_L}, \tag{5.38}$$

where κ is the circulation vector. The net effect is a precession of the vortex about the trap centre. More generally, the vortex follows a path of constant free energy;
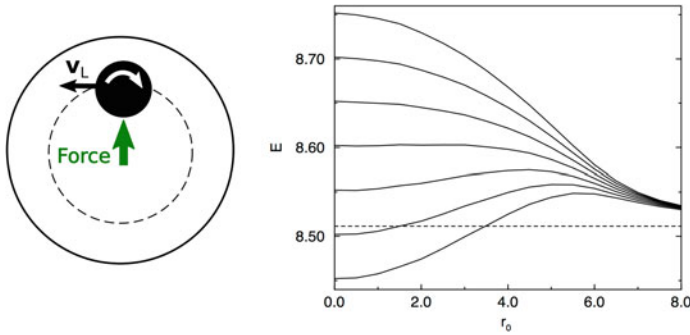
Fig. 5.13 *Left* Schematic of the Magnus effect which causes an off-centre vortex to precess in a trapped condensate. *Right* Free energy E of a trapped condensate versus the radial position of a vortex, r_0. The *top line* is for a non-rotating system, while the *lower lines* have increasing rotation frequencies. Reprinted figure with permission from [17]. Copyright 1999 by the American Physical Society

for example, it will trace out a circular path in an axi-symmetric harmonic trap and an elliptical path in a non-axi-symmetric harmonic trap. The experiment of Ref. [18] pioneered the real-time imaging of vortices in condensates and was able to directly monitor the precession of a vortex, finding it to agree well with theoretical predictions.

At the trap centre, $E(r_0)$ becomes flat such that the vortex ceases to precess; in fact, the trapped condensate with a central vortex line is a stationary state. For a non-rotating condensate, this state is energetically unstable ($E(r_0)$ is a maximum at the origin). Under sufficiently fast rotation, however, $E(r_0)$ changes shape such that this state becomes a minimum and thus energetically stable, consistent with discussion in Sect. 5.6.

This analysis assumes the vortex line to be straight. This is valid is flattened, quasi-2D geometries, but in 3D geometries, the vortex line can bend and support excitations.

5.9 Kelvin Waves

A sinusoidal or helical perturbation of the vortex core away from its rest position is called a *Kelvin wave*. Figure 5.14 (left) shows a Kelvin wave of amplitude A and wavelength λ. A Kelvin wave of infinitesimal amplitude A and wavelength $\lambda \gg a_0$ rotates with angular velocity,

$$\omega_0 \approx \frac{\kappa k^2}{4\pi} \left(\ln \left(\frac{1}{ka_0} \right) - 0.116 \right), \tag{5.39}$$
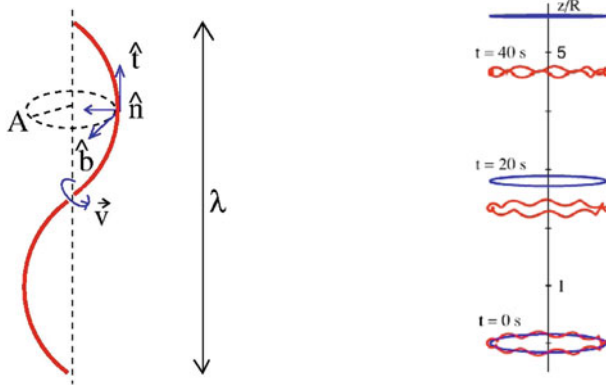
Fig. 5.14 *Left* Schematic of Kelvin waves of amplitude A and wavelength λ. The three unit vectors in the tangent, normal and binormal directions are shown. The waves rotate along the binormal direction, in the direction opposite to the direction of the flow. *Right* Comparison between motion of a vortex ring (radius $R = 0.1$ cm, *blue*) and a vortex ring perturbed by Kelvin waves (relative amplitude $A/R = 0.05$, *red*). Calculation performed with the vortex filament model [12]. Figure adapted with permission from Ref. [12]. Copyrighted by the American Physical Society

where $k = 2\pi/\lambda$ is the wavenumber; in other words, the shorter the wave the faster it rotates. The time sequence shown in Fig. 5.9 shows a vortex ring which hits a straight vortex. It is apparent that after the collision the straight vortex is perturbed by Kelvin waves. Vortex rings can also be perturbed by Kelvin waves, see Fig. 5.14 (right); the vortex ring with waves travels slower than the unperturbed circular ring. Vortex lines also support excitations in the form of breathers [19].

5.10   Vortex Reconnections

When two quantum vortex lines approach each other, they reconnect, changing the topology of the flow. The effect, illustrated in Fig. 5.15, has been experimentally observed in superfluid helium [20] and in atomic condensates [21]. In classical invis-cid fluids (governed by the Euler equation) vortex reconnections are not possible. Reconnections of quantum vortices thus arise from the presence of the quantum pressure term in the Gross–Pitaevskii equation. In classical viscous fluids (governed by the Navier-Stokes equation) reconnections are possible but involve dissipation of energy, whereas in condensates reconnections take place while conserving the energy. Figure 5.16 shows the reconnection of two vortices computed using the GPE. A vortex-antivortex pair, initially slightly bent, propagates to the right. The curvature of the vortices quickly increases at their midpoint, they move faster and hit each other, reconnecting and then moving away.
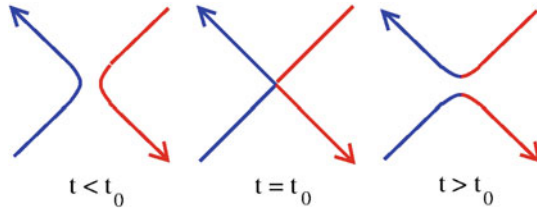
Fig. 5.15 Schematic vortex reconnection of two vortex lines. The *arrows* indicate the direction of the vorticity (the rotation of the fluid around the axis of the vortex). *Left* before the reconnection ($t < t_0$); *Middle* at the moment of reconnection, $t = t_0$; *Right* after the reconnection ($t < t_0$)
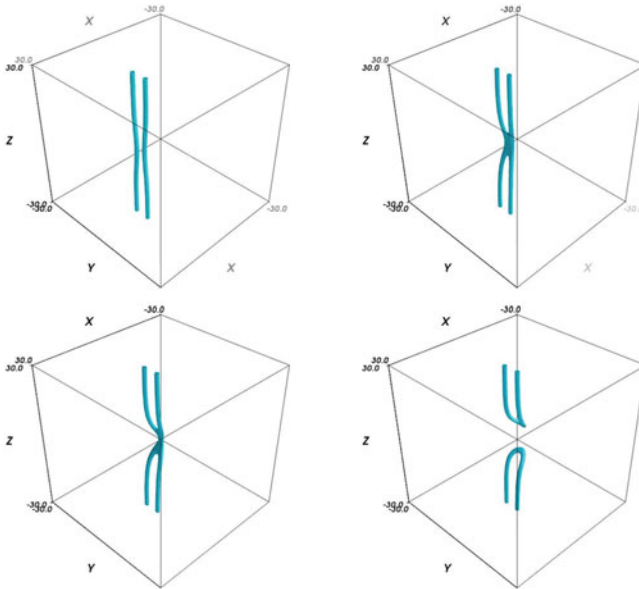
Fig. 5.16 Reconnection of antiparallel vortex lines computed by solving the GPE in a periodic box. Shown is the isosurface of the condensate density $\rho = 0.2$, where $\rho = 1.0$ is the bulk value. Reprinted from [24] with the permission of AIP Publishing

In 2D, vortex reconnections become *annihilation* events in which two vortex points of opposite polarity destroy each other. This can occur through the interaction with a third vortex, and leaves behind a soliton-like rarefaction pulse of sound [25]. Recently, it has been argued that a fourth vortex is required to turn the rarefaction pulse into sound waves which then spread to infinity [26, 27], making the annihilation a four-vortex process.
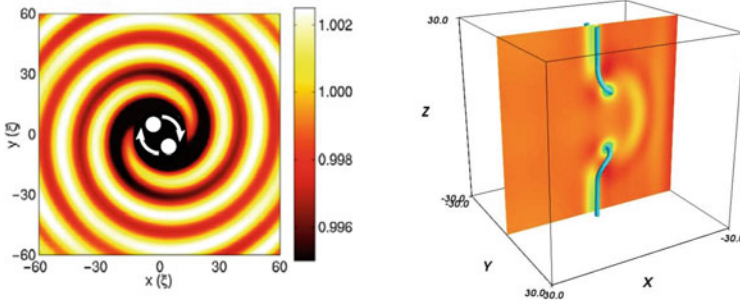
Fig. 5.17 *Left* Pattern of sound waves (density variations) on the xy plane generated by a rotating pair of vortices (shown by the *white dots*). Image adapted from [28]. Note the small amplitude of the sound waves, relative to the background density of one. *Right* Rarefaction sound pulse generated by the vortex reconnection of Fig. 5.16, shown as density variations on the central plane. Reprinted from [24] with the permission of AIP Publishing

5.11   Sound Emission

Even in the absence of thermal effects, vortices can lose energy, and they do so by creating sound waves. This occurs when vortices and vortex elements accelerate, for example, Fig. 5.17 (left) shows the pattern of spiral sound waves emitted outwards by a co-rotating pair of vortices. It also arises during vortex reconnections, which release a sharp pulse of sound, as seen in Fig. 5.17 (right). In 2D annihilation events leave behind only sound waves.

In all of these scenarios, the pattern of the condensate phase changes. The information about this change can travel outwards from the vortices no faster than the speed of sound. Beyond this "information horizon", the condensate phase has the old pattern. The sound waves act to smooth between the new and old patterns, and prevent discontinuities in the phase at this horizon.

The time evolution of a condensate described by the GPE (that is, a condensate at very small temperatures) conserves the total energy, although the relative proportion of kinetic energy (due to vortices) and sound energy (due to waves) may change. In general, a collection of freely-evolving vortices will decay into sound waves, with the energy being transferred into the "sound field", although this decay is typically very slow. The decay can be prohibited, or even reversed, by suitable driving of the system, and under certain conditions, intense sound waves can create vortices [29].
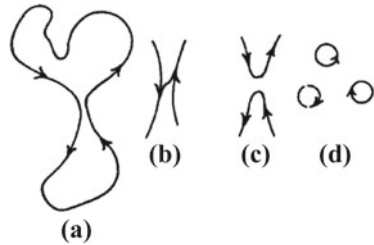
5.12   Quantum Turbulence

Besides lattices, Kelvin waves and vortex rings, other complex vortex states have been studied recently, e.g., U- and S-shaped vortices [30] and vortex knots [31], see Fig. 5.18. But the most challenging vortex state is turbulence.
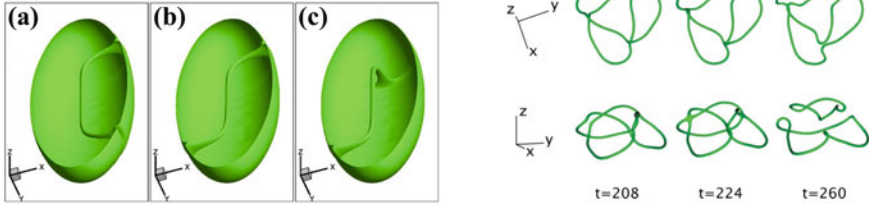
Fig. 5.18 *Left* U and S-shaped vortices in a spheroidal condensate. Reprinted figure with permission from [30]. Copyright 2003 by the American Physical Society. *Right* The break-up of a $T_{2,3}$ vortex knot into two vortex rings. Reprinted figure with permission from [31]. Copyright 2012 by the American Physical Society

Fig. 5.19 Schematic of vortex reconnections and generation of small vortex loops, as envisaged by Richard Feynman [32]

A disordered vortex configuration of many vortices is called a *vortex tangle*; it represents a state of *quantum turbulence*. Vortex reconnections and the resulting generation of smaller and smaller vortex loops in a cascade process were first conjectured by Richard Feynman in his pioneering 1955 article on the applications of quantum mechanics to liquid helium [32]. Figure 5.19 illustrates this cascade. Vortices move in an irregular way around each other, undergoing reconnections which trigger Kelvin waves and generate small vortex loops. In a statistical steady state, the intensity of the turbulence is usually measured (experimentally and numerically) by the *vortex line density L*, defined as the length of vortex lines per unit volume. From the vortex line density L one estimates that the typical distance between vortices is $\ell \approx L^{-1/2}$. As well as vortices, quantum turbulence also features sound waves.

Current work [33, 34] studies properties of quantum turbulence such as velocity and acceleration statistics [35], the emergence of coherent structures out of disorder, and the energy spectrum E_k (representing the distribution of the kinetic energy over the length scales); in particular, the energy spectrum is defined from,

$$E' = \frac{1}{\mathcal{V}} \int_{\mathcal{V}} \frac{\mathbf{v}^2}{2} \mathrm{d}^3 \mathbf{r} = \int_0^\infty E_k \, \mathrm{d}k, \qquad (5.40)$$

where E' is energy per unit mass, $\mathcal{V}$ is the volume and k the wavenumber.

The two main tools to study quantum turbulence are the GPE and the *vortex filament model*, which we describe in Sect. 5.13; the latter is directly relevant to superfluid helium, but is important in general, as it isolates vortex interactions, neglecting finite

core-size effects and sound waves. In the next subsections we describe recent results for 3D and 2D turbulence.

5.12.1   Three-Dimensional Quantum Turbulence

Quantum turbulence at very low temperatures is generated in superfluid helium by stirring with grids, wires or propellers, or by injecting vortex rings. Observations of the decay of the vortex line density and the energy spectrum reveal two turbulent regimes [36]. In the first regime [37], called *quasi-classical turbulence* and illustrated in Fig. 5.20, the energy spectrum obeys the same Kolmogorov scaling of ordinary turbulence ($E_k \sim k^{-5/3}$) over the hydrodynamic range $k_D \ll k \ll k_\ell$ (where $k_\ell = 2\pi/\ell$, $k_D = 2\pi/D$ and D is the system size). This result is confirmed by numerical simulations based on the GPE [38] and the vortex filament model [39–41]. Kolmogorov scaling suggests the existence of a classical *cascade*, which, step-by-step, transfers energy from large eddies to smaller eddies. The concentration of energy at the largest length scales (near k_D) arises from the emergence of transient bundles of vortices of the same polarity [42] which induce large scale flows. Without forcing, quasi-classical turbulence decays as $L \sim t^{-3/2}$.

However, under other conditions, E_k peaks at the intermediate scales followed at large wavenumbers by the k^{-1} dependence typical of isolated vortices, suggesting a random vortex configuration without cascade [41]. In the absence of forcing, this regime, called *ultra-quantum turbulence* [36], decays as $L \sim t^{-1}$.
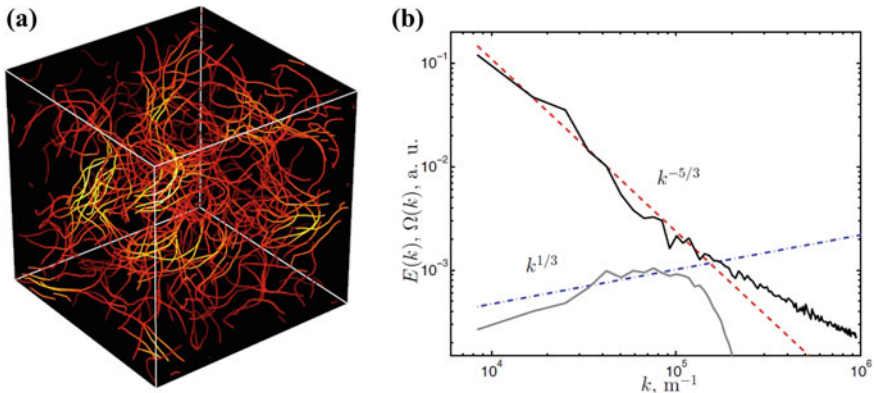
Fig. 5.20   a Quantum turbulence in superfluid helium computed in a periodic box using the vortex filament method [42]. Lighter colour denotes bundles of vortex lines with the same orientation: they are responsible for the emergence of the classical $k^{-5/3}$ Kolmogorov spectrum. Figure adapted with permission from Ref. [42]. Copyrighted by the American Physical Society. **b** Energy spectrum of the kinetic energy E_k vs k, computed using the vortex filament method [40]: note the $k^{-5/3}$ Kolmogorov scaling for $k < k_\ell \approx 1.8 \times 10^5 \, \text{m}^{-1}$. The *curve* at the *bottom* shows that the spectrum of the coarse-grained vorticity is consistent with the $k^{1/3}$ scaling of Kolmogorov theory
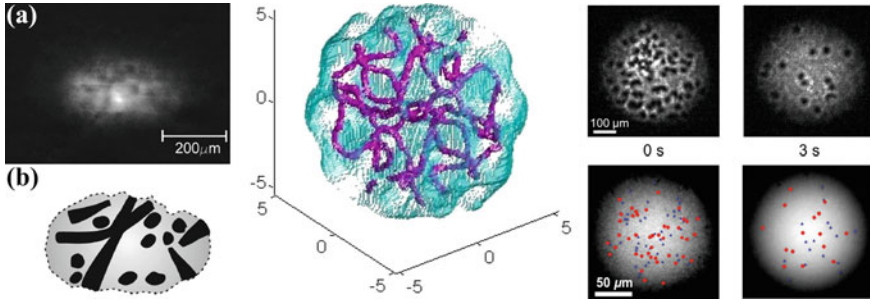
Fig. 5.21 *Left* Absorption images of turbulent 3D atomic condensate (top) and schematic diagram of the inferred distribution of vortices (bottom) [43]. Reprinted figure with permission from [43]. Copyright 2009 by the American Physical Society. *Middle* Quantum turbulence in a harmonically confined atomic condensate computed using the GPE. The surface of the condensate is *pale blue*, the surface of the vortex cores is *purple*. Figure adapted with permission from Ref. [35]. Copyrighted by the American Physical Society. *Right* Experimental absorption (*top*) images of an condensate in a state of 2D turbulence [45]. Images courtesy of Y.I. Shin. Corresponding images of (unexpanded) condensate density from GPE simulations (bottom) [25]. Images courtesy of G.W. Stagg. Vortices with positive (negative) circulation are highlighted by *red circles* (*blue triangles*). The vortices appear much smaller since the condensate has not been expanded

Turbulence in atomic condensates has been generated by stirring the gas with a laser beam or by shaking the confining trap [34, 43]. Current 3D condensates created in the laboratory are relatively small, see Fig. 5.21. The limited separation of length scales (unlike helium, D is not much bigger than ℓ, which is not much bigger than a_0) and the difficulty in directly measuring the velocity have so far prevented measurements of the energy spectrum, although the Kolmogorov regime has been predicted [44].

5.12.2 Two-Dimensional Quantum Turbulence

Due to the ability to engineer the effective dimensionality, atomic condensates also allow the study of 2D turbulence, which consists of a disordered arrangement of vortex points and waves. This is a remarkable feature of quantum fluids, because (with the possible exception of soap films) ordinary flows are never really 2D (for example, only by considering large-scale patterns the atmosphere can be approximated by a 2D flow). Figure 5.21 (right) shows experimental and simulated images of 2D turbulence in a trapped condensate. The turbulence is not being driven and so the number of vortices decays over time.

In fluid dynamics, 2D turbulence is expected to shown unique features such as an *inverse cascade* where increasingly large vortical structures form over time (an example is Jupiter's great Red Spot). The inverse cascade involves the clustering of vortices with the same sign, predicted by Onsager, and represents a phase transition

associated with a state of negative effective temperature (defined in terms of the entropy of the vortex configuration). In the opposite limit the vortices tend to form dipoles [46, 47].

5.13   Vortices of Infinitesimal Thickness

In this section we derive mathematical tools to model quantized vortex lines as *vortex filaments* (in 3D) or *vortex points* (in 2D). Both methods are based on the classical Euler equation. They assume that the fluid is incompressible, thus neglecting sound waves, and treat the vortex cores as line (in 3D) or point (in 2D) singularities. This approximation is realistic for helium turbulence experiments, where there is a wide separation of length scales between the system size ($D \approx 10^{-2}$ to 10^{-1} m), the inter-vortex distance ($\ell \approx 10^{-6}$ to 10^{-4} m) and the vortex core radius ($a_0 \approx 10^{-10}$ m). The approximation is less good for atomic condensates, but the model is useful to isolate pure vortex dynamics from sound and healing length effects.

We have seen that, at length scales larger than the healing length ξ, the Gross–Pitaevskii equation reduces to classical continuity equation and the compressible Euler equation. In the further limit of velocities much less than the speed of sound (i.e. small Mach numbers), density variations can be neglected; in this limit, the compressible Euler equation reduces to the incompressible Euler equation,

$$\frac{\partial \mathbf{v}}{\partial t} + (\mathbf{v} \cdot \nabla)\mathbf{v} = -\frac{1}{\rho}\nabla p, \tag{5.41}$$

where ρ is constant, and the continiuty equation becomes the solenoidal condition $\nabla \cdot \mathbf{v} = 0$.

5.13.1   Three-Dimensional Vortex Filaments

We introduce the vector potential $\mathbf{A}$ defined such that, $\mathbf{v} = \nabla \times \mathbf{A}$. Since the divergence of a curl is always zero, we have $\nabla \cdot \mathbf{A} = 0$, and $\mathbf{A} \rightarrow$ constant for $\mathbf{x} \rightarrow \infty$. The vorticity $\boldsymbol{\omega}$ can be written as,

$$\boldsymbol{\omega} = \nabla \times \mathbf{v} = \nabla \times (\nabla \times \mathbf{A}) = \nabla(\nabla \cdot \mathbf{A}) - \nabla^2 \mathbf{A} = -\nabla^2 \mathbf{A}, \tag{5.42}$$

Given the vorticity distribution $\boldsymbol{\omega}(\mathbf{r}, t)$ at the time t, the vector potential $\mathbf{A}(\mathbf{r}, t)$ is obtained by solving Poisson's equation,

$$\nabla^2 \mathbf{A} = -\boldsymbol{\omega}. \tag{5.43}$$

The solution of Eq. (5.43) at the point $\mathbf{s}$ is,

$$\mathbf{A}(\mathbf{s}, t) = \frac{1}{4\pi} \int_{\mathcal{V}} \frac{\boldsymbol{\omega}(\mathbf{r}, t)}{|\mathbf{s} - \mathbf{r}|} \mathrm{d}^3\mathbf{r}, \tag{5.44}$$

where $\mathbf{r}$ is the variable of integration and $\mathcal{V}$ is volume. Taking the curl (with respect to $\mathbf{s}$), we obtain the *Biot–Savart law*,

$$\mathbf{v}(\mathbf{s}, t) = \frac{1}{4\pi} \int_{V} \frac{\boldsymbol{\omega}(\mathbf{r}, t) \times (\mathbf{s} - \mathbf{r})}{|\mathbf{s} - \mathbf{r}|^3} \mathrm{d}^3\mathbf{r}. \tag{5.45}$$

In electromagnetism, the Biot–Savart law determines the magnetic field as a function of the distribution of currents. In vortex dynamics, the Biot–Savart law determines the velocity as a function of the distribution of vorticity. If we assume that the vorticity $\boldsymbol{\omega}$ is concentrated on filaments of infinitesimal thickness with circulation κ, we can formally replace $\boldsymbol{\omega}(\mathbf{r}, t)\mathrm{d}^3\mathbf{r}$ with $\kappa \mathrm{d}\mathbf{r}$. The volume integral, Eq. (5.45), becomes a line integral over the vortex line configuration $\mathcal{L}$, and the Biot–Savart law reduces to,

$$\mathbf{v}(\mathbf{s}, t) = -\frac{\kappa}{4\pi} \oint_{\mathcal{L}} \frac{(\mathbf{s} - \mathbf{r})}{|\mathbf{s} - \mathbf{r}|^3} \times \mathrm{d}\mathbf{r}. \tag{5.46}$$

Equation (5.46) is the cornerstone of the vortex filament method, in which we model quantized vortices as three dimensional oriented space curves $\mathbf{s}(\xi_0, t)$ of circulation κ, where the parameter ξ_0 is arc length. Since, according to Helmholtz's Theorem, a vortex line moves with the flow, the time evolution of the vortex configuration is given by,

$$\frac{\mathrm{d}\mathbf{s}}{\mathrm{d}t} = \mathbf{v}^{\mathrm{self}}(\mathbf{s}), \tag{5.47}$$

where,

$$\mathbf{v}^{\mathrm{self}}(\mathbf{s}) = -\frac{\kappa}{4\pi} \oint_{\mathcal{L}} \frac{(\mathbf{s} - \mathbf{r})}{|\mathbf{s} - \mathbf{r}|^3} \times \mathrm{d}\mathbf{r}. \tag{5.48}$$

(the *self-induced velocity*) is the velocity which *all* vortex lines present in the flow induce at the point $\mathbf{s}$.

To implement the vortex filament method, vortex lines are discretized into a large number of points $\mathbf{s}_j$ ($j = 1, 2, \ldots$), each point evolving in time according to Eq. (5.48). Vortex reconnections are performed algorithmically. Since the integrand of Eq. (5.48) diverges as $\mathbf{r} \to \mathbf{s}$, it must be desingularized; a physically sensible cutoff length scale is the vortex core radius a_0. This cutoff idea is also behind the following *Local Induction Approximation* (LIA) to the Biot–Savart law,

$$\mathbf{v}^{\mathrm{self}}(\mathbf{s}) = \beta \mathbf{s}' \times \mathbf{s}'', \qquad \beta = \frac{\kappa}{4\pi} \ln\left(\frac{R}{a_0}\right), \tag{5.49}$$

where $\mathbf{s}' = \mathrm{d}\mathbf{s}/\mathrm{d}\xi_0$ is the unit *tangent* vector at the point $\mathbf{s}$, $\mathbf{s}'' = \mathrm{d}^2\mathbf{s}/\mathrm{d}\xi_0^2$ is in the *normal* direction, and $R = 1/|\mathbf{s}''|$ is the local radius of curvature. The physical interpretation of the LIA is simple: at the point $\mathbf{s}$, a vortex moves in the *binormal* direction with speed which is inversely proportional to the local radius of curvature. Note that a straight vortex line does not move, as its radius of curvature is infinite.

To illustrate the LIA, we compute the velocity of a vortex ring of radius R located on the $z = 0$ plane at $t = 0$. The ring is described by the space curve $\mathbf{s} = (R\cos(\theta), R\sin(\theta), 0)$, where θ is the angle and $\xi_0 = R\theta$ is the arc length. Taking derivatives with respect to ξ_0 we have $\mathbf{s}' = (-\sin(\xi_0/R), \cos(\xi_0/R), 0)$ and $\mathbf{s}'' = (-1/R)(\cos(\xi_0/R), \sin(\xi_0/R), 0)$. Using Eq. (5.49), we conclude that the vortex ring moves in the z direction with velocity,

$$\mathbf{v}^{\text{self}} = \frac{\kappa}{4\pi R}\ln(R/a_0)\widehat{\boldsymbol{e}}_z. \tag{5.50}$$

The result is in good agreement with a more precise solution of the Euler equation based on a hollow core at constant volume, which is,

$$\mathbf{v}^{\text{self}} = \frac{\kappa}{4\pi R}\left(\ln\left(\frac{8R}{a_0}\right) - \frac{1}{2}\right)\widehat{\boldsymbol{e}}_z. \tag{5.51}$$

Using the GPE, Roberts and Grant [48] found that a vortex ring of radius much larger than the healing length moves with velocity,

$$\mathbf{v}^{\text{self}} = \frac{\kappa}{4\pi R}\left(\ln\left(\frac{8R}{a_0}\right) - 0.615\right)\widehat{\boldsymbol{e}}_z. \tag{5.52}$$

5.13.2 Two-Dimensional Vortex Points

As in the previous section, we consider inviscid, incompressible ($\nabla \cdot \mathbf{v} = 0$), irrotational ($\nabla \times \mathbf{v} = \mathbf{0}$) flow, and allow singularities. We also assume that the flow is two-dimensional on the xy plane, with velocity field,

$$\mathbf{v}(x, y) = (v_x(x, y), v_y(x, y)), \tag{5.53}$$

The introduction of the *stream function* ψ (not to be confused with the wavefunction), defined by,

$$v_x = \frac{\partial\psi}{\partial y}, \qquad v_y = -\frac{\partial\psi}{\partial x}, \tag{5.54}$$

guarantees that $\nabla \cdot \mathbf{v} = 0$. The irrotationality of the flow implies the existence of a velocity potential ϕ such that $\mathbf{v} = \nabla\phi$,

$$v_x = \frac{\partial \phi}{\partial x}, \qquad v_y = \frac{\partial \phi}{\partial y}. \tag{5.55}$$

It follows that both stream function and velocity potential satisfy the two-dimensional Laplace's equation ($\nabla^2 \psi = 0$, $\nabla^2 \phi = 0$), and well-known techniques of complex variables can be applied. For this purpose, let $z = x + iy$ be a point of the complex plane (rather than the vertical coordinates). We introduce the *complex potential*,

$$\Omega(z) = \phi + i\psi. \tag{5.56}$$

It can be shown that the velocity components v_x and v_y are obtained from,

$$v_x - iv_y = \frac{d\Omega}{dz}, \tag{5.57}$$

Any complex potential $\Omega(z)$ can be interpreted as a two-dimensional inviscid, incompressible, irrotational flow. Since Laplace's equation is linear, the sum of solutions is another solution, and we can add the complex potential of simple flows to obtain the complex potential of more complicated flows. In particular,

$$\Omega(z) = U_0 e^{-i\eta} z, \tag{5.58}$$

represents a uniform flow of speed U_0 at angle η with the x axis, and,

$$\Omega(z) = -\frac{i\kappa}{2\pi} \log(z - z_0), \tag{5.59}$$

represents a positive (anticlockwise) vortex point of circulation κ at position $z = z_0$.

Problems

5.1 Consider the bucket of Sects. 5.5 and 5.6 to now feature a harmonic potential $V(r) = \frac{1}{2} m \omega_r^2 r^2$ perpendicular to the axis of the cylinder. Take the condensate to adopt the Thomas–Fermi profile.

(a) Show that the energy of the vortex-free condensate is $E_0 = \pi m n_0 \omega_r^2 H_0 R_r^4 / 6$, where R_r is the radial Thomas–Fermi radius and n_0 is the density along the axis.
(b) Now estimate the kinetic energy E_{kin} due to a vortex along the axis via Eq. (5.12). Use the fact that $a_0 \ll R_r$ to simplify your final result.
(c) Estimate the angular momentum of the vortex state, and hence estimate the critical rotation frequency at which the presence of a vortex becomes energetically favourable.

5.2 Use the LIA (Eq. (5.49)) to determine the angular frequency of rotation of a Kelvin wave of wave length $\lambda = 2\pi/k$ (where k is the wavenumber) on a vortex with circulation κ.

5.3 Using the vortex point method and the complex potential, determine the translational speed of a vortex-antivortex pair (each of circulation κ) separated by the distance $2D$.

5.4 Using the vortex point method and the complex potential, determine the period of rotation of a vortex-vortex pair (each of circulation κ) separated by the distance $2D$.

5.5 Consider a homogeneous, isotropic, random vortex tangle (ultra-quantum turbulence) of vortex line density L, contained in a cubic box of size D. Show that the kinetic energy is approximately

$$E \approx \frac{\rho \kappa^2 L D^3}{4\pi} \ln\left(\frac{\ell}{a_0}\right), \tag{5.60}$$

where ρ is the density, κ the quantum of circulation, $\ell \approx L^{-1/2}$ is the inter-vortex distance and a_0 is the vortex core radius.

5.6 In an ordinary fluid of kinematic viscosity ν, the decay of the kinetic energy per unit mass, E', obeys the equation

$$\frac{dE'}{dt} = -\nu\omega^2, \tag{5.61}$$

where ω is the rms vorticity. Consider ultra-quantum turbulence of vortex line density L. Define the rms superfluid vorticity as $\omega = \kappa L$, and show that the vortex line density obeys the equation,

$$\frac{dL}{dt} = -\frac{\nu}{c}L^2, \tag{5.62}$$

where the constant c is,

$$c = \frac{1}{4\pi} \ln\left(\frac{\ell}{a_0}\right), \tag{5.63}$$

hence show that, for large times, the turbulence decays as

$$L \sim \frac{c}{\nu}t^{-1}. \tag{5.64}$$

References

1. Y. Shin et al., Phys. Rev. Lett. **93**, 160406 (2004)
2. T. Winiecki, *Numerical Studies of Superfluids and Superconductors*, Ph.D. thesis, University of Durham (2001)
3. E.J. Yarmchuck, M.J.V. Gordon, R.E. Packard, Phys. Rev. Lett. **43**, 214 (1979)
4. J.R. Abo-Shaeer, C. Raman, J.M. Vogels, W. Ketterle, Science **292**, 476 (2001)
5. C. Raman, J.R. Abo-Shaeer, J.M. Vogels, K. Xu, W. Ketterle, Phys. Rev. Lett. **87**, 210402 (2001)
6. A. Recati, F. Zambelli, S. Stringari, Phys. Rev. Lett. **86**, 377 (2001)
7. S. Sinha, Y. Castin, Phys. Rev. Lett. **87**, 190402 (2001)
8. K.W. Madison, F. Chevy, V. Bretin, J. Dalibard, Phys. Rev. Lett. **86**, 4443 (2001)
9. N.G. Parker, R.M.W. van Bijnen, A.M. Martin, Phys. Rev. A **73**, 061603(R) (2006)
10. T.P. Simula, P.B. Blakie, Phys. Rev. Lett. **96**, 020404 (2006)
11. G.W. Stagg, A.J. Allen, C.F. Barenghi, N.G. Parker, J. Phys.: Conf. Ser. **594**, 012044 (2015)
12. C.F. Barenghi, R. Hänninen, M. Tsubota, Phys. Rev. E **74**, 046303 (2006)
13. P. Nozieres, D. Pines, *The Theory of Quantum Liquids* (Perseus Books, Cambridge, 1999)
14. T.W. Neely, E.C. Samson, A.S. Bradley, M.J. Davis, B.P. Anderson, Phys. Rev. Lett. **104**, 160401 (2010)
15. W.J. Kwon, S.W. Seo, S. W., Y. Shin. Phys. Rev. A **92**, 033613 (2015)
16. T. Winiecki, C.S. Adams, Europhys. Lett. **52**, 257 (2000)
17. B. Jackson, J.F. McCann, C.S. Adams, Phys. Rev. A **61**, 013604 (1999)
18. D.V. Freilich, D.M. Bianchi, A.M. Kaufman, T.K. Langin, D.S. Hall, Science **329**, 1182 (2010)
19. H. Salman, Phys. Rev. Lett. **16**, 165301 (2013)
20. G.P. Bewley, M.S. Paoletti, K.R. Sreenivasan, D.P. Lathrop, Proc. Nat. Acad. Sci. USA **105**, 13707 (2008)
21. S. Serafini, M. Barbiero, M. Debortoli, S. Donadello, F. Larcher, F. Dalfovo, G. Lamporesi, G. Ferrari, Phys. Rev. Lett. **115**, 170402 (2015)
22. A.L. Fetter, Rev. Mod. Phys. **81**, 647 (2009)
23. M. Tsubota, K. Kasamatsu, M. Ueda, Phys. Rev. A **65**, 023603 (2002)
24. S. Zuccher, M. Caliari, A.W. Baggaley, C.F. Barenghi, Phys. Fluids **24**, 125108 (2012)
25. G.W. Stagg, A.J. Allen, N.G. Parker, C.F. Barenghi, Phys. Rev. A **91**, 013612 (2015)
26. A.J. Groszek, T.P. Simula, D.M. Paganin, K. Helmerson, Phys. Rev. A **93**, 043614 (2016)
27. A. Cidrim, F.E.A. dos Santos, L. Galantucci, V.S. Bagnato, C.F. Barenghi, Phys. Rev. A **93**, 033651 (2016)
28. N.G. Parker, *Numerical studies of vortices and dark solitons in atomic Bose-Einstein condensates*, Ph.D. thesis, University of Durham (2004)
29. N.G. Berloff, C.F. Barenghi, Phys. Rev. Lett. **93**, 090401 (2004)
30. A. Aftalion, I. Danaila, Phys. Rev. A **68**, 023603 (2003)
31. D. Proment, M. Onorato, C.F. Barenghi, Phys. Rev. E **85**, 036306 (2012)
32. R.P. Feynman, Applications of quantum mechanics to liquid helium, in *Progress in Low Temperature Physics*, vol. 1, ed. by C.J. Gorter (North-Holland, Amsterdam, 1955)
33. C.F. Barenghi, L. Skrbek, K.R. Sreenivasan, Proc. Nat. Acad. Sci. USA suppl.1 **111**, 4647 (2014)
34. M.C. Tsatsos, P.E.S. Tavares, A. Cidrim, A.R. Fritsch, M.A. Caracanhas, F.E.A. dos Santos, C.F. Barenghi, V.S. Bagnato, Phys. Reports **622**, 1 (2016)
35. A.C. White, C.F. Barenghi, N.P. Proukakis, A.J. Youd, D.H. Wacks, Phys. Rev. Lett. **104**, 075301 (2010)
36. P.M. Walmsley, A.I. Golov, Phys. Rev. Lett. **100**, 245301 (2008)
37. J. Maurer, P. Tabeling, Europhys. Lett. **43**, 29 (1998)
38. C. Nore, M. Abid, M.E. Brachet, Phys. Rev. Lett. **78**, 3896 (1997)
39. T. Araki, M. Tsubota, S.K. Nemirovskii, Phys. Rev. Lett. **89**, 145301 (2002)
40. A.W. Baggaley, C.F. Barenghi, Y.A. Sergeev, Europhys. Lett. **98**, 26002 (2012)

41. A.W. Baggaley, C.F. Barenghi, Y.A. Sergeev, Phys. Rev. B **85**, 060501(R) (2012)
42. A.W. Baggaley, J. Laurie, C.F. Barenghi, Phys. Rev. Lett. **109**, 205304 (2012)
43. E.A.L. Henn, J.A. Seman, G. Roati, K.M.F. Magalhaes, V.S. Bagnato, Phys. Rev. Lett. **103**, 045301 (2009)
44. M. Kobayashi, M. Tsubota, Phys. Rev. A **76**, 045603 (2007)
45. W.J. Kwon, G. Moon, J. Choi, S.W. Seo, Y. Shin, Phys. Rev. A **90**, 063627 (2014)
46. T. Simula, M.J. Davis, K. Helmerson, Phys. Rev. Lett. **113**, 165302 (2014)
47. T.P. Billam, M.T. Reeves, B.P. Anderson, A.S. Bradley, Phys. Rev. Lett. **112**, 145301 (2014)
48. P.H. Roberts, J. Grant, J. Phys. A: Math. Gen. **4**, 55 (1971)

Appendix A
Simulating the 1D GPE

The GPE is a nonlinear partial differential equation, and its solution must, in general, be obtained numerically. A variety of numerical methods exist to solve the GPE, including those based on Runge–Kutta methods, the Crank–Nicolson method and the split-step Fourier method.[1] The latter (also known as the time-splitting spectral method) is particularly compact and efficient, and here we apply it to the 1D GPE. Furthermore, we introduce the imaginary time method for obtaining ground state solutions. Basic Matlab code is provided.

A.1 Split-Step Fourier Method

The split-step fourier method is well-established for numerically solving the time-dependent Schrodinger equation, written here in one-dimension,

$$i\hbar\frac{\partial\psi(x,t)}{\partial t} = \hat{H}\psi(x,t). \tag{A.1}$$

The Hamiltonian $\hat{H}$ can be expressed as $\hat{H} = \hat{T} + \hat{V}$, where $\hat{T} \equiv -\frac{\hbar^2}{2m}\frac{\partial^2}{\partial x^2}$ and $\hat{V} \equiv V(x)$ are the kinetic and potential energy operators. Integrating from t to $t + \Delta t$ (and noting the time-independence of the Hamiltonian) leads to the time-evolution equation,

$$\psi(x, t + \Delta t) = e^{-i\Delta t\hat{H}/\hbar}\psi(x, t). \tag{A.2}$$

The operators T and V do not commute, hence $e^{-i\Delta t\hat{H}/\hbar} \neq e^{-i\Delta t\hat{T}/\hbar}e^{-i\Delta t\hat{V}/\hbar}$. Nonetheless, the following approximation,

$$e^{-i\Delta t\hat{H}/\hbar}\psi \approx e^{-i\Delta t\hat{V}/2\hbar}e^{-i\Delta t\hat{T}/\hbar}e^{-i\Delta t\hat{V}/2\hbar}\psi, \tag{A.3}$$

---

[1]A. Minguzzi, S. Succi, F. Toschi, M.P. Tosi, P. Vignolo, Phys. Rep. **395**, 223 (2004).

holds with error $\mathcal{O}(\Delta t^3)$. In position space $\hat{V}$ is diagonal, and so the operation $e^{-i\Delta t \hat{V}/2\hbar}\psi$ simply corresponds to multiplication of $\psi(x, t)$ by $e^{-i\Delta t V(x)/2\hbar}$. Although $\hat{T}$ is not diagonal in position space, it becomes diagonal in reciprocal space. Conversion to reciprocal space is achieved by taking the Fourier transform $\mathcal{F}$ of the wavefunction $\tilde{\psi}(k, t) = \mathcal{F}[\psi(x, t)]$, where k denotes the 1D wavevector. Then the kinetic energy operation corresponds to multiplication of $\tilde{\psi}(k, t)$ by $e^{-i\hbar\Delta t k^2/2m}$. Thus Eq. (A.3) can be written as,

$$\psi(x, t + \Delta t) \approx e^{-\frac{i}{2\hbar}V(x)\Delta t} \cdot \mathcal{F}^{-1}\left[e^{-\frac{i\hbar k^2}{2m}\Delta t} \cdot \mathcal{F}\left[e^{-\frac{i}{2\hbar}V(x)\Delta t} \cdot \psi(x, t)\right]\right]. \quad (A.4)$$

In practice, the computational expense of performing forward and backward Fourier transforms to evaluate Eq. (A.3) is small (particularly when using numerical fast Fourier transform techniques) compared to the significant expense of evaluating the kinetic energy term directly in position space. Note that the split-step method naturally incorporates periodic boundary conditions.

The above method was developed for the linear Schrodinger equation with time-independent Hamiltonian. Remarkably, it holds for the GPE (despite its nonlinearity and time-dependent Hamiltonian) under the replacement $V(x) \mapsto V(x) + g|\psi|^2$. Errors of $\mathcal{O}(\Delta t^3)$ are maintained, providing the most up-to-date ψ is always employed during the sequential operations in Eq. (A.4).[2]

A.2   1D GPE Solver

We now outline the approach to solve the 1D GPE using the split-step method, with reference to the Matlab code included below. To make the numbers more convenient, the GPE is divided through by $\hbar$ (equivalent to considering energy in units of $\hbar$). We consider a 1D box, discretized into grid points with spacing Δx (dx), and extending over the spatial range $x = [-M\Delta x, M\Delta x]$, where M (M) is a positive integer. Position is described by a vector x_i (x), defined as $x_i = -M\Delta x + (i-1)\Delta x$, with $i = 1, \ldots, 2M + 1$. The potential $V(x)$ is defined as the vector $V_i = V(x_i)$. Starting from the initial time, the wavefunction $\psi(x)$, represented by the vector $\psi_i = \psi(x_i)$ (psi), is evolved over the time interval Δt (dt) by evaluating Eq. (A.4) numerically by replacing the Fourier transform $\mathcal{F}$ (and its inverse $\mathcal{F}^{-1}$) by the discrete fast Fourier transform. Here, wavenumber is discretized into a vector k_i (k), defined as $k_i = -M\Delta k + (i-1)\Delta k$, with $\Delta k = \pi/M\Delta x$ (dk). This time iteration step is repeated N_t (Nt) times to find the solution at the desired final time.

The Matlab code below simulates a BEC of 5000 ^{87}Rb atoms with $a_s = 5.8$ nm and trapping frequencies $\omega_\perp = 2\pi \times 100$ Hz and $\omega_x = 2\pi \times 40$ Hz. Starting from the narrow non-interacting ground state (Gaussian) profile, the condensate undergoes oscillating expansions and contractions, due to the competition between repulsive

[2]J. Javanainen, J. Ruostekoski, J. Phys. A **39**, L179 (2006).

interactions and confining potential. Note—under different scenarios, reduced time and grid spacings may be required to ensure numerical convergence.

```
% SOLVES THE 1D GPE VIA THE SPLIT-STEP FOURIER METHOD
clear all;clf; %Clear workspace and figure

hbar=1.054e-34;amu=1.660538921e-27; %Physical constants
m=87*amu;as=5.8e-9; %Atomic mass; scattering length
N=1000;wr=100*2*pi;wx=40*2*pi; %Atom number; trap frequencies

M=200; Nx=2*M+1;
dx=double(2e-7); x=(-M:1:M)*dx; %Define spatial grid
dk=pi/(M*dx); k=(-M:1:M)*dk; %Define k-space grid
dt=double(10e-8); Nt=200000; %Define time step and number

lr=sqrt(hbar/(m*wr)); lx=sqrt(hbar/(m*wx)); %HO lengths
g1d=2*hbar*hbar*as/(m*lr^2); %1D interaction coefficient

V=0.5*m*wx^2*x.^2/hbar; %Define potential
psi_0=sqrt(N/lx)*(1/pi)^(1/4)*exp(-x.^2/(2*lx^2)); %Initial wavefunction

%[psi_0,mu] = get_ground_state(psi_0,dt,g1d,x,k,m,V); %Imaginary time

Nframe=100; %Data saved every Nframe steps
t=0; i=1; psi=psi_0; spacetime=[]; %Initialization

for itime=1:Nt %Time-stepping with split-step Fourier method
    psi=psi.*exp(-0.5*1i*dt*(V+(g1d/hbar)*abs(psi).^2));
    psi_k=fftshift(fft(psi)/Nx);
    psi_k=psi_k.*exp(-0.5*dt*1i*(hbar/m)*k.^2);
    psi=ifft(ifftshift(psi_k))*Nx;
    psi=psi.*exp(-0.5*1i*dt*(V+(g1d/hbar)*abs(psi).^2));
    if mod(itime,Nt/Nframe) == 0  %Save wavefunction every Nframe steps
      spacetime=vertcat(spacetime,abs(psi.^2)); t
    end
    t=t+dt;
end

subplot(1,3,1); %Plot potential
plot(x,V,'k'); xlabel('x (m)'); ylabel('V (J/hbar)');

subplot(1,3,2); %Plot initial and final density
plot(x,abs(psi_0).^2,'k',x,abs(psi).^2,'b');
legend('\psi(x,0)','\psi(x,T)');xlabel('x (m)');ylabel('|\psi|^2 (m^{-1})');

subplot(1,3,3); % Plot spacetime evolution as pcolor plot
dt_large=dt*double(Nt/Nframe);
pcolor(x,dt_large*(1:1:Nframe),spacetime); shading interp;
xlabel('x (m)'); ylabel('t (s)');
```

A.3   Imaginary Time Method

A convenient numerical method for obtaining ground state solutions of the Schrodinger equation/GPE is through imaginary time propagation. The wavefunction $\psi(x, t)$ can be expressed as a superposition of eigenstates $\phi_m(x)$ with time-dependent amplitudes $a_m(t)$ and energies $E_m(t)$, i.e. $\psi(x, t) = \sum_m a_m(t)\phi_m(x)$, for which, after the substitution $t \rightarrow -i\Delta t$, the evolution Eq. (A.3) becomes,

$$\psi(t + \Delta t) = e^{-\Delta t \hat{H}/\hbar}\psi(x, t) = \sum_m a_m(t)\phi_m(x)e^{-\Delta t E_m/\hbar}. \tag{A.5}$$

The amplitude of each eigenstate contribution decays over time, with the ground state (with lowest E_m) decaying the slowest. Thus, by renormalizing ψ after each iteration (to ensure the conservation of the desired norm/number of particles), ψ will evolve towards the ground state.

Convergence may be assessed by monitoring the chemical potential. This is conveniently evaluated using the relation $\mu = (\hbar/\Delta t) \ln |\psi(x, t)/\psi(x, t + \Delta t)|$ at some coordinate within the condensate; this relation is obtained by introducing the eigenvalue μ and imaginary time into Eq. (A.3).

The Matlab function `get_ground_state` below obtains the GPE ground state via imaginary time propagation. Uncommenting line 19 in the above GPE solver calls this function prior to real time propagation; as one expects, the profile remains static in time.

```
% SOLVES THE 1D GPE IN IMAGINARY TIME USING THE SPLIT-STEP METHOD
function [psi,mu] = get_ground_state(psi,dt,g1d,x,k,m,V)

hbar=1.054e-34; dx=x(2)-x(1); dk=2*pi/(x(end)-x(1));
N=dx*norm(psi).^2; Nx=length(x); psi_mid_old=psi((Nx-1)/2);
mu_old=1; j=1; mu_error=1;
 while mu_error > 1e-8
     psi=psi.*exp(-0.5*dt*(V+(g1d/hbar)*abs(psi).^2));
     psi_k=fftshift(fft(psi))/Nx;
     psi_k=psi_k.*exp(-0.5*dt*(hbar/m)*k.^2);
     psi=ifft(ifftshift(psi_k))*Nx;
     psi=psi.*exp(-0.5*dt*(V+(g1d/hbar)*abs(psi).^2));

     psi_mid=psi((Nx-1)/2);
     mu=log(psi_mid_old/psi_mid)/dt; mu_error=abs(mu-mu_old)/mu;

     psi=psi*sqrt(N)/sqrt((dx*norm(psi).^2));
    if mod(j,5000) == 0
         mu_error
     end
     if j > 1e8
         'no solution found'
         break
     end
     psi_mid_old=psi((Nx-1)/2); mu_old=mu; j=j+1;
 end
end
```

Problems

A.1 Obtain the ground-state density profiles for a 1D condensate under harmonic confinement with (i) no interactions, (ii) repulsive interactions and (iii) attractive interactions. Compare (ii) with the corresponding Thomas–Fermi profile.

A.2 Starting from the Gaussian harmonic oscillator ground state, release the non-interacting condensate into an infinite square well (achieve by setting the potential to a high value towards the edge of the box, and zero elsewhere). Repeat for repulsive and attractive interactions. How does the initial expansion (before reflection from the box walls) depend on the interactions?

Now simulate the longer-term behaviour. The wavefunction undergoes revivals, known as the Talbot effect, and forms a "quantum carpet".[3]

A.3 Form the ground state solution for a repulsively-interacting condensate in a harmonic trap. Excite a centre-of-mass ("sloshing") oscillation by shifting the trap by some distance at $t = 0$. Similarly, excite a monopole mode by slightly weakening the trap at $t = 0$. Extract the frequencies of these modes. Do the frequencies depend on the number of particles and the interaction sign/strength?

---

[3]I. Marzoli et al. Acta Phys. Slov. **48**, 323 (1998) [arXiv:quant-ph/9806033].

Index